

NASA Contractor Report 3567

NASA
CR
3567-
v.1
c.1

LOAN COPY RE
AFWL TECHNICAL
KIRTLAND AFB

0062159

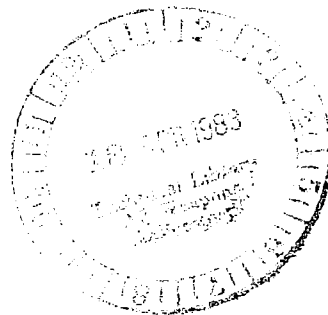


TECH LIBRARY KAFB, NM

Analysis of Unswept and Swept Wing Chordwise Pressure Data From an Oscillating NACA 0012 Airfoil Experiment

Volume I - Technical Report

A. O. St. Hilaire
and F. O. Carta



CONTRACT NAS1-16041
MARCH 1983



25th Anniversary
1958-1983

NASA



NASA Contractor Report 3567

Analysis of Unswept and Swept Wing Chordwise Pressure Data From an Oscillating NACA 0012 Airfoil Experiment

Volume I - Technical Report

A. O. St. Hilaire
and F. O. Carta
*United Technologies Research Center
East Hartford, Connecticut*

Prepared for
Langley Research Center
under Contract NAS1-16041



National Aeronautics
and Space Administration

Scientific and Technical
Information Branch

1983

TABLE OF CONTENTS

	<u>Page</u>
SUMMARY	1
INTRODUCTION	2
LIST OF SYMBOLS	4
DESCRIPTION OF THE DATA BASE	6
DATA PROCESSING AND ANALYSIS	8
Introductory Comments	8
Data Compaction and Storage	8
Data Analysis Techniques	9
Normalization Procedure	12
PRESSURE WAVE STUDY	13
Wave Speed Analysis	13
Vortex Inception Angle Variation	17
DISCUSSION OF NORMALIZATION PROCEDURE	20
UNSTEADY CHORDWISE PRESSURE ANALYSIS	22
Overview	22
Effect of α_M on Normalization	23
Leading Edge Region Time Histories	24
Parameter Analysis of Chordwise Pressures	26
Effect of Sweep on Peak Angle of Attack Response	27
DISCUSSION OF INTEGRATED LOAD RESULTS	29
SUMMARY OF RESULTS	31
APPENDIX: DISCUSSION OF MEASUREMENT ERROR	33
REFERENCES.	34
TABLES	
FIGURES	

SUMMARY

A further examination of previously reported unsteady aerodynamic data on a tunnel spanning wing (both swept and unswept), obtained in the United Technologies Research Center (UTRC) Main Wind Tunnel, was performed. In the original study (NASA CR-3092) the analysis of these data was focused on the behavior of the integrated force components of the NACA 0012 airfoil section tested (lift, drag, and pitching moment). The objective of the present investigation was to study the unsteady chordwise force response on the airfoil surface and to examine its sensitivity to the various system parameters.

The main body of this data analysis was carried out by analyzing the propagation speed of pressure disturbances along the chord, and by studying the behavior of the unsteady part of the chordwise pressure distribution at various points of the airfoil pitching cycle. It was found that Mach number effects dominate the approach to stall and the inception of stall, both static and dynamic; the stall angle decreases as the Mach number increases. It was also found that sweep dominates the load behavior within the stall regime; large phase differences between unswept and swept responses, that do not exist at low lift coefficient, appear once the stall boundary has been penetrated.

Conventional pressure normalization procedures were reviewed and it was found that the cosine law for sweep angle is not applicable at angles of attack above the stall angle, both for steady and unsteady conditions. It was also found that the reduced frequency parameter traditionally used in unsteady aerodynamic analysis is not a reliable indicator of the unsteady aerodynamic response in the high angle of attack regime.

An additional analysis was performed to resolve a troublesome aspect of the previously reported results. It was found that the relative displacement of the lift and moment hysteresis loop response (excluding nonoscillatory terms) during upstroke between unswept and swept wings is a real effect, and is almost entirely described by the phase and amplitude differences in the first harmonic components.

INTRODUCTION

The need for swept wing unsteady aerodynamic data into the dynamic stall regime was addressed in Ref. 1 wherein test results were reported from experiments performed using a NACA 0012 airfoil section tunnel-spanning wing (TSW) oscillating in pitch in both the unswept and 30 deg swept back configurations. The main motivation for obtaining such data is for use by the helicopter designer who must account for a widely varying aerodynamic environment on the rotor blade as it traverses the azimuth plane. In addition to this immediate engineering application, these results provide the opportunity to examine the effects of sweep at moderate pitching amplitudes, and thus permit the evaluation of techniques currently in use for estimating the unsteady swept wing aerodynamic forces from the existing data banks for zero sweep angle.

The results that were reported in Ref. 1 focused on (1) the unsteady integrated load components (lift, drag, and moment) computed from unsteady chordwise pressure distributions for both stalled and unstalled conditions, and (2) the surface pressure fluctuations obtained in the stall regime from companion steady airfoil experiments. Several findings were reported, of which the most notable is that sweep tends to delay the onset of dynamic stall. A summary of the main results can be found on page 40 therein. A companion data report to Ref. 1 was also published (Ref. 2) containing a complete set of unsteady normal force, chord force, lift force, drag force, and moment responses in the form of hysteresis loops. The data report was arranged to emphasize the effect of sweep on the results. A review of related work in this field can be found in the introduction to Ref. 1 and in the associated bibliography.

The present report utilizes the same data base that was used to produce the results in Refs. 1 and 2 and is essentially a continuation of that data analysis. Here, the emphasis is on the unsteady chordwise pressure data and their sensitivity to the various test parameters: wing sweep angle, Λ ; pitching amplitude, $\bar{\alpha}$; mean angle of attack, α_M ; pitching frequency, f ; and Mach number, $M_c = M_\infty \cos \Lambda$. Two parametric studies are presented herein: (1) the behavior of the chordwise propagation of pressure waves associated with the dynamic stall process, and (2) the behavior of the unsteady surface pressures, both individually as time histories over the whole motion cycle, and collectively as chordwise distributions at specific points of the motion cycle.

An accompanying data report (Ref. 3) contains listings of the first ten harmonic components of the individual chordwise pressure responses, and of the integrated load results. The data tables in Ref. 3 can be used to reproduce the oscillatory components of the individual pressure time histories,

and the complete normal force, chord force, lift force, drag force, and moment coefficient time histories. (Here, the term "complete" means nonoscillatory plus oscillatory parts, and it is understood that the chord and drag forces were computed by integration of pressure distributions and therefore do not include the effects of viscous drag.) Hysteresis plots of the integrated force coefficient results (versus angle of attack) were reported in Ref. 2.

The present document begins with a review of the data base and the approach to the normalization of the data. This is followed by a description of the data retrieval process that was used to expedite the performance of the parametric analysis. A discussion of the chordwise wave propagation phenomenon and its sensitivity to the test parameters is then presented. A review of the effectiveness of the data normalization procedure is presented next. The report then proceeds with the analysis of the chordwise response behavior to the various test parameters, including a brief examination of the individual pressure time histories very near the leading edge. Finally, a troublesome aspect of the hysteresis loop comparisons of Ref. 1 is revisited and resolved.

LIST OF SYMBOLS

A	dimensionless pitch rate, Eq. (14)
A_v	dimensionless pitch rate at vortex inception angle
a_∞	sound speed
c	airfoil chord
C_C	chord force coefficient
C_D	drag force coefficient, Eq. (5)
C_L	lift force coefficient, Eq. (4)
C_M	moment coefficient
C_N	normal force coefficient
$C_p(\chi, t)$	pressure coefficient distribution, Eq. (3)
f	airfoil pitching frequency, Hz
k_c	chordwise reduced frequency, Eq. (2)
M_c	chordwise Mach number, Eq. (1)
M_∞	free stream Mach number
m	slope, Eq. (11)
$p(\chi, t)$	chordwise pressure distribution, newton/m ²
q	dynamic pressure based on chordwise velocity, newton/m ²
T	period, sec
t	time, sec
t_0	vortex inception time, sec
V_c	chordwise velocity, m/sec
V_∞	free stream velocity, m/sec

LIST OF SYMBOLS (Cont'd)

\bar{v}_w	average dimensionless wave speed, Eq. (8)
$\bar{v}_{w_{ij}}$	average dimensionless wave speed between stations i and j
α	airfoil angle of attack, deg, Eq. (6)
α_M	mean angle of attack, deg
α_s	dynamic stall inception angle, deg, Eq. (19)
α_{ss}	steady state stall angle, deg, Eq. (19)
α_v	vortex inception angle, Eq. (10)
α_{vo}	constant used in Eq. (11)
ϵ	data scatter parameter, Eq. (15)
Λ	sweep angle, deg
τ	dimensionless time based on oscillation period, also fraction of period
τ_o	dimensionless vortex inception time based on oscillation period
ϕ	phase lead, deg
χ	distance from airfoil nose
ω	circular frequency, rad/sec

DESCRIPTION OF THE DATA BASE

The data base for the present study was obtained from aerodynamic experiments performed on an oscillating tunnel-spanning wing (TSW) in both unswept and 30 deg swept configurations in the United Technologies Research Center (UTRC) Main Wind Tunnel. The chordwise profile taken normal to the wing leading edge is a NACA 0012 airfoil. A detailed description of the test program can be found in Ref. 1. Although the data base and normalization procedure are also fully described therein, the portions that are pertinent to the present study are repeated here for completeness. Of primary interest in this investigation is the unsteady chordwise pressure distribution. The unsteady data acquisition points that were used along the chord are schematically depicted in Fig. 1.

The experiments of Ref. 1 were performed for the matrix of test parameter settings shown in Table 1. These parameters were the wing sweep angle, Λ , the amplitude of pitching motion, $\bar{\alpha}$, the mean angle of attack, α_M , the pitching frequency, f , and the approach Mach number, M_∞ . The effect of sweep was accounted for in the normalization process by referring all of the data to the component of Mach number, M_c , normal to the wing span. This quantity is related to the freestream value, M_∞ , by the formula

$$M_c = M_\infty \cos \Lambda \quad (1)$$

where subscript c denotes the chordwise direction. Data were obtained for two values of M_c ($= 0.30$ and 0.40) for each value of Λ ($= 0$ deg and 30 deg). This approach required testing the 30 deg swept configuration at a higher freestream velocity as shown in Table 1. Unsteady pressure data were obtained for two values of $\bar{\alpha}$ (8 deg and 10 deg) at four mean angle of attack settings ($0, 9, 12$ and 15 deg) about the quarterchord axis. The angles were measured in a plane perpendicular to the span axis. The choice of pitching frequencies used during the test program was predetermined according to Table 2 which lists the nominal values of reduced frequency defined by

$$k_c = \frac{\pi c f}{a_\infty M_c} \quad (2)$$

where a_∞ is the speed of sound.

The effects of sweep on the pressure data were accounted for in Ref. 1 by normalizing the data with respect to the velocity component normal to the span to obtain the following expression for dimensionless pressure

$$C_p(\chi, t) = -p(\chi, t)/q\cos^2\Lambda \quad (3)$$

where χ is the dimensionless position along the chord and t is time. This nondimensionalization scheme is based on a steady-state sweep analysis which assumes the flow to be potential and the pressure distribution on the wing to be determined entirely by the magnitude of the normal velocity component, $V_\infty \cos \Lambda$. Note also that in this report, the pressure coefficient is defined as the negative of the normalized pressure. This is convenient for relating positive integrated lift to a positive value of C_p .

DATA PROCESSING AND ANALYSIS

Introductory Comments

The analysis of unsteady chordwise pressures and their sensitivity to the various system parameters by conventional methods is a formidable undertaking for a data base the size of the one shown in Table 1. This is true mainly because an important aspect in the study of chordwise pressure behavior involves a comparative study of the pressure distribution at various points of the airfoil pitching motion cycle. This approach requires substantial data manipulation if a reasonable number of representative cases and comparisons are to be analyzed in any significant detail. (It is noted that the chordwise pressure in the present study consists of 21 channels of data, including 13 upper surface and 8 lower surface locations.)

The approach that was used to expedite the present analysis consisted of (1) compacting the processed data into a data file where each record (test case) is addressable either by record number or by the corresponding test parameters (Λ , $\bar{\alpha}$, α_M , f , and M_c) that are unique to the record, and (2) tailoring a data management program where specific channels from any combination of records can be retrieved for numerical and/or graphical analysis by means of a series of built-in computer queries.

Data Compaction and Storage

The direct access data file that was used in the present analysis was generated in two steps: (1) compacting the unswept and swept data bases into a common data file, and (2) creating a file directory for interfacing the data file with the data retrieval software (described later in this section).

Data compaction was achieved for the unswept and swept data bases by cycle-averaging the individual pressure responses of each case over 5 cycles of the airfoil pitching motion and then reducing the resulting time histories to 24 harmonic components (including the zeroth harmonic term). The fundamental frequency used in the Fourier analysis process was the pitching frequency of the airfoil. The unswept and swept wing data bases were then combined into a common compacted data file.

The normal force, chord force, and moment responses were then directly computed from separate chordwise integrations (by trapezoidal rule) of the in-phase and out-of-phase portions (relative to the airfoil motion) of each

harmonic component. The lift and drag forces were then computed from the normal force and chord force using the following formulas:

$$C_L = C_N \cos \alpha + C_C \sin \alpha \quad (4)$$

$$C_D = C_N \sin \alpha - C_C \cos \alpha \quad (5)$$

where α is given by

$$\alpha = \alpha_M + \bar{\alpha} \sin \omega t. \quad (6)$$

A schematic depicting the force vectors is shown in Fig. 2. By inspection of these equations, it is seen that the harmonic coefficients of C_L and C_D cannot be computed directly from the harmonic coefficients of C_N and C_C because of the nonlinear appearance of α within the trigonometric terms. Therefore, an intermediate computation of the C_L and C_D responses was made by substituting time history reproductions of C_N , C_C , and α into Eqs. (4) through (6). The resulting C_L and C_D time histories were then Fourier analyzed, and together with C_N , C_C , and C_M , were added to the compacted data file by extending the number of channels of each test case from 22 (α and 21 chordwise pressures) to 27.

The final step in completing the contents of the compacted file was adding to each case the steady state force and moment coefficients corresponding to C_N , C_C , C_M , C_L , and C_D as well as the actual test parameter values (Λ , $\bar{\alpha}$, α_M , f , and M_C) measured during the test.

The interface of the data file with data retrieval software was achieved by installing a file directory header into the data file. The file directory was indexed to match the actual record sequence of the file and was set up with nominal values of Λ , $\bar{\alpha}$, α_M , f , and M_C corresponding to the actual test parameter values of each record. The objective here is that all requests to the data file are processed by means of the file directory. Data retrieval is thus achieved without having to directly search through the individual records of the file. This is an especially desirable approach when records are being retrieved out of sequence from the file.

Data Analysis Techniques

The objective of the data analysis in this report is to examine and evaluate the effect of the test parameters (Λ , $\bar{\alpha}$, α_M , f , and M_C) on the unsteady pressure response over the surface of the blade. To accomplish

this, the authors found it necessary to use several graphical representations while concentrating on the various characteristic features of the data. It is appropriate, therefore, that the descriptions of each figure type be consolidated in the present section so that subsequent sections can be devoted primarily to the discussion of the physical phenomena being depicted.

Much of this report deals with changes in unsteady blade pressure associated with changes in certain of the test parameters. Recall that in this report, pressure coefficient is defined as the negative of the normalized pressure at any station,

$$C_p(\chi, \tau) = -p(\chi, \tau)/q \cos^2 \Lambda. \quad (7)$$

In some figures the pressure coefficient is plotted versus dimensionless chord position, χ , while in others the independent variable is dimensionless time, τ . For example, Fig. 3 represents the pressure coefficient plotted versus χ at the instant that $\alpha = \alpha_M$ (upper panel), and at the peak incidence angle, $\alpha = \alpha_M + \bar{\alpha}$ (lower panel). The direct comparison to be made here between the solid and dashed lines is between two chordwise Mach numbers. (Other plots will show the effect of other parameters in the same manner.) A similar chordwise pressure plot, shown in Fig. 4, depicts the first harmonic pressure amplitude (upper panel) and phase angle (lower panel) taken from the Fourier representation of the pressure time history. Here the direct comparison is between the two sets of symbols representing the two sweep angles tested.

A third type of chordwise pressure plot is shown in Fig. 5. Here, the format of the individual panels is similar to that of Fig. 3, but the intent of the figure as a whole is significantly different. Now the solid and dashed lines denote upper and lower surface pressures, and the major comparison is made between the two columns. (In this case, the effect of sweep is depicted.) A second parametric comparison can be made in Fig. 5 by viewing successive pairs of panels which, in this case, are for three instantaneous angles of attack, α . Both the numerical value of α and the relative position of the blade during the motion cycle are shown between each pair.

The last type of chordwise pressure plot shown in Fig. 6 differs from Fig. 5 only in the orientation of the individual plots. Here, for example, the upper row curves were obtained at a mean angle of attack of $\alpha_M = 9$ deg, and the lower row at $\alpha_M = 12$ deg. Each column then represents a specific angular displacement from the mean (i.e., 7, 7.5, and 8 deg) as the peak angle of attack is approached and attained during the upstroke.

Individual pressure time histories are also used in this report. A typical example is shown in Fig. 7. In every case the upper row of panels

will represent the motion of the blade about the mean angle of attack, and each successive row will show the pressure time history for the specific chordwise measurement stations denoted by χ . As in Fig. 5, the comparisons in Fig. 7 are made between solid and dashed lines within each panel, and between adjacent columns.

In Ref. 4 it was shown that plots of unsteady pressure versus both time and chordwise position could be analyzed to yield quantitative information on the chordwise propagation of pressure waves. That technique is applied herein. Plots of pressure time histories were produced at several chordwise positions, and in the example of Fig. 8, the data are restricted to the first 15 percent of the chord for clarity. In this figure the vertical axis represents both the unsteady pressure coefficient level relative to steady state (left scale) and the chordwise location of the pressure measurement (right scale). The result is a pseudo three-dimensional plot of the $C_p(\chi, \tau)$ surface, referred to as a pressure carpet plot. To interpret these figures, refer each curve to its zero level at the appropriate χ -tic mark on the right scale, and use the left scale as a gage to measure the pressure relative to its zero level. The precipitous drop in C_p in the vicinity of $\tau=0.17$ to 0.2 is customarily associated with dynamic stall and is usually ascribed to the formation and chordwise passage of a stall cell or vortex.

For this carpet plot a set of constant pressure contours (isobars) was constructed in the χ, τ plane as shown in Fig. 9. The two columns of numbers on the right represent the percent of the pressure range from minimum to maximum and the associated value of unsteady pressure coefficient relative to steady state (for example, a value of $C_p = -3.0$ is 4 percent of the range above minimum C_p , and a value of $C_p = 6.0$ is 74 percent of the range above minimum). The numbers that are appended to each contour are the corresponding values of C_p . As shown in Ref. 4, the direction of the family of contour extremes identifies the direction of wave propagation, and a simple estimate of the slope yields the wave speed.

The sensitivity of the contours to relatively small timewise discrepancies in data from adjacent measuring stations revealed a minor error in the data set, which is described in the Appendix. The error manifested itself in small time or phase displacements of adjacent signals, and is occasionally noticeable as a zigzagging ripple in the chordwise pressure distribution, as, for example, in the lower right panel of Fig. 5, or in several panels of Fig. 6.

As noted in the Appendix the entire data set was uniformly corrected for the computations made in the wave speed analysis, but the corrections were confined to that section only. The remainder of the analysis, including all of the tabulated data in Ref. 3, remained uncorrected, to preserve its commonality with previous results from Refs. 1 and 2.

Normalization Procedure

In the present analysis normalization was achieved by dividing the negative of the measured unsteady pressures by the dynamic pressure, $0.5 \rho V_c^2$, and by multiplying the circular frequency of airfoil pitching oscillation by $c/2V_c$. Here, V_c is the chordwise component of the freestream velocity ($V_\infty \cos \Lambda$) and c is the airfoil chord.

PRESSURE WAVE STUDY

Wave Speed Analysis

The use of pressure coefficient carpet and contour plots for wave speed analysis was introduced in the previous section, using Figs. 8 and 9 for the forward 15 percent portion of the airfoil as examples. The corresponding carpet and contour plots for the entire chord are presented in Figs. 10 and 11. (In this particular case, $\Lambda = 0$ deg, $\bar{\alpha} = 8$ deg, $\alpha_M = 9$ deg, $f = 10$ Hz, $M_c = 0.3$ and $k_c = 0.125$.) In both contour plots only positive values of C_p (cf. Eq. 7) have been included, to focus on the region of maximum normal force and hence on the stall wave propagation.

Figure 12 is a contour map of the pressure surface in Fig. 8, focused on the first four tenths of the period, $0 \leq \tau \leq 0.4$. In this figure, the connection between the contour extremum at the leading edge ($\chi_0 = 0.004$) with the extremum at the 15 percent chord location ($\chi_2 = 0.149$) by the dashed line labeled "overall 15%" is used for estimating the wave speed over the forward 15 percent of the blade chord. It is seen that this set of contour extremes moves toward increasing time as the chord is traversed from front to rear. The dimensionless wave speed was shown in Ref. 4 to be related to the ratio of chord extent to elapsed time by the formula

$$\bar{V}_W = \frac{c \Delta \chi}{V_c \Delta \tau} \quad (8)$$

and with $t = \tau T = 2\pi\tau/\omega$, and $k_c = c\omega/2V_c$, this becomes

$$\bar{V}_W = \frac{k_c}{\pi} \cdot \frac{\Delta \chi}{\Delta \tau} \quad (9)$$

A careful study of the contours in Fig. 12 indicates that the locus of contour extremes is not linear but can be represented by straight line segments of different slopes. A two-segment estimate for this case is illustrated in Fig. 13. The end points of the first segment are denoted by (χ_0, τ_0) and (χ_1, τ_1) and those of the second segment by (χ_1, τ_1) and (χ_2, τ_2) . Hence, there are actually two distinct regions within the first 15 percent of the chord that have different wave speeds. For this particular example, these values are

$$(\chi_0, \chi_1, \chi_2) = (0.004, 0.028, 0.149)$$

$$(\tau_0, \tau_1, \tau_2) = (0.123, 0.155, 0.187)$$

and with $k = 0.125$, application of the wave speed Eq. (9) yields

$$\bar{v}_{W_{01}} = \frac{k}{\pi} \frac{\chi_1 - \chi_0}{\tau_1 - \tau_0} = 0.035 \text{ (first segment)}$$

$$\bar{v}_{W_{12}} = \frac{k}{\pi} \frac{\chi_2 - \chi_1}{\tau_2 - \tau_1} = 0.146 \text{ (second segment)}$$

$$\bar{v}_{W_{02}} = \frac{k}{\pi} \frac{\chi_2 - \chi_0}{\tau_2 - \tau_0} = 0.090 \text{ (overall, 15\%)}$$

where the wave speed subscripts match the subscripts of the initial and end-point coordinates of the segment in question. Furthermore, Fig. 14 for the entire chord shows that another discontinuity can be defined at the 15 percent chord station, separating the forward region from the aft region of the chord, implying additional speed changes along the chord. This last coordinate point is given by

$$(\chi_3, \tau_3) = (0.971, 0.284)$$

and two additional wave speeds can be defined,

$$\bar{v}_{W_{23}} = \frac{k}{\pi} \frac{\chi_3 - \chi_2}{\tau_3 - \tau_2} = 0.326 \text{ (third segment)}$$

$$\bar{v}_{W_{03}} = \frac{k}{\pi} \frac{\chi_3 - \chi_0}{\tau_3 - \tau_0} = 0.239 \text{ (overall, 100\%)}$$

For convenience, the individual segment wave speeds for this example are collected below.

$$\bar{v}_{W_{01}} = 0.035$$

$$\bar{v}_{W_{02}} = 0.090$$

$$\bar{v}_{W_{12}} = 0.146$$

$$\bar{v}_{W_{03}} = 0.239$$

$$\bar{v}_{W_{23}} = 0.326$$

It is seen that the wave is slowest in the region of high pressure gradient near the leading edge ($\bar{v}_{W_{01}}$). This is the region characterized by the dense array of constant level contour lines in Fig. 13. Conversely, the wave

travels more rapidly over the second segment (\bar{V}_{w12}) where the chordwise pressure gradient is lower, and attains its highest speed over the last segment (\bar{V}_{w23}) where pressure gradient is minimal. However, without additional evidence, it is impossible to establish a cause-and-effect relationship between the pressure gradient and the speed variation. Alternatively, starting inertia in the vortex rollup associated with dynamic stall could be the reason for wave acceleration. Whatever the cause, a consistent observation has been made (as will be shown presently), that the wave speed seems to be inversely related to the unstalled chordwise pressure gradient.

Before proceeding with a detailed examination of parametric trends, several values of wave speed for the unswept wing tests are compared in Fig. 15 with those obtained in Ref. 4. Overall averaged wave speed for the entire chord (\bar{V}_{w03}), and local averaged wave speed for 15 percent of the chord (\bar{V}_{w02}), are plotted versus reduced frequency in the upper and lower panels of Fig. 15, respectively. The original data are denoted by the open symbols, and the current data for $\bar{\alpha} = 8$ deg and $M_c = 0.3$ by the solid symbols. It is seen that the current results are consistent with previous calculations.

A study was performed to examine the effect of each of the test parameters on wave speed and the results are shown in Figs. 16 through 18. In each figure the overall wave speed, \bar{V}_{w03} , is plotted versus reduced frequency, k_c . Mean angle of attack variation is always depicted by the three symbols used: circle, triangle, and square. In each figure there are four panels, with one parameter held constant from left panel to right panel, a second parameter held constant from top panel to bottom panel, and the variation of the parameter of primary interest for each figure highlighted by the contrast between open and solid symbols. In Fig. 16 the effect of amplitude variation is examined by noting that the open symbols represent $\bar{\alpha} = 8$ deg and the solid symbols represent $\bar{\alpha} = 10$ deg. This figure shows little or no effect of amplitude on overall wave speed. Although it was originally suggested in Fig. 20 of Ref. 4 that increasing amplitude appeared to increase the value of \bar{V}_{w03} at any k_c , the present results do not corroborate this earlier indication. It is noteworthy that the data in Ref. 4 were obtained for a variety of Mach number values and of profile shapes, whereas the present results are taken from a wholly self-consistent data base. Also, this figure and subsequent figures show that there is little or no effect of mean angle of attack on wave speed, which agrees with the observations made in Ref. 4.

Mach number is the parameter of primary interest in Fig. 17, and its effect, although small, seems to be consistent. For $\Lambda = 0$ deg (top panels)

the higher Mach number (solid symbols) yields a slightly smaller value of \bar{V}_{W03} than $M_c = 0.3$, although the two sets of data appear to converge as k increases. For $\Lambda = 30$ deg (bottom panels) there is less distinction between the two sets of Mach number data, and it could be argued that the effect of Mach number is minimal.

By far, the parameter that has the greatest effect on \bar{V}_W is the sweep angle, as shown in Fig. 18. In all four panels the overall wave speed for the unswept wing (open symbols) is consistently and significantly greater than that for the swept wing (solid symbols) by a factor of 1.5 to 2.0. This phenomenon of lower chordwise wave speed in swept flow has not been predicted by any previous analysis nor observed in any previous experiment.

In an effort to examine these trends more closely, wave speeds for the several segments (defined earlier) were computed and are displayed in Figs. 19 and 20 for $M_c = 0.3$ and 0.4, respectively (at the same value $\bar{\alpha} = 8$ deg). The three left hand panels in each figure are the three local wave speeds, \bar{V}_{W01} , \bar{V}_{W12} , and \bar{V}_{W23} , proceeding aft along the chord. The two right hand panels are the two average wave speeds, \bar{V}_{W02} over the first 15 percent of the chord, and \bar{V}_{W03} over the entire chord. (The latter are repeated in these two figures from the top panels of Fig. 18.) It is clearly shown here that there is substantially no effect of sweep angle on the local wave speed over the forward 15 percent of the chord, either by examination of the panels for \bar{V}_{W01} and \bar{V}_{W12} , or from the results for \bar{V}_{W02} . Virtually all of the sweep effect is perceived to occur in the aft portion of the chord (lower left panel of both Figs. 19 and 20), with factors of as much as 2 observed in swept wing wave speed versus that for the unswept wing. This result is representative of all cases examined. If the pressure wave is associated with the formation and chordwise transport of a vortex, these results would imply that the vortex motion along the chord is independent of sweep over the first 15 percent region of the chord, and is strongly dependent on sweep thereafter.

Finally, an analysis of the chordwise variation of local wave speed is provided by Fig. 21 for the case with $M_c = 0.4$, $\bar{\alpha} = 8$ deg and $\alpha_M = 15$ deg. In this figure the local wave speed is plotted versus dimensionless chord position, χ , for several values of k . The unswept results are plotted in the left panels and the swept results in the right. Linear scales are used in the upper panels, and two effects clearly emerge. The first is the general increase of \bar{V}_W with k at any given value of χ (although there is some scatter) for both values of Λ . The second is the continual increase with χ of \bar{V}_W for $\Lambda = 0$ deg, and the much smaller increase with χ of \bar{V}_W aft of $\chi = 0.1$ for $\Lambda = 30$ deg. In an effort to spread out the many points plotted at

small values of χ , the same data are repeated in the semi-log plots in the lower two panels. While there is no unusual revelation afforded by these semi-log plots, they do appear to resolve the cluttered points into an orderly chordwise progression.

Vortex Inception Angle Variation

In pursuing further the interpretation of the phenomenon just described as the formation of a vortex and its subsequent chordwise transport, the inception time can be studied and related to the vortex inception angle, α_v . A direct computation of α_v , can be made by substituting the dimensionless inception time, $\tau_o = \omega t_o / 2\pi$ (cf. Fig. 13 or 14), into Eq. (6) for instantaneous angular position,

$$\alpha_v = \alpha_M + \bar{\alpha} \sin 2\pi\tau_o \quad (10)$$

The results are shown in Figs. 22 and 23 as plots of vortex inception angle versus reduced frequency. As before, the use of circles, triangles, and squares denote $\alpha_M = 9, 12$, and 15 deg, and open and solid symbols highlight the comparison of sweep angle effects in Fig. 22 and of Mach number effects in Fig. 23. These plots also contain information on the steady state stall angle (triangular symbols pointing to the appropriate values on the ordinate) and on the best linear fit to the data. The latter were obtained by a least squares procedure for each data group, and the former by estimating the steady state angle of attack at which $dCM/d\alpha = 0$ in Figs. 14 through 17 in Ref. 1.

In both figures the vortex inception angle, α_v , varies linearly with k_c , as indicated by the good correlation of the linear least squares line

$$\alpha_v = \alpha_{v0} + mk_c \quad (11)$$

with the measured data, and the narrow scatter range for each data set. (In this equation α_{v0} is the zero frequency intercept and m is the slope.) Figure 22 shows that sweep has a tendency to delay vortex inception, but this delay is less than two degrees overall, and less than one degree in the majority of cases examined. In contrast to this result, Fig. 23 shows a substantial Mach number effect, with incipient vortex angle differences of as much as three or four degrees as M_c varies from 0.3 to 0.4. Both figures indicate that the steady state stall angle based on zero moment slope, α_{ss} , is unaffected by sweep angle changes. (However, Figs. 14 through 17 of Ref. 1 show that the shape of the lift curve changes significantly in the direction of lift stall delay with increasing sweep, consistent with Fig. 3 of Ref. 5 which is based on the data of Ref. 6.) A comparison of the steady state stall angle with the zero frequency intercept of the least squares

vortex inception line shows a two degree difference at $M_c = 0.3$, and a reasonably good correlation at $M_c = 0.4$. These zero frequency and steady state values are summarized in Table 3.

A careful study of Figs. 22 and 23 reveals little or no effect of mean angle of attack on the incipient vortex angle. Specifically, at any constant value of k_c there is no discernable trend of α_v with α_m ; there is only scatter. This is an observation that is directly concerned with the effect of pitch rate on α_v , which is addressed next.

A case to be considered in detail is represented by the solid symbols at $k_c \approx 0.125$ in the lower left panel of Fig. 22 for $M_c = 0.3$, $\bar{\alpha} = 10$ deg, and $\Lambda = 30$ deg. In this instance the vortex inception angle is very nearly 16 deg for all three values of α_m . This is demonstrated in Fig. 24 which depicts three motion time histories for $\alpha_m = 9, 12$, and 15 deg versus dimensionless time, τ . A horizontal line at $\alpha_v = 16$ deg represents the observed insensitivity of the vortex inception angle to changes in α_m , and leads directly to a consideration of pitch rate effects. For a sinusoidal motion involving instantaneous angle of attack, α , mean angle of attack, α_m , and amplitude of motion, $\bar{\alpha}$ as given by Eq. (6), the instantaneous dimensional pitch rate is given by

$$\dot{\alpha} = \omega \bar{\alpha} \cos \omega t = \omega \bar{\alpha} \sqrt{1 - \sin^2 \omega t} \quad (12)$$

A combination of Eqs. (6) and (12) yields

$$\dot{\alpha} = \omega \sqrt{\bar{\alpha}^2 - (\alpha - \alpha_m)^2} \quad (13)$$

which can be converted to the dimensionless pitch rate, A , by the formula (cf. Ref. 7)

$$A = \frac{c}{2a\omega M_c} \dot{\alpha} = k_c \sqrt{\bar{\alpha}^2 - (\alpha - \alpha_m)^2} \quad (14)$$

The values of A for the intersections of the $\alpha_v = 16$ deg line with the three motion curves in Fig. 24 are noted on the figure and are seen to vary from 0.0156 to 0.0216. (The minor changes in the actual measured values of α_v at each k_c in Figs. 22 and 23 will result in some scatter but will not materially affect the conclusions reached.)

A direct examination of the effect of mean angle of attack variations on α_v with reduced frequency effects excluded is afforded by a return to Eq. (11). Recalling that this equation is a linear least squares fit, the scatter of individual data points may be quantitatively evaluated by rewriting the equation in the form

$$\varepsilon = \alpha_v - \alpha_{v0} - mk_c \quad (15)$$

where $\epsilon \equiv 0$ for an exact linear fit. Values of k_c , τ_o , α_v (from Eq. (10)), ϵ (from Eq. (15)), and A_v (from Eq. (14)) with $\alpha = \alpha_v$ are listed in Table 4, and ϵ is plotted versus A_v in Fig. 25 for all vortex inception events. This figure emphasizes the irregularity of the scatter, and leads directly to the observation that the vortex inception angle is independent of the pitch rate when k_c is fixed. With the exception of a few isolated points the error, ϵ , is generally bounded by $|\epsilon| < 0.5$ deg, and never exceeds ± 1.0 deg.

A question must be raised at this point on the possible relationship of the vortex inception angle, α_v , to the various dynamic stall angle concepts that have been cited in the literature. As far back as Halfman's 1951 report (Ref. 8) and up to the present time, several authors have shown that the dynamic stall angle increases with both increasing reduced frequency and pitch rate. One of the more complete examinations is that of Gormont (Ref. 9), based on data and analyses from previous work (Refs. 10, 11). Here it is shown that the dynamic moment stall angle, based on $\partial C_M(\text{dynamic})/\partial \alpha = 0$, varies linearly with the square root of the pitch rate, and, for the thick V23010-1.58 airfoil examined, approaches the steady state stall angle as the zero pitch rate limit is reached.

To permit a comparison of Gormont's linear fit of the Ref. 10 dynamic stall angle results with the current data, the steady-state stall angle was removed from the vortex inception angle results of the present experiment ($\alpha_v - \alpha_{ss}$, from Tables 3 and 4), and then plotted versus \sqrt{A} in Fig. 26. The $M_c = 0.4$ linear fit to Gormont's thick airfoil moment stall results (lower left panel of Fig. 11 in Ref. 9) are shown plotted as dashed lines in the two $M_c = 0.4$ panels of Fig. 26. Although there is considerable scatter of the data, a linear trend is discernable for $\bar{\alpha} = 10$ deg (lower two panels). Gormont's linear fit for moment stall angle starts from the origin and lies roughly parallel to, and significantly above, the α_v data in the lower right panel. If these data were linearly extrapolated to zero pitch rate, the intercept value would lie approximately 1.5 deg below the steady state stall angle, which is in direct contradiction to the result shown in Table 3 and in the lower right panel of Fig. 22. This can be resolved by noting that a linear behavior of the data is observed for $\alpha_v - \alpha_{ss}$ plotted versus \sqrt{A} in Fig. 26 or versus A in Fig. 27. In the latter, only the cases for $\bar{\alpha} = 10$ deg are repeated. The data are now more in keeping with the results in Fig. 22, and the original Gormont linear data fit is now a parabola. The apparent inconsistency lies in the lack of data at low pitch rates (or reduced frequency), and the only clear result from the $M_c = 0.4$ evidence is that leading edge vortex inception precedes moment stall, assuming that both the V23010-1.58 airfoil data of Ref. 9 and the current NACA 0012 airfoil data can be validly compared in this manner.

DISCUSSION OF NORMALIZATION PROCEDURE

Generally, the purpose of normalization is to consolidate data to a common reference. This is done to highlight the nonsimilar aspects of the data from case to case and thus to permit a more effective analysis of their dependence on the various test parameters. In well behaved small disturbance problems, for example, the normalization process coalesces the data to a common curve so that they become amenable to a general qualitative analysis. In the present investigation, however, the fluctuations in the measured pressures exceed what is normally considered "small disturbance" levels. In realization of this and the fact that much of the data was obtained within the stalled flow regime, the following discussion attempts to identify the limitations of the normalization procedure used in this report.

An example of how well the normalization procedure works below stall with the current data base is depicted in Fig. 28a in which unsteady data obtained from the 30 deg swept wing at $\bar{\alpha} = 8$ deg, $\alpha_M = 0$ deg, $M_c = 0.40$, and $f = 8$ Hz ($k_c = \pi cf/M_c a_\infty = 0.076$) are compared with data similarly obtained at $M_c = 0.30$, and $f = 6$ Hz (also at $k_c = 0.076$). This example shows that the reduced frequency normalization procedure successfully coalesces the linear part (first harmonic component) of the chordwise response distribution to a common curve at low aerodynamic load ($\alpha_M = 0$ deg). Conversely, Fig. 28b shows some deterioration in similarity when results for the same combinations of Mach number and frequency are compared at $\alpha_M = 9$ deg. This result indicates that reduced frequency similarity deteriorates at high angles of attack.

The data set reported on herein and in Ref. 1 includes effects due to wing sweep angle. Sweep was accounted for in the normalization process by utilizing the component of freestream velocity normal to the span as the normalizing velocity. This simple approach is the same that has been traditionally used in the analysis of steady-state data. An example of the effectiveness of this approach to swept wing normalization in similarity analysis is shown in Fig. 29a for the zero mean angle of attack case at $f = 8$ Hz, $\bar{\alpha} = 8$ deg, and $M_c = 0.40$. Figure 29b shows the same comparison but at $\alpha_M = 9$ deg. As in Fig. 28b, it is seen that the higher mean angle of attack causes a deterioration in the sweep similarity between normalized data.

On the basis of the examples shown in Figs. 28 and 29, it would appear that the present normalization procedure is generally effective in highlighting the nonsimilar aspects of the data, and is thus useful in determining the effect of the various test parameters on the oscillatory stall phenomenon.

It is useful to further examine this normalization scheme by using it to make a preliminary evaluation of the effects of f , M_c , and Λ on the complete unsteady chordwise response of the upper surface at zero mean angle of attack. Figures 30 through 32, respectively, show the effect of f , M_c , and Λ at the lowest, mean, and highest incidence points of the motion cycle. For the range of parameters tested, these figures show that the general shape and magnitude of the unsteady chordwise pressure distribution of the zero mean angle of attack configuration are in good agreement at the moderate pitching amplitude of $\bar{\alpha} = 8$ deg.

The effectiveness of the current normalization procedure in coalescing the pressure coefficient distributions helps emphasize the differences in the leading edge region results. These differences are especially notable in Fig. 31 where the effect of Mach number is shown. Since conclusions about the behavior of oscillatory pressures cannot be made on the basis of chordwise pressure distributions alone, individual pressure time histories must also be examined to obtain information about the amplitude and phase behavior over the entire cycle. An illustration of this is shown in Fig. 33 where each column contains cyclically averaged time history traces of the four leading edge region pressure coefficients from the same cases that were used to produce the chordwise plot comparisons of Figs. 30 through 32. From left to right columns, the results in Fig. 33 show the effects of f (corresponding to Fig. 30), M_c (corresponding to Fig. 31) and Λ (corresponding to Fig. 32).

Figure 33 shows that the effect of increasing f on the pressure coefficient time history is to increase the lag of the response, while the effect of increasing M_c is to increase the magnitude of the response at the high and low pitching angles of the motion cycle. The rightmost column of Fig. 33 shows that the effect of Λ on the pressure coefficient response is minimal with the swept configuration slightly leading the unswept case.

Finally, it is noted that the parameter k_c can be varied either by changing f or M_c . A comparison of the left and middle columns of Fig. 33 shows that the effect of variation in k_c in these figures is dependent on whether f or M_c is varied. Because of this lack of uniqueness in the sensitivity of the response to variations in k_c , the parameter analysis in this report will focus on the effects of f , M_c , and Λ rather than k_c , M_c , and Λ .

UNSTEADY CHORDWISE PRESSURE DISTRIBUTION ANALYSIS

Overview

The chordwise pressure distribution analysis in this section is limited to 8 degree pitching amplitude data with special attention to the leading edge region. Three examples of the behavior of the chordwise distribution are shown in Figs. 34 through 36 for mean angles of attack of 0, 9, and 15 deg, respectively. Each figure shows the pressure distributions on both surfaces at specific points of the motion cycle for both the unswept (left column) and swept (right column) wing configurations. The airfoil pitch position (relative to mean angle of attack) corresponding to these distributions is indicated by the dot on the adjacent waveform between the columns. Other test parameters, common to these examples, are $M_c = 0.30$, $f = 8$ Hz ($k_c \approx 0.102$), and $\bar{\alpha} = 8$ deg.

Before proceeding with the description of the results, it is noted that steady state stall occurs at approximately $\alpha = 13$ deg for $M_c = 0.30$ and at approximately $\alpha = 10.5$ deg for $M_c = 0.40$ (Table 3). Therefore, in terms of the present test configurations, dynamic stall penetration occurs at angles of attack greater than the mean for $\alpha_M = 9$ deg, either slightly above or below the mean for $\alpha_M = 12$ deg (depending on M_c) and below the mean for $\alpha_M = 15$ deg. This aerodynamic behavior relative to α_M should be borne in mind during the discussion of the examples in this section.

The cases shown in Figs. 34 through 36 are singled out as typical of the entire data base for the range of mean angles of attack tested. In addition to being a representative zero degree mean angle of attack case, Fig. 34 can also be used as a benchmark for evaluating the quality and consistency of the data. For example, the upper and lower surface chordwise pressure distributions in Fig. 34 appear nearly symmetric with the motion within each column. This is consistent with the profile shape of the NACA 0012 airfoil. In particular, note how the main features of the upper and lower surface responses are reversed at mean angle of attack ($\alpha \approx 0$ deg) when the upstroke and downstroke distributions are compared. Similarly note the reversal of the surface distributions at the maximum and minimum points of the motion cycle. Another test of consistency is to compare the unswept and swept results. As expected by the discussion of the previous section, the data appear nearly the same throughout the motion cycle. (It is further noted that the unswept and swept wing results were generated in two separate tunnel entries.)

In contrast, the stalled flow penetration case shown in Fig. 35 ($\alpha_M = 9$ deg) shows no evidence of symmetry in the response about the mean angle of attack. This example also shows that sweep similarity is significantly

altered in the higher incidence angle range as the airfoil oscillates in and out of stall. In this comparison, the decrease in similarity is especially noticeable at peak incidence where the unswept wing has experienced a more severe collapse of the suction response than the swept configuration.

Figure 36 ($\alpha_M = 15$ deg) shows chordwise distributions that were generated mostly within the stalled flow region. Here it is seen that the differences between the unswept and swept wing results are not as severe, giving the appearance that some sweep similarity is regained when the airfoil is in deep stall. However, as will be shown in later paragraphs of this section, this is not the case since there remains substantial disagreement, especially in the forwardmost 2 percent region of the chord, during the entire motion cycle. On the basis of Figs. 35 and 36 it appears that the dissimilarities due to sweep are strongest when the airfoil load is in transition between an unstalled and a stalled response.

Effect of α_M on Normalization

The remaining discussion of the chordwise pressure data is focused on the sensitivity of the suction (upper) surface distribution to the various test parameters with occasional emphasis on the effects of sweep. The cases and their behavior highlighted in this section are typical of the entire data set.

In the previous section it was shown that the normalization procedure used in the data reduction successfully coalesces the first harmonic component of the zero mean incidence angle cases to a common curve (cf. Figs. 28 and 29). This coalescence was further demonstrated in Figs. 30 through 32 for the complete unsteady component of the total response at zero mean angle of attack. In these latter three figures comparisons were made showing the respective effects of pitching frequency, Mach number, and sweep.

The impact of mean angle of attack on this generalized behavior is now examined by comparing the swept wing results in Figs. 37 ($\alpha_M = 0$ deg) and 38 ($\alpha_M = 9$ deg). Each figure, in turn, shows comparisons between two test cases in which both the frequency and Mach number are varied simultaneously while maintaining a constant reduced frequency of $k_c = 0.076$. The variations in frequency and Mach number between cases are the same in each figure.

There is nearly perfect agreement between the two cases over the entire cycle at $\alpha_M = 0$ deg (Fig. 37) confirming the validity of reduced frequency scaling at low load. However, when a similar comparison is made at $\alpha_M = 9$ deg (Fig. 38), the two cases are in disagreement. This deterioration in generalized behavior occurs over the entire high angle of attack range of the motion cycle with maximum disagreement at peak α where the unsteady separation effects spread over the entire chord. Conversely, it is noted that

similarity in the chordwise response is regained at the minimum point of the cycle where $\alpha = 1.0$ deg (Fig. 38). The disagreement in the chordwise responses over most of the cycle is due to the difference in Mach number between the two cases as illustrated in the following discussion.

The sensitivity of the data at $\alpha_M = 9$ deg to variations in the reduced frequency is examined in the next two figures for both the unswept (left column) and swept (right column) wings at the mean, maximum, and minimum points of the motion cycle. The objective here is to show the influence of k_c on the data by separately varying the pitching frequency (Fig. 39) and Mach number (Fig. 40). In Fig. 39, the variation in k_c (due to f) is three times that of Fig. 40 (due to M_c) and yet the degree and trend of the change in the chordwise response between cases in each figure is about the same for both the unswept and swept configurations. These figures show that the trend of the pressure response distribution, although different in magnitude, is generally consistent with the variation in k_c (due to changes in either f or M_c) and verify the dominant influence of M_c on k_c .

A further inspection of Figs. 39 and 40 also shows that although the influence of k_c (due to changes in either f or M_c) is generally the same between unswept and swept results, there are regions of the motion cycle where k_c has the opposite effect. (For example, near peak angle of attack in Fig. 40, an increase in k_c corresponds to a decrease in suction for the unswept response and an increase in suction for the swept response in the forward 10 percent region of the chord.)

This difference in the effect of k_c on the response at specific points of the cycle is partly due to the difference in the phasing of the unsteady load response relative to the pitching motion between the unswept and swept configurations. As a result, the effect of k_c shows up differently at various points of the cycle, especially in the transition region (between stalled and unstalled flow) where the airfoil surface pressure response appears to be most sensitive to parameter variations. Examples illustrating the sensitivity of the phasing of the leading edge region pressure response are presented next.

Leading Edge Region Time Histories

An important aspect in the parametric evaluation of chordwise load behavior is the analysis of the pressure time histories at various points along the chord. The objective here is to show representative examples from the data base and to highlight some of the main features in the behavior of the pressure time histories to variations in the test parameters. The time histories shown in Figs. 41 through 43 each contain three-harmonic component reconstructions of the leading edge region responses at the 0.4, 1.0, and 1.9

percent chord positions of the suction surface. (The choice of three-harmonic component plots rather than the total response is to keep the parametric analysis relatively simple while not giving up any essential features.) Each figure is arranged in 3 columns corresponding to the 0, 9, and 15 degree mean incidence angle configurations. Each column is comprised of the blade pitching time history at the top followed by the three forwardmost suction surface time histories at $\chi = 0.004, 0.010, \text{ and } 0.019$.

Figure 41 shows the effect of frequency at $M_c = 0.30$, $\Lambda = 0$ deg, and $\bar{\alpha} = 8$ deg. In this figure, it is seen that a frequency increase from 4 to 8 Hz (or k_c increasing from 0.051 to 0.102) has only a minor impact, showing up mainly as a slight increase in the phase lag (right shift) of the responses at $\alpha_M = 0$ deg and 9 deg. At $\alpha_M = 15$ deg, however, this increase in frequency causes a substantial increase in the phase lag of the response during the upstroke as well as a significant diminution in the response level during the downstroke. Figure 44 is a companion to Fig. 41 where the 9 deg (left column) and 15 deg (right column) mean incidence angle time histories from the leading edge region are repeated with additional time histories further down along the chord at $\chi = 0.045, 0.073, 0.114, \text{ and } 0.268$. This figure shows little variation in the relative phasing throughout the forwardmost quarterchord region. This is most easily seen during the first quarter cycle of the $\alpha_M = 15$ deg configuration.

Figures 42 and 45 show the effect of Mach number at $f = 8$ Hz, $\Lambda = 0$ deg, and $\bar{\alpha} = 8$ deg using the same comparison approach as in Figs. 41 and 44. Here Fig. 42 shows that an increase in Mach number has a greater effect on the leading edge region response than does the variation in the frequency (cf. Fig. 41). This sensitivity of the leading edge region response to the Mach number is especially significant at $\alpha_M = 9$ deg and to a lesser extent at $\alpha_M = 15$ deg. In particular, it is noted that the increase in Mach number lowers the stall penetration angle and reduces the sharpness of the dynamic stall event. Figure 45 shows that this sensitivity of the aerodynamic response to M_c persists at least to $\chi = 0.268$.

Examples of the effect of sweep on the time history behavior of the chordwise response are shown next in Figs. 43 and 46 at $f = 8$ Hz, $M_c = 0.30$, and $\bar{\alpha} = 8$ deg. The zero degree mean angle of attack results in Fig. 43 show that sweep effects are essentially negligible throughout the cycle all way to the forwardmost station at $\chi = 0.004$. Conversely, sweep significantly alters the leading edge region response when $\alpha_M = 9$ and 15 deg. In the 9 deg mean angle of attack case, sweep effects remain fairly significant through the quarterchord region while the 15 deg mean angle of attack case shows a substantial decline in the influence of sweep beyond $\chi = 0.045$. The most notable effect of sweep on these results is in the increased phase lag of the load and the associated delay in the stall event. This is especially clear when $\alpha_M = 9$ deg. In particular, note how the peak response during

the upstroke is delayed to later in the cycle for $\Lambda = 30$ deg (dashed line) relative to $\Lambda = 0$ deg (solid line).

Parameter Analysis of Chordwise Pressures

The effect of mean angle of attack on the suction surface pressure response and on the influence of sweep at specific angles of attack is examined next. As examples, Figs. 47 and 48 show this effect at $\alpha = 7.4$ deg and 16.6 deg in the upstroke portion of the cycle. Each figure shows results at $M_c = 0.30$ (left column) and at $M_c = 0.40$ (right column) along with accompanying simple waveforms indicating the point in the motion cycle where the chordwise distributions were taken. Figure 47 contains results taken from the portion of the cycle where the unsteady aerodynamic activity is not in transition and is within the potential flow range of the motion. It is seen that the unswept and swept wing chordwise distributions in this part of the cycle are each nearly similar over the range of mean angle of attack shown at Mach numbers of 0.30 and 0.40 . This behavior, although not completely generalized, is encouraging from a data utilization standpoint in that this response distribution appears applicable (at this point of the motion cycle) over the entire range of mean incidence angles between $\alpha_M = 9$ deg and $\alpha_M = 15$ deg. With the exception of the upper left distributions, Fig. 48 shows that this similarity of the unswept and swept wing responses with respect to mean angle of attack tends to persist into the separated flow region. In particular, the chordwise distributions for each Mach number in Fig. 48 are very similar at $\alpha_M = 12$ deg and 15 deg while noticeably different at $\alpha_M = 9$ deg where the angle of attack value used in this comparison is near its peak. (It is again pointed out here that the jaggedness in the leading edge region response is an anomaly of the data which was explained earlier.) It is also noted in this figure that the effects of Mach number and sweep are substantial at this high value of angle of attack (16.6 deg), while the effect of Mach number at $\alpha = 7.4$ deg (cf. Fig. 47) is nearly imperceptible.

A further analysis of the $M_c = 0.30$ results corresponding to the previous two figures is presented in Figs. 49 and 50. As in Figs. 47 and 48, these figures show the effects of sweep and mean angle of attack on the chordwise distribution at various points of the motion cycle. Figure 49 shows the chordwise distributions at instantaneous angles of attack of $\alpha = 9, 11, 13,$ and 15 deg during upstroke (in columns from left to right) thus filling the gap between the results of Figs. 47 and 48 at 7.4 deg and 16.6 deg incidence, respectively. It is seen that the effect of varying α_M on the shape of the distribution (within each column) is relatively small over this range of angle of attack (within each row) for both the unswept and swept cases, implying that significant stall penetration has not yet taken place. It is also noted that the effect of sweep in reducing suction is consistent throughout this portion of the motion cycle.

A similar analysis is presented in Fig. 50 for the downstroke portion of the cycle over the same angle of attack range (where the plots are arranged following the motion from left to right). In this region the effects of sweep and mean angle of attack are each more significant than in Fig. 49. This is especially evident at $\alpha = 15$ deg (extreme left column) where flow reattachment is still underway. The sensitivity of the chordwise response to changes in mean angle of attack during the downstroke portion of the motion cycle occurs mainly because the aerodynamic activity is in varying stages of recovery from separation. This variation in the level of aerodynamic activity depends both on how deeply the stalled flow region was penetrated by the airfoil and on where the airfoil is in the motion cycle relative to peak incidence.

Effect of Sweep on Peak Angle of Attack Response

The effect of sweep on the peak angle of attack region response is now examined for $\alpha_M = 9, 12$ and 15 deg. Figures 51 and 52 show the sensitivity of the chordwise response to sweep in 0.5 degree increments within 1.5 deg of peak angle for each mean angle of attack case. Figure 51 shows the upstroke portion of the study while Fig. 52 shows the downstroke portion.

The effect of sweep on the 9 degree mean angle of attack configuration is examined first (see top row of Figs. 51 and 52). At $\alpha = 15.5$ deg in the top row in Fig. 51, the effect of sweep is still moderate as the airfoil motion enters the stall transition region of the cycle. A half degree later at $\alpha = 16.0$ deg, there is beginning evidence of collapse in suction for the unswept wing. This collapse progresses rapidly to maximum severity at peak angle while the loss in suction for the swept wing occurs in a more orderly fashion and does not reach the same intensity. As a result of this difference in the rate and magnitude of suction collapse, the unswept and swept wing chordwise load distributions are significantly different at peak angle of attack. Going on to the top row in Fig. 52 where the downstroke portion is presented, the change in both the unswept and swept wing responses becomes less severe with the change in angle of attack and the chordwise distributions appear to once again coalesce as α reaches 15.5 degrees.

The results for the 12 degree mean angle of attack configuration are shown in the middle row of both figures. In this case the motion is well into the stall region throughout the range of angles shown and the pressure distribution is still exhibiting the after-effects of transition between unstalled and stalled flow. This behavior is made more apparent by the extensive disagreement between the unswept and swept airfoil pressure distributions throughout the upstroke portion of the motion near peak angle of attack (Fig. 51). This sweep-induced difference becomes less severe as the motion passes through the peak and into the downstroke region (Fig. 52).

However, the strong disagreement at the leading edge persists throughout this range of angles. As shown earlier in the discussion of response time histories, this behavior is partly a consequence of the difference in the phasing of the recovery process between the unswept and swept wing responses relative to the airfoil pitching motion.

The behavior of the 15 degree mean angle of attack configuration is shown in the bottom row of Figs. 51 and 52. In this case, the chordwise distributions all occur very deep in the stall region, where flow separation is fully achieved, and are thus relatively stable to small changes in angle. At $\alpha = 21.5$ deg in Fig. 51, it is seen that the transition into fully separated flow is nearly completed. Once the transition is fully achieved, the unswept and swept distributions appear to coalesce and as the motion passes through peak angle of attack, the load distributions appear less dependent on sweep. It should be noted, however, that this latter observation can be misleading if it is not combined with a study of the corresponding time histories of Fig. 43 where it is seen that the close agreement between unswept and swept results is only transitory during the downstroke at $\tau = 0.33$ (right column).

DISCUSSION OF INTEGRATED LOAD RESULTS

The integrated load results (lift, drag, and moment) reported in Ref. 1 were computed from the chordwise response data of this report. Hysteresis loop comparisons were made therein to show the effect of sweep on the unsteady lift, drag, and moment components of the total force response. A particular feature that remained unexplained in the results is the substantial displacement in the lift curve below stall between the unswept and swept wing results, especially at high angles of attack. A perspective on this displacement can be obtained from Figs. 53 and 54. Figure 53 shows that the normalized steady-state lift curves of the unswept and swept NACA 0012 airfoils are nearly coalesced below stall. This is not the case when viewing the unsteady comparisons in Fig. 54. Here, it is seen that the upstroke portions of the unswept lift responses below stall are significantly and increasingly displaced from one another as α_M increases. (Figure 54 is a reproduction of results from Fig. 34 of Ref. 1 showing the effect of sweep on the lift response for four mean angles of attack tested at $M_c = 0.40$, $f = \text{Hz}$, and $\bar{\alpha} = 8 \text{ deg.}$)

It has been found that this displacement of the lift response is mainly associated with the first harmonic component. This was discovered serendipitously while attempting to superimpose the unsteady parts of the unswept and swept wing lift responses. In order to achieve this superposition effectively, the time mean components of the lift responses were removed in an attempt to bring the loops to closer alignment than shown in Fig. 54. The result of doing this is shown in the top row of Fig. 55 for the 15 degree mean angle of attack case where plot 55a is repeated from Fig. 54 and plot 55b is stripped of the time mean component. The resultant lack of change in the relative positioning of these loops indicates that, for this particular comparison, the entire displacement is a sweep-induced unsteady phenomenon. A harmonic analysis of these loops was performed to determine the aspect of the data that accounts for this displacement. It was found that the ultimate shape, displacement, and rotation of the lift loops of Fig. 55a are primarily governed by the first harmonic component ellipse. This is clearly illustrated by the first harmonic component comparison in plot 55c where the mid-portion of the ΔC_L upstroke displacement of the complete response (plot 55a) is accounted for. This first harmonic result shows that the primary influence of sweep on the total lift response is through the phasing between the first harmonic component of the lift response and the blade motion, and through the ratio of the first harmonic component amplitude of the response to the airfoil pitching amplitude. The remaining comparisons in Fig. 55 (plots d through h) show how the addition of higher harmonic terms contributes in evolving the complete unsteady response without significant influence on the ΔC_L displacement at the midpoint of the upstroke. From this example, it is seen that the main importance of the higher harmonic terms is

in shaping the loops rather than affecting their orientation. A comparison of plot 55d and plot 55b shows that most of the remaining features of the loops are due to the second harmonic term.

The analysis of the moment responses for the same unswept and swept cases shown in Fig. 55 is presented in Fig. 56. Unlike the lift result, it is seen that the removal of the nonoscillatory terms from the total values tends to bring the unswept and swept responses to closer proximity but with some displacement remaining. As in the case of the lift result the subsequent harmonic analysis of the moment response shows that the remaining displacement is due to the influence of sweep on the unsteady portion of the response and that the ultimate orientations are again largely determined by the first harmonic ellipses. In this case the influence of the second harmonic term (plot 56d) on the final shape is clearly evident.

Several additional sweep comparisons were analyzed and variations were observed in the source (unsteady or time mean) of the loop displacement from case to case. An example that illustrates this variation in the sweep influence (relative to that shown in Figs. 55 and 56) is presented next in Figs. 57 and 58.

The unswept and swept cases shown in these figures are the same in every respect to Figs. 55 and 56, except that $\alpha_M = 9$ deg. The results of the harmonic analysis of the lift in Fig. 57 is basically the same as before; however, Fig. 58 shows that, in this case, the displacement of the moment response is entirely accounted for by the nonoscillatory terms. As a result, note how the first harmonic ellipses are nearly coincident.

Taken together, the harmonic analysis presented in Figs. 55 through 58 show that the loop displacements range from being entirely dependent on the unsteady influence (cf. Fig. 55) to entirely dependent on the time mean influence (cf. Fig. 58). Therefore, what once appeared to be anomalous behavior (because of the inconsistent result obtained by removal of the time mean component from the total response) has been shown to be amenable to analysis.

SUMMARY OF RESULTS

An analysis was performed on unsteady aerodynamic pressure data from a NACA 0012 tunnel-spanning wing oscillating in the unswept and swept configuration. The range of parameters tested were: sweep, 0 and 30 degrees; pitching amplitude, 8 and 10 degrees; mean angle of attack, 0 to 15 degrees; Mach number normal to the wing span, 0.30 and 0.40; pitching frequency, 4 to 11 Hertz. The corresponding reduced frequency range of the data was .038 to .125.

The main subject areas of this report are: the analysis of the chordwise wave propagation speed, the analysis of the upper surface chordwise pressure distribution, and a brief harmonic analysis of the integrated lift response. The results of this study are summarized below. Items with asterisks are regarded as primary findings.

Pressure Wave Analysis

- Mean angle of attack has little or no effect on wave speed, which in all cases increases uniformly with reduced frequency (Figs. 16 through 20). Motion amplitude also has little or no effect on wave speed (Fig. 16). Mach number has a small but consistent effect on wave speed, with higher Mach numbers yielding slightly smaller wave speeds (Fig. 17).
- * ● Sweep angle has a dominant effect on wave speed. The overall wave speed for the unswept wing is consistently greater than that for the swept wing by a factor of 1.5 to 2.0 (Figs. 18 et seq.). This represents a major failure above stall for the cosine law normalization which has been shown to be consistently valid below stall.
- Previous observations of the effect of increasing sweep to delay stall are confirmed in the present work. In addition, the vortex inception angle increases slowly with k_c (Fig. 22).
- * ● Mach number has a dominant effect on vortex inception angle and static stall angle, with a decrease in both angles as M_c increases (Fig. 23).
- Vortex inception is substantially independent of amplitude of motion and of mean angle of attack (Figs. 22, 23).
- Local wave speed differences associated with sweep are confined to the region of the blade aft of the 15 percent chord. Wave speeds are

substantially the same for both sweep angles forward of this chord location (Figs. 19, 20). The variation of local wave speed with chordwise position shows an initial rapid increase near the leading edge followed by a leveling off of wave speed over the aft region of the chord (Fig. 21). Overall wave speed (averaged over the first 15 percent of the chord) agrees well with previous results from Ref. 4 (Fig. 15).

- * ● The vortex inception angle is independent of pitch rate when reduced frequency is fixed (Fig. 25).

Chordwise Pressures Analysis

- Sweep effects on the upper surface pressure distribution are more prevalent when the aerodynamic response is in transition between unstalled and stalled conditions.
- The sensitivity of the pressure responses to sweep is also strongest when the wing angle of attack is near peak value for mean angles of attack of 9, 12, and 15 degrees (Figs. 34, 35, and 36).
- * ● Sweep similarity by means of the cosine law (which prevails over the angle of attack range of ± 8 degrees about zero mean angle) deteriorates when the mean angle of attack reaches 9 degrees and the motion penetrates stall (Figs. 43 and 46).
- The effects of sweep very near peak angle appear stronger on the approach to than on recession from peak angle when $\alpha_M = 9$ deg while the opposite appears to be the case when $\alpha_M = 12$ deg. The effects of sweep at $\alpha_M = 15$ deg, on the other hand, are relatively small near peak angle (Figs. 51 and 52).
- * ● The reduced frequency parameter is not a reliable indicator of the unsteady aerodynamic condition at high angles of attack. This is because the same numerical value of reduced frequency can be obtained for two different combinations of M_c and f in which the M_c effect on the flow dominates the effect of f (Figs. 37 and 38).

Integrated Load Analysis

- * ● The main influence of sweep on the total integrated lift and moment responses is very strongly determined by the first harmonic term. This result implies that the effect of sweep on the unsteady response is amenable to analysis (Fig. 55).

APPENDIX

DISCUSSION OF MEASUREMENT ERROR

A minor measurement error was detected during the present analysis that occurs throughout the data set. This error neither affects the discussion presented herein nor does it alter the conclusions previously reported in Ref. 1 (based on the same data set).

The main evidence of the error is the jaggedness that occurs in both the upper surface chordwise pressure distribution plots and the constant pressure contours of the chordwise wave speed analysis. For the chordwise distribution plots, this anomaly ranges from slight to relatively large depending on the pressure loading condition. In the case of the constant pressure contours the effect is generally minor and, at worst, is more a nuisance than a detriment to the evaluation of the wave speed.

A close inspection of the first harmonic component phase angle distribution along the chord in Fig. 4 shows that the jaggedness (seen in Fig. 5 for example) is principally related to a phasing error between consecutive pressure responses along the chord. In particular, it is noted that the phase angle plots near the leading edge appear to be scattered about a mean trend. This behavior of the data set was found to be caused by a misalignment of the tape heads of the analog tape recorders. Both the read and write functions were configured to utilize two heads during record and playback where the odd and even numbered channels (sequentially assigned along the chord) were segregated to separate heads.

Under these circumstances, the time lag between odd and even channels due to head misalignment caused an odd-even channel phase error. This phase error, Δ , is related to the oscillation period, T , and tape speed, S , by the equation

$$\frac{\Delta\varphi}{360^\circ} = \Delta\tau = \frac{\Delta t}{T} = f \Delta t = f \frac{\Delta x}{S}$$

where Δx represents the error displacement between the heads. A typical value of Δx equal to .003 in. produces a phase angle error of 5 deg in the first harmonic at $f = 8$ Hz.

The entire data set was uniformly corrected for the computations made in the wave speed analysis, but the corrections were confined to that section only. All other figures presented in this report and the data tables in Ref. 3 remain uncorrected to preserve consistency with the results of Refs. 1 and 2.

REFERENCES

1. St. Hilaire, A. O., F. O. Carta, M. R. Fink and W. D. Jepson: The Influence of Wing Sweep on the Aerodynamic Loading of an Oscillating NACA 0012 Airfoil. Volume I - Technical Report. NASA CR-3092, 1979.
2. St. Hilaire, A. O. and F. O. Carta: The Influence of Sweep on the Aerodynamic Loading of an Oscillating NACA 0012 Airfoil. Volume II - Data Report. NASA CR-145350, 1979.
3. St. Hilaire, A. O. and F. O. Carta: Analysis of Unswept and Swept Wing Chordwise Pressure Data from an Oscillating NACA 0012 Airfoil Experiment. Volume II - Data Report. NASA CR-165927, 1983.
4. Carta, F. O.: Analysis of Oscillatory Pressure Data Including Dynamic Stall Effects. NASA CR-2394, May 1974.
5. Harris, F. D.: Preliminary Study of Radial Flow Effects on Rotor Blades. Journal of the American Helicopter Society. Vol. 11, No. 3, July 1966.
6. Purser, P. E. and M. L. Spearman: Wind Tunnel Tests at Low Speed of Swept and Yawed Wings Having Various Plan Forms. NACA Technical Note 2445, December 1951.
7. Carta, F. O., G. L. Commerford, R. G. Carlson and R. H. Blackwell: Investigation of Airfoil Dynamic Stall and Its Influence on Helicopter Control Loads. USAAMRDL Technical Report 72-51, September 1972.
8. Halfman, R. L., H. C. Johnson and S. M. Haley: Evaluation of High-Angle-of-Attack Aerodynamic-Derivative Data and Stall-Flutter Prediction Techniques. NACA Technical note 2533, November 1951.
9. Gormont, R. E.: A Mathematical Model of Unsteady Aerodynamics and Radial Flow for Application to Helicopter Rotors. USAAMRDL Technical Report 72-67, May 1973.
10. Liiva, J., F. J. Davenport, L. Gray, and I. C. Walton: Two-Dimensional Tests of Airfoils Oscillating Near Stall. Volumes I and II. USAAVLABS Tech. Rep. 68-13A, U.S. Army, Apr. 1968. (Available from DTIC as AD 670 957.)
11. Gross, D. W. and F. D. Harris: Prediction of Inflight Stalled Airloads from Oscillating Airfoil Data. Presented at the 25th Annual National Forum of the American Helicopter Society, Washington, D.C., May 1969.

TABLE 1

UNSTEADY TEST MATRIX FOR NACA0012 AIRFOIL

Airfoil	Λ (deg)	$\bar{\alpha}$ (deg)	α_M (deg)	M_∞	M_C	f(cps)					
						4	5.33	6	8	10	10.67
NACA0012 ↓	0 ↓	8 ↓ 10 ↓	0	.3	.3	X			X	X	
			"	.4	.4	X			X	X	
			9	.3	.3	X			X	X	
			"	.4	.4	X			X	X	
			12	.3	.3	X			X	X	
			"	.4	.4	X			X	X	
			15	.3	.3	X			X	X	
			"	.4	.4	X			X	X	
			0	.3	.3	X			X	X	
			"	.4	.4	X			X	X	
			9	.3	.3	X			X	X	
			"	.4	.4	X			X	X	
			12	.3	.3	X			X	X	
			"	.4	.4	X			X	X	
NACA0012 ↓	30 ↓	8 ↓ 10 ↓	0	.346	.3	X		X	X	X	
			"	.462	.4	X	X		X	X	X
			9	.346	.3	X		X	X	X	
			"	.462	.4	X	X		X	X	X
			12	.346	.3	X	X	X	X	X	
			"	.462	.4	X	X		X	X	X
			15	.346	.3	X		X	X	X	
			"	.462	.4	X	X		X	X	X
			9	.346	.3	X		X	X	X	
			"	.462	.4	X	X		X	X	X
			12	.346	.3	X		X	X	X	
			"	.462	.4	X	X		X	X	X
			15	.346	.3	X		X	X	X	
			"	.462	.4	X	X		X	X	X

TABLE 2

NOMINAL VALUES OF k_c FOR BASIC TEST PROGRAM

$M_c =$ f (cps)	0.3	0.4
	VALUES OF k_c	
4	.051	.038
5.33	.067	.051
6	.076	
8	.102	.076
10	.127	.095
10.67		.102

Notes:

1. All values displayed were run at least once.
2. Horizontal arrows on right column denote nominal values used for unswept runs.
3. Boxed numbers denote nominal values used for swept runs.
4. Diagonal arrows indicate matched values of k_c .

TABLE 3

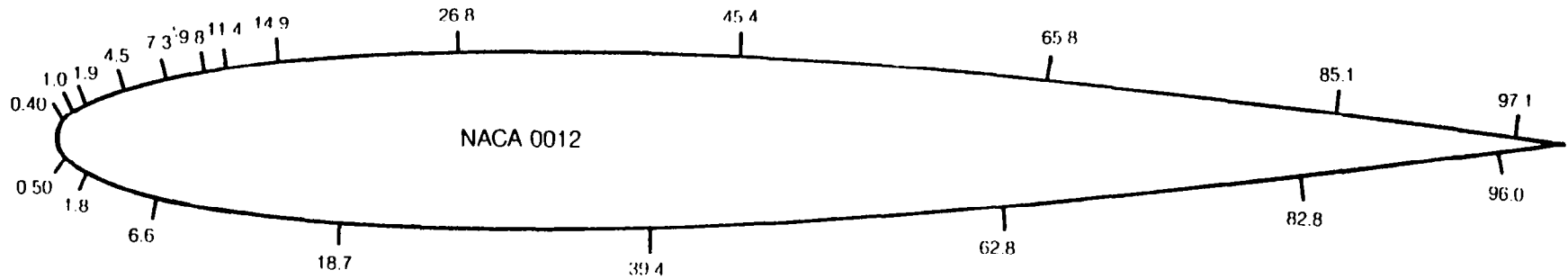
		α_{Vo}		α_{ss}	
		Least Squares intercept at $k_c=0$		Steady State Based on $dC_M/d\alpha=0$	
M_c	$\bar{\alpha}$	$\Lambda=0^\circ$	$\Lambda=30^\circ$	$\Lambda=0^\circ$	$\Lambda=30^\circ$
.3	8°	14.4°	15.0°	12.9°	12.8°
	10°	14.5°	14.5°		
.4	8°	10.3°	11.4°	10.4°	10.4°
	10°	9.9°	10.6°		

TABLE 4

	α_M (deg)	k_c	τ_o	α_v (deg)	ϵ (deg)	A_v	
$\Lambda=0$ deg $M_c=0.3$ $\alpha=8$ deg	9	.0498	.137	15.07	.423	.0045	$\alpha_{vo}=14.43^\circ$ $M_c=4.330^\circ$
		.0993	.125	14.66	-.202	.0098	
		.1245	.123	14.58	-.391	.0125	
	12	.0497	.052	14.57	-.077	.0066	
		.1001	.057	14.80	-.065	.0131	
		.1249	.066	15.22	.247	.0160	
	15	.0497	.987	14.35	-.297	.0069	
		.1002	.000	15.00	.134	.0140	
		.1248	.004	15.20	.228	.0174	
$\Lambda=0$ deg $M_c=3.0$ $\alpha=10$ deg	9	.0499	.094	14.57	-.334	.0072	$\alpha_{vo}=14.53^\circ$ $M_c=7.454^\circ$
		.0997	.104	15.08	-.195	.0138	
		.1250	.110	15.37	-.093	.0168	
	12	.0497	.051	15.15	.248	.0082	
		.1006	.061	15.74	.459	.0163	
		.1265	.055	15.39	-.085	.0208	
$\Lambda=0$ deg $M_c=0.4$ $\alpha=8$ deg	9	.0374	.050	11.47	.908	.0050	$\alpha_{vo}=10.26^\circ$ $M_c=8.177^\circ$
		.0742	.033	10.65	-.213	.0101	
		.0929	.045	11.23	.214	.0125	
	12	.0374	.969	10.45	-.112	.0051	
		.0749	.986	11.30	.431	.0104	
		.0939	.991	11.55	.526	.0131	
	15	.0373	.889	9.86	-.701	.0040	
		.0751	.902	10.38	-.491	.0086	
		.0935	.904	10.46	-.561	.0108	
$\Lambda=0$ deg $M_c=0.4$ $\alpha=10$ deg	9	.0374	.026	10.63	-.054	.0064	$\alpha_{vo}=9.94^\circ$ $M_c=20.023^\circ$
		.0746	.033	11.06	-.369	.0127	
		.0934	.042	11.61	-.196	.0157	
	12	.0376	.979	10.68	-.008	.0065	
		.0749	.000	12.00	.565	.0131	
		.0935	.998	11.87	.062	.0163	
$\Lambda=30$ deg $M_c=0.3$ $\alpha=8$ deg	9	.0502	.138	15.10	-.185	.0045	$\alpha_{vo}=14.98^\circ$ $M_c=6.026^\circ$
		.0756	.144	15.29	-.148	.0065	
		.1003	.149	15.44	-.147	.0083	
		.1259	.145	15.32	-.421	.0108	
		.0498	.065	15.18	-.103	.0064	
		.0656	.074	15.59	.212	.0082	
		.0750	.071	15.45	.015	.0095	
		.0996	.079	15.81	.227	.0122	
		.1244	.074	15.59	-.142	.0155	
	12	.0503	.060	14.94	-.346	.0065	
		.1003	.077	15.72	.133	.0124	
		.0503	.013	15.65	.364	.0070	
		.0758	.009	15.45	.011	.0106	
		.1000	.018	15.90	.315	.0139	
		.1246	.019	15.95	.216	.0173	

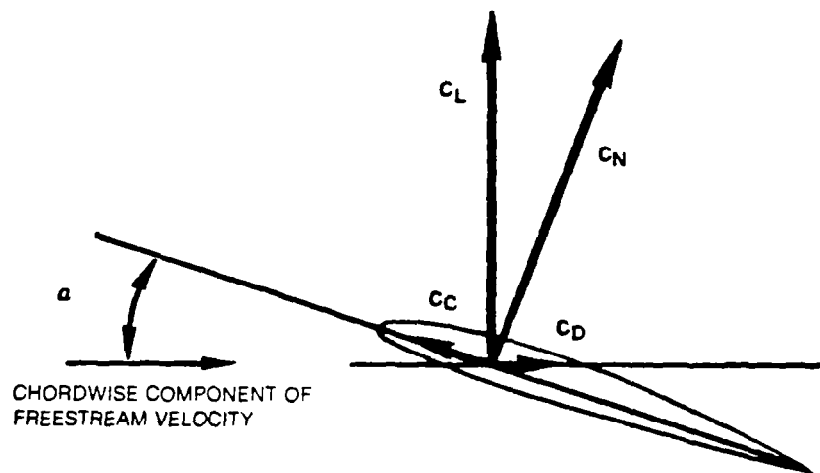
TABLE 4 (Concluded)

	α_M (deg)	k_c	τ_o	α_v (deg)	ϵ (deg)	A_v	
$\Lambda=30$ deg $M_c=0.3$ $\alpha=10$ deg	9	.0498	.102	14.98	-.111	.0070	$\alpha_{vo}=14.51^\circ$ $M_c=11.576^\circ$
		.0750	.110	15.37	-.013	.0101	
		.0994	.114	15.57	-.095	.0131	
	12	.1241	.115	15.61	-.341	.0163	
		.0497	.049	15.03	-.060	.0083	
		.0754	.050	15.09	-.297	.0125	
	15	.0995	.060	15.68	.014	.0162	
		.1241	.066	16.03	.079	.0198	
		.0499	.005	15.31	.218	.0087	
		.0754	.008	15.50	.113	.0131	
		.0995	.010	15.63	-.036	.0173	
		.1239	.018	16.13	.181	.0215	
		.0983	.016	16.00	.348	.0171	
$\Lambda=30$ deg $M_c=0.4$ $\alpha=8$ deg	9	.0377	.051	11.52	-.269	.0050	$\alpha_{vo}=11.36^\circ$ $M_c=11.487^\circ$
		.0502	.055	11.71	-.223	.0066	
		.0754	.050	11.47	-.752	.0100	
	12	.0945	.069	12.36	.033	.0107	
		.1002	.068	12.32	-.187	.0127	
		.0376	.003	12.15	.362	.0052	
		.0496	.010	12.50	.574	.0069	
		.0745	.014	12.70	.488	.0104	
		.0933	.016	12.80	.372	.0130	
	15	.0992	.015	12.75	.254	.0138	
		.0377	.998	11.90	.111	.0053	
		.0753	.002	12.10	-.121	.0105	
		.0376	.929	11.55	-.238	.0047	
		.0499	.934	11.78	-.149	.0064	
		.0751	.941	12.10	-.119	.0098	
$\Lambda=30$ deg $M_c=0.4$ $\alpha=10$ deg	9	.0371	.035	11.18	-.107	.0063	$\alpha_{vo}=10.61^\circ$ $M_c=18.254^\circ$
		.0495	.042	11.61	.096	.0083	
		.0743	.045	11.79	-.176	.0125	
	12	.0929	.050	12.09	-.216	.0154	
		.0990	.052	12.21	-.207	.0164	
		.0375	.989	11.31	.016	.0065	
		.0497	.992	11.50	-.017	.0087	
		.0746	.003	12.19	.218	.0130	
		.0935	.000	12.00	-.317	.0163	
	15	.0992	.010	12.63	.209	.0173	
		.0374	.935	11.03	-.263	.0060	
		.0494	.949	11.85	.338	.0082	
		.0740	.953	12.09	.129	.0124	
		.0934	.957	12.33	.015	.0157	
		.0991	.963	12.70	.281	.0168	



TIC MARKS AND NUMBERS INDICATE PRESSURE MEASURING STATIONS ALONG REFERENCE LINE, PERCENT CHORD

Fig. 1 Airfoil Cross Section Showing Chordwise Measuring Stations Along Reference Line



$$C_D = C_N \sin \alpha - C_C \cos \alpha$$

$$C_L = C_N \cos \alpha + C_C \sin \alpha$$

Fig. 2 Airfoil Force Schematic

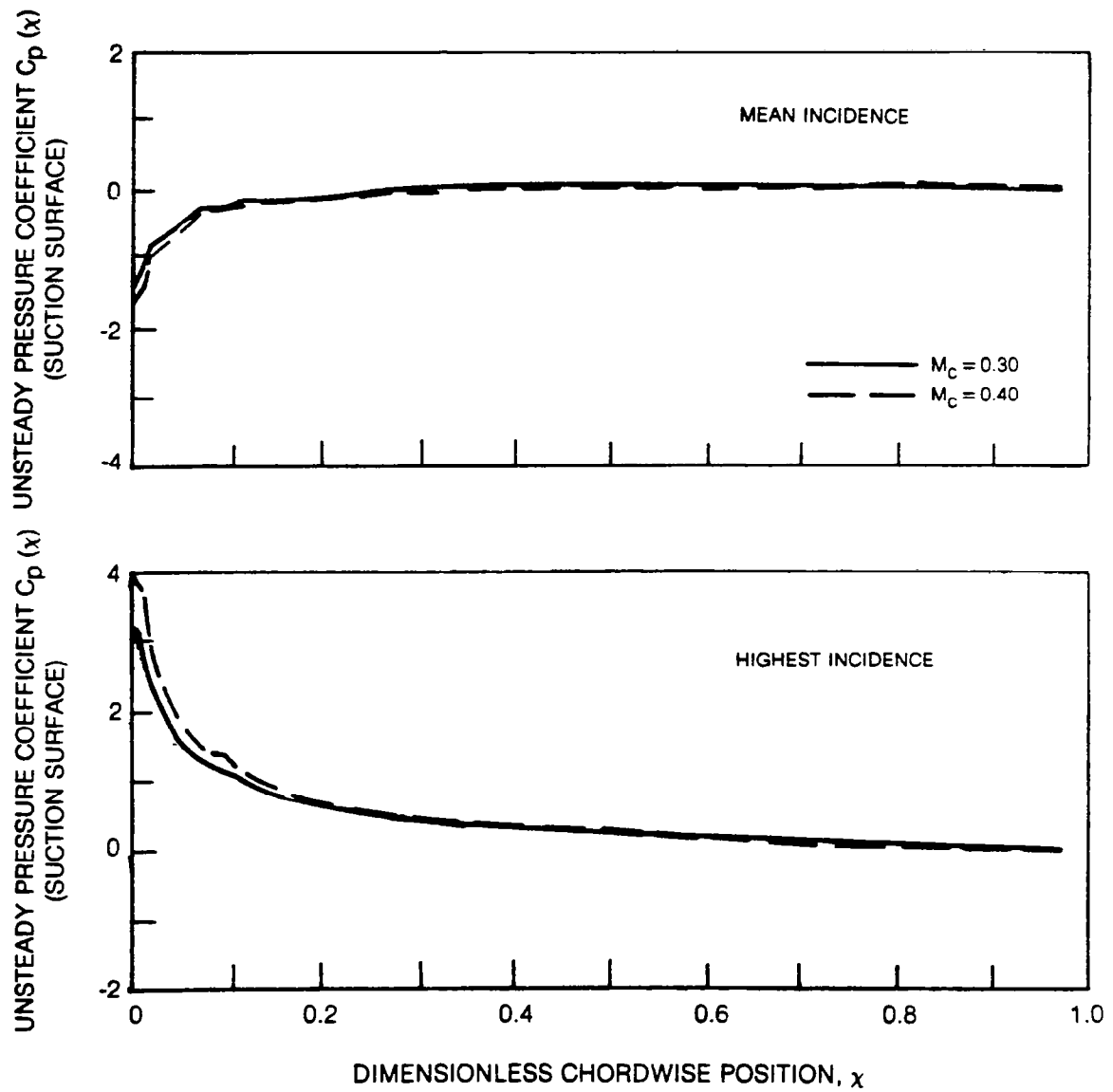


Fig. 3 Example of Chordwise Pressure Distribution Comparison — Continuous Curves

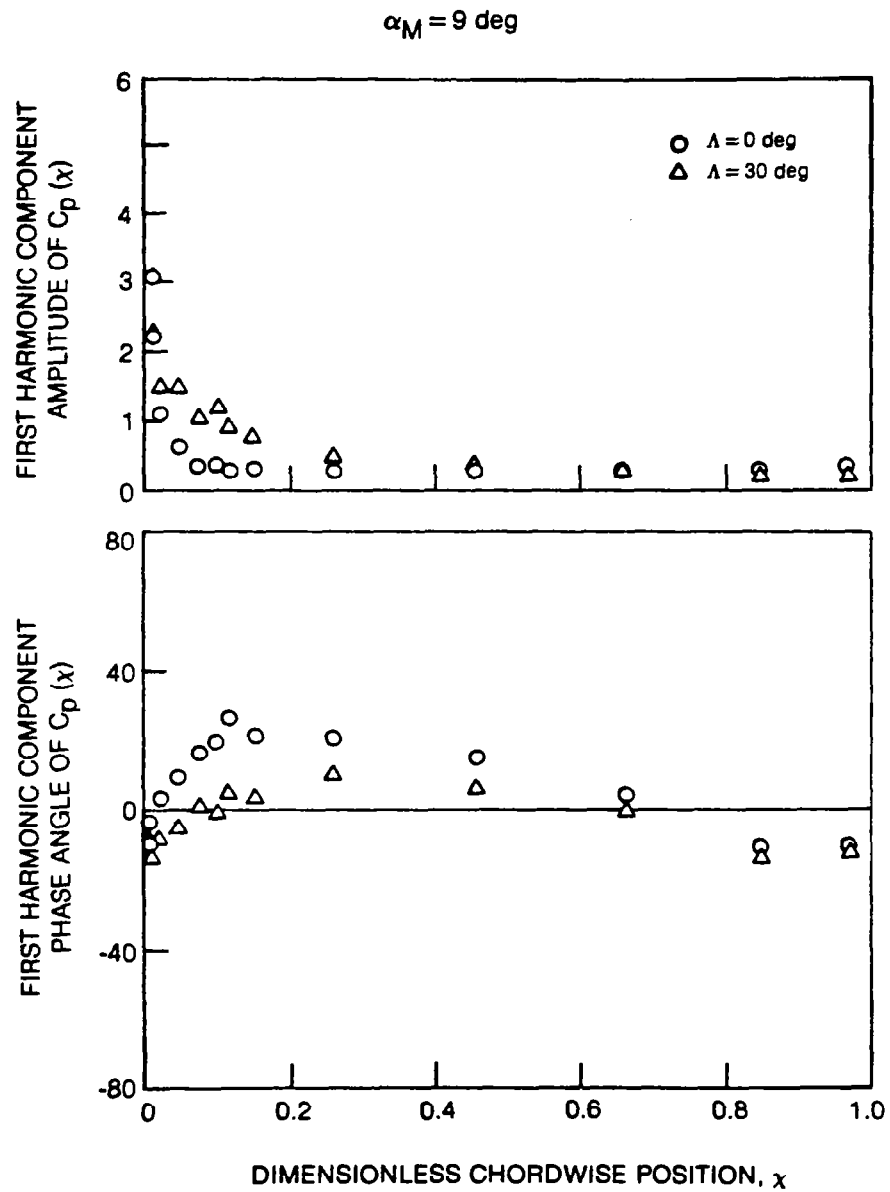


Fig. 4 Example of Chordwise Pressure Distribution Comparison — Discrete Points

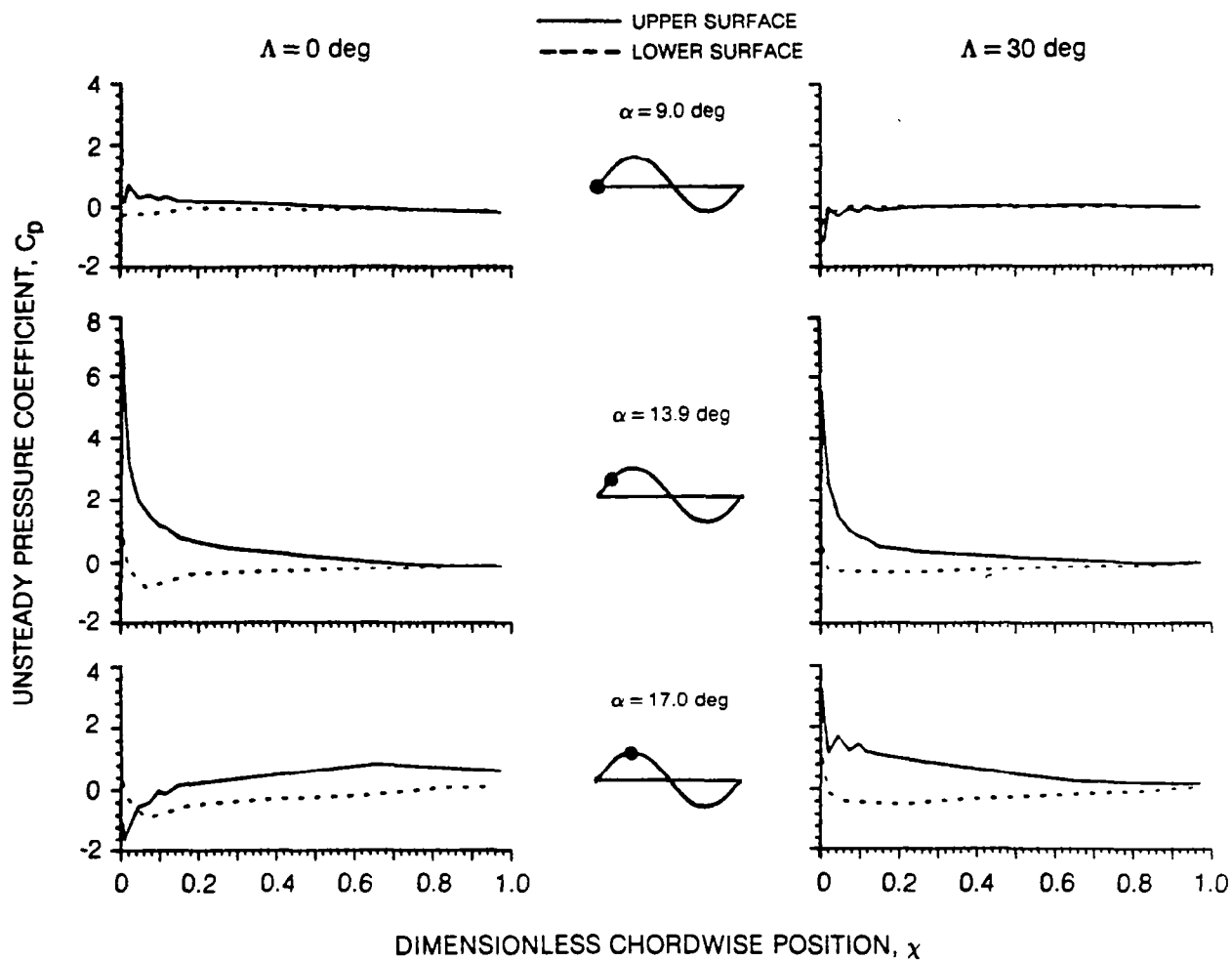


Fig. 5 Example of Chordwise Pressure Distribution Format for Comparison of Adjacent Columns

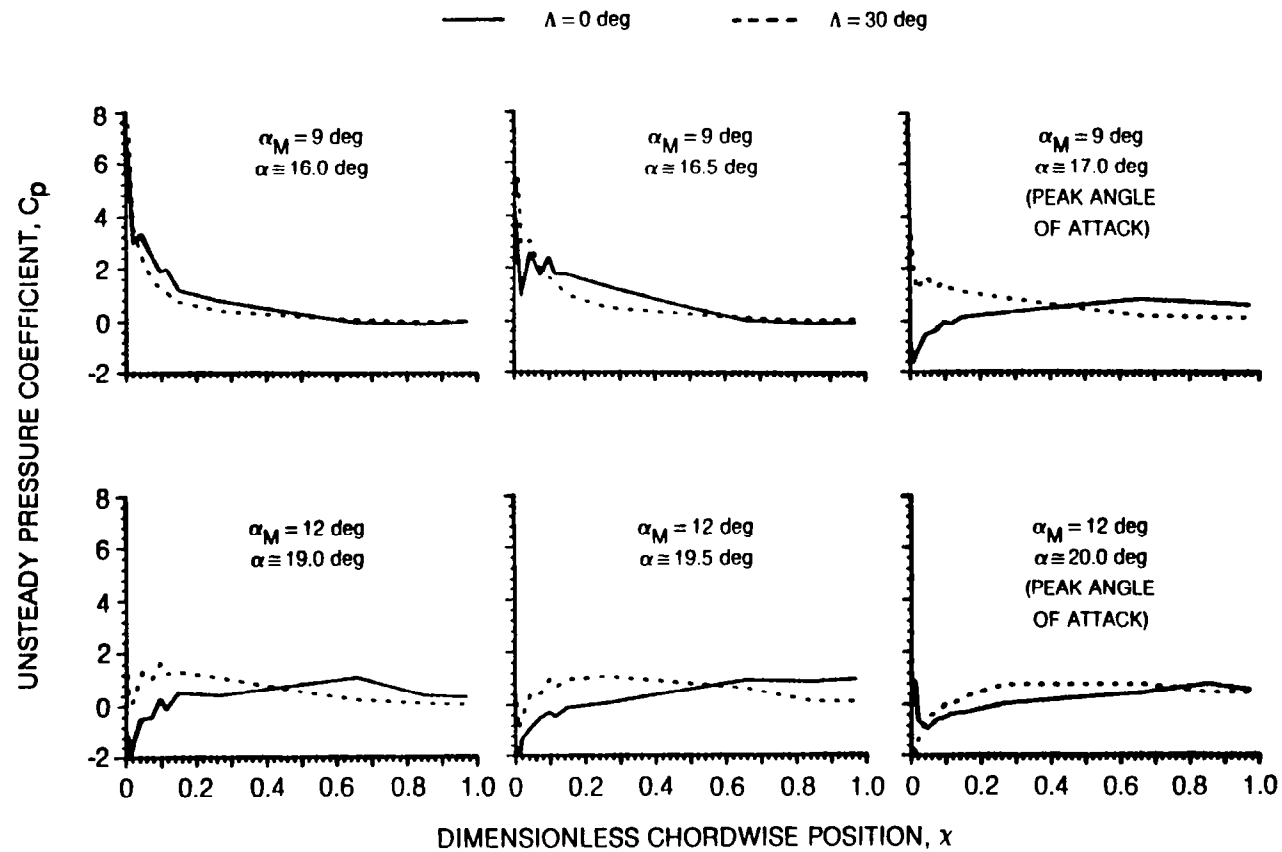


Fig. 6 Example of Chordwise Pressure Distribution Format for Trend Analysis

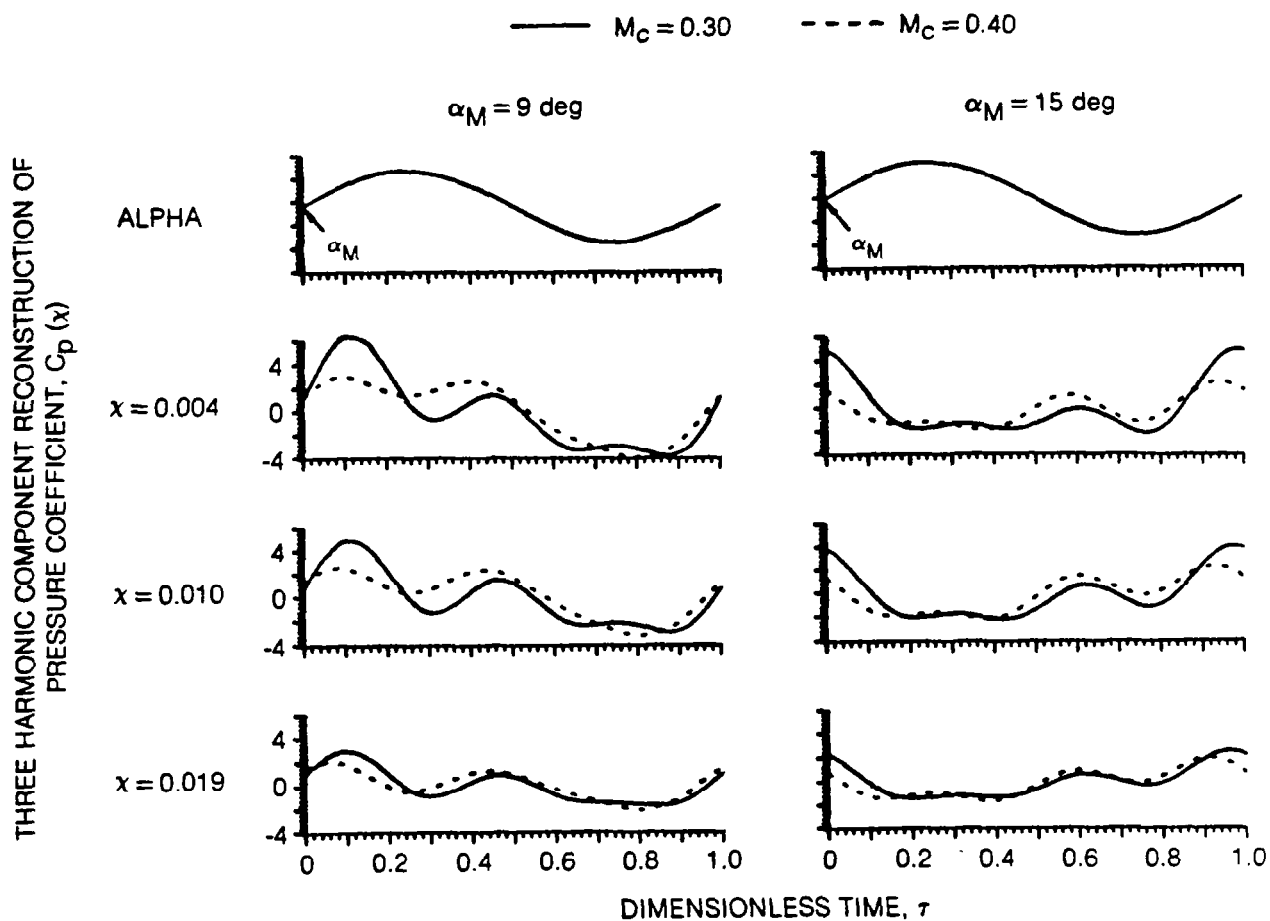


Fig. 7 Example of Pressure Time History Format for Comparison or Trend Analysis

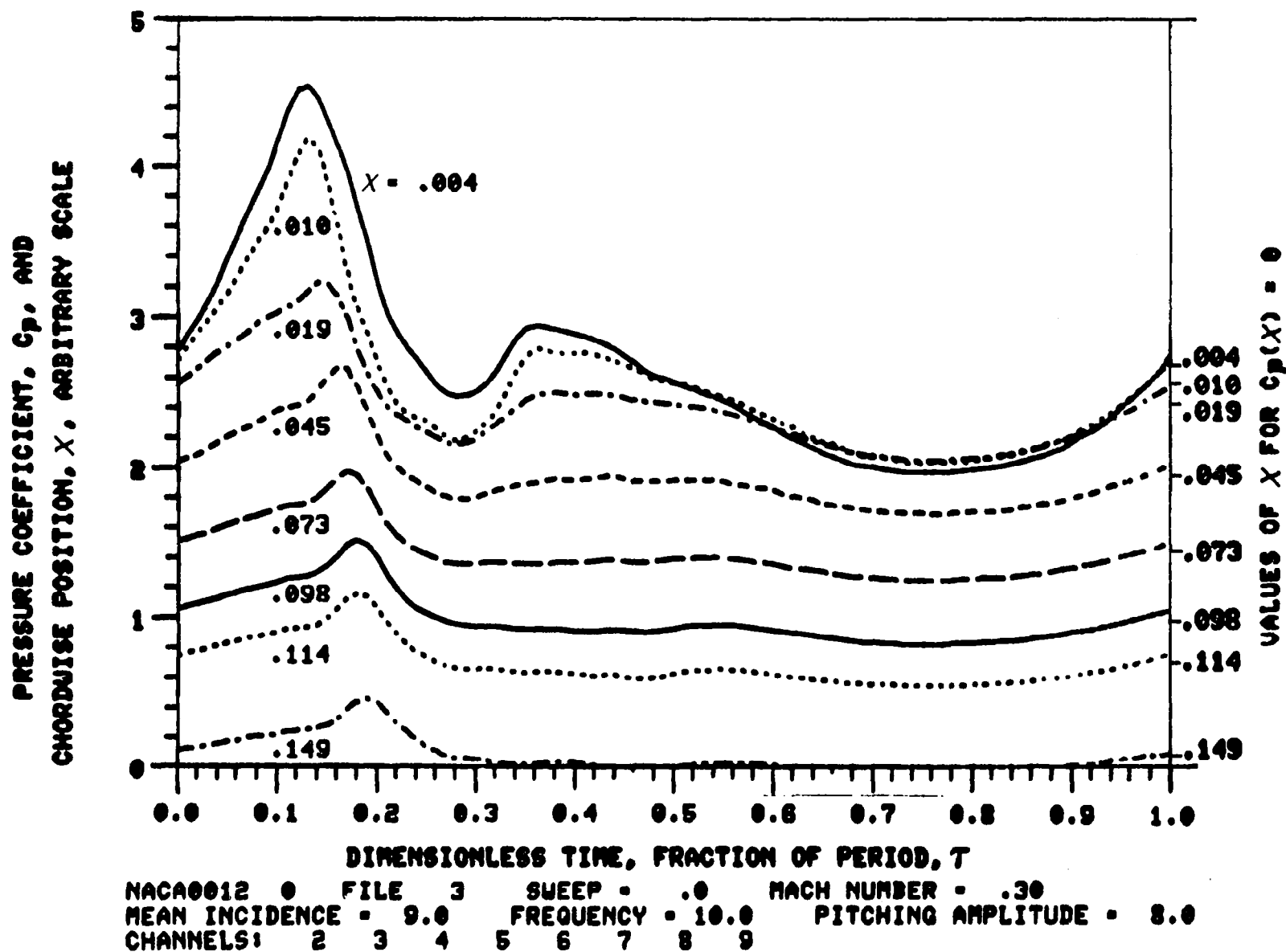


Fig. 8 Pressure Carpet Plot, Leading Edge Region

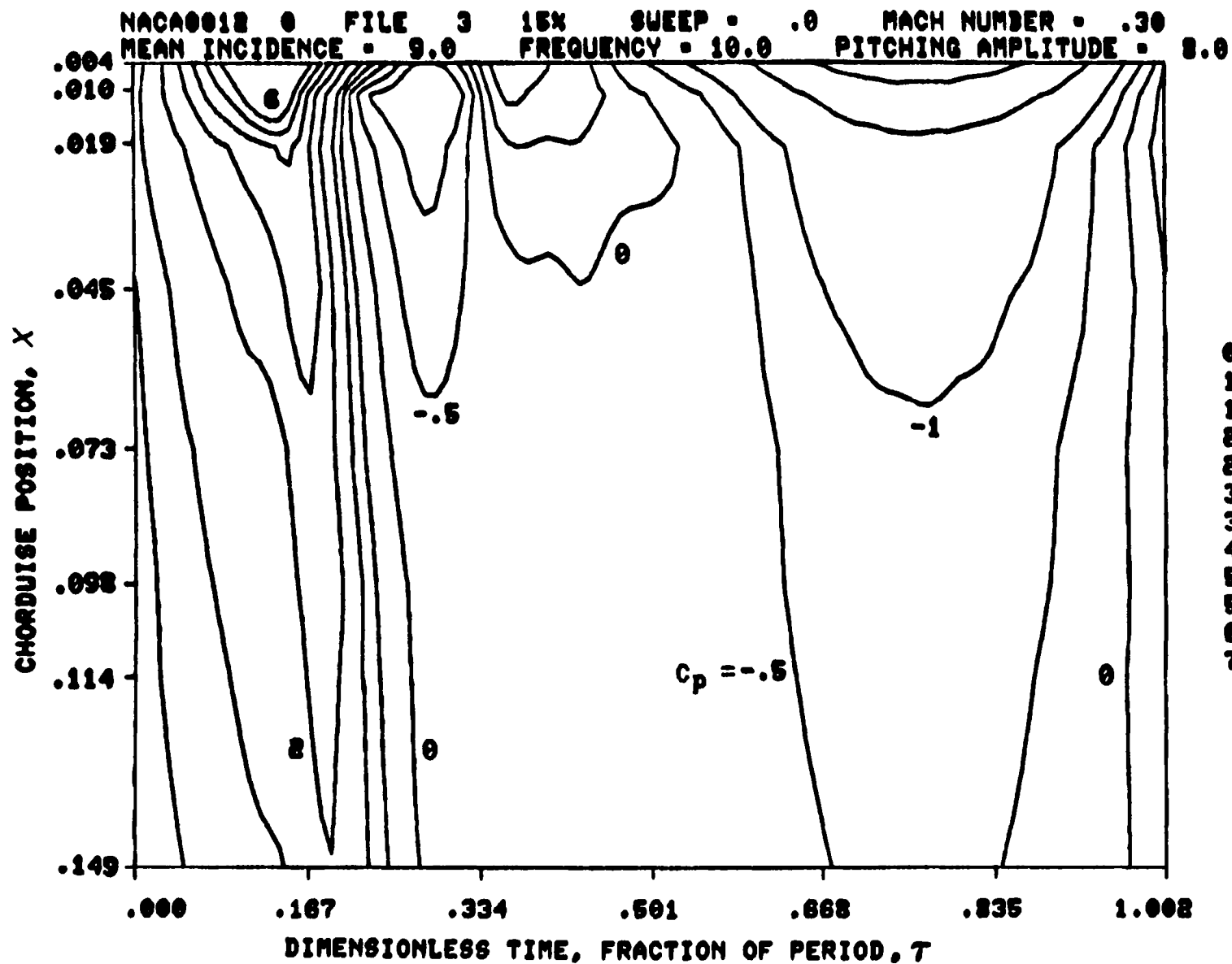
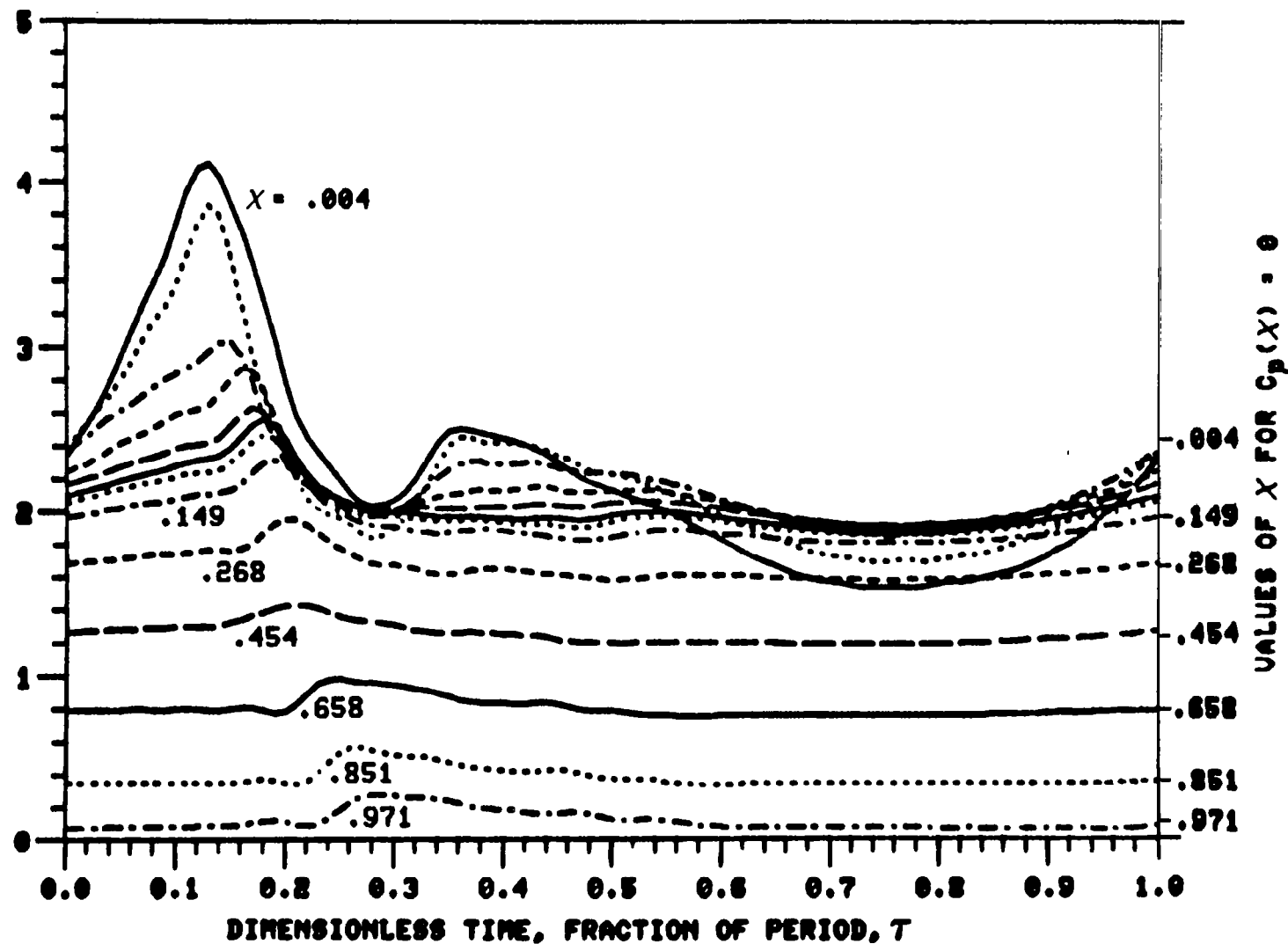


Fig. 9 Pressure Contour Map, Leading Edge Region

PRESSURE COEFFICIENT, C_p , AND
CHORDWISE POSITION, X , ARBITRARY SCALE



NACA0012 • FILE 3 SWEEP = .0 MACH NUMBER = .30
MEAN INCIDENCE = 9.0 FREQUENCY = 10.0 PITCHING AMPLITUDE = 8.0
CHANNELS: 2 3 4 5 6 7 8 9 10 11 12 13 14

Fig. 10 Pressure Carpet Plot, Entire Chord

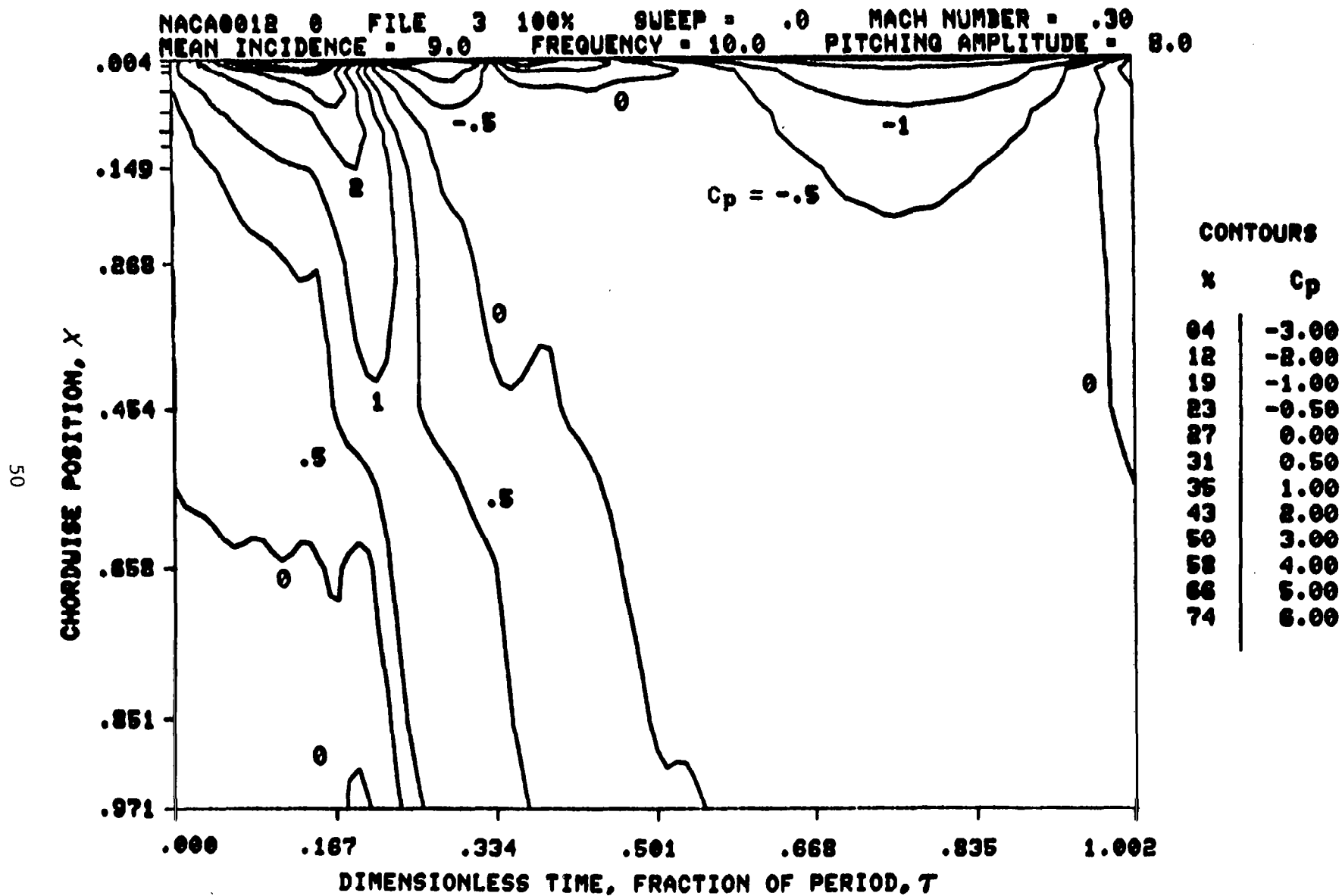


Fig. 11 Pressure Contour Map, Entire Chord

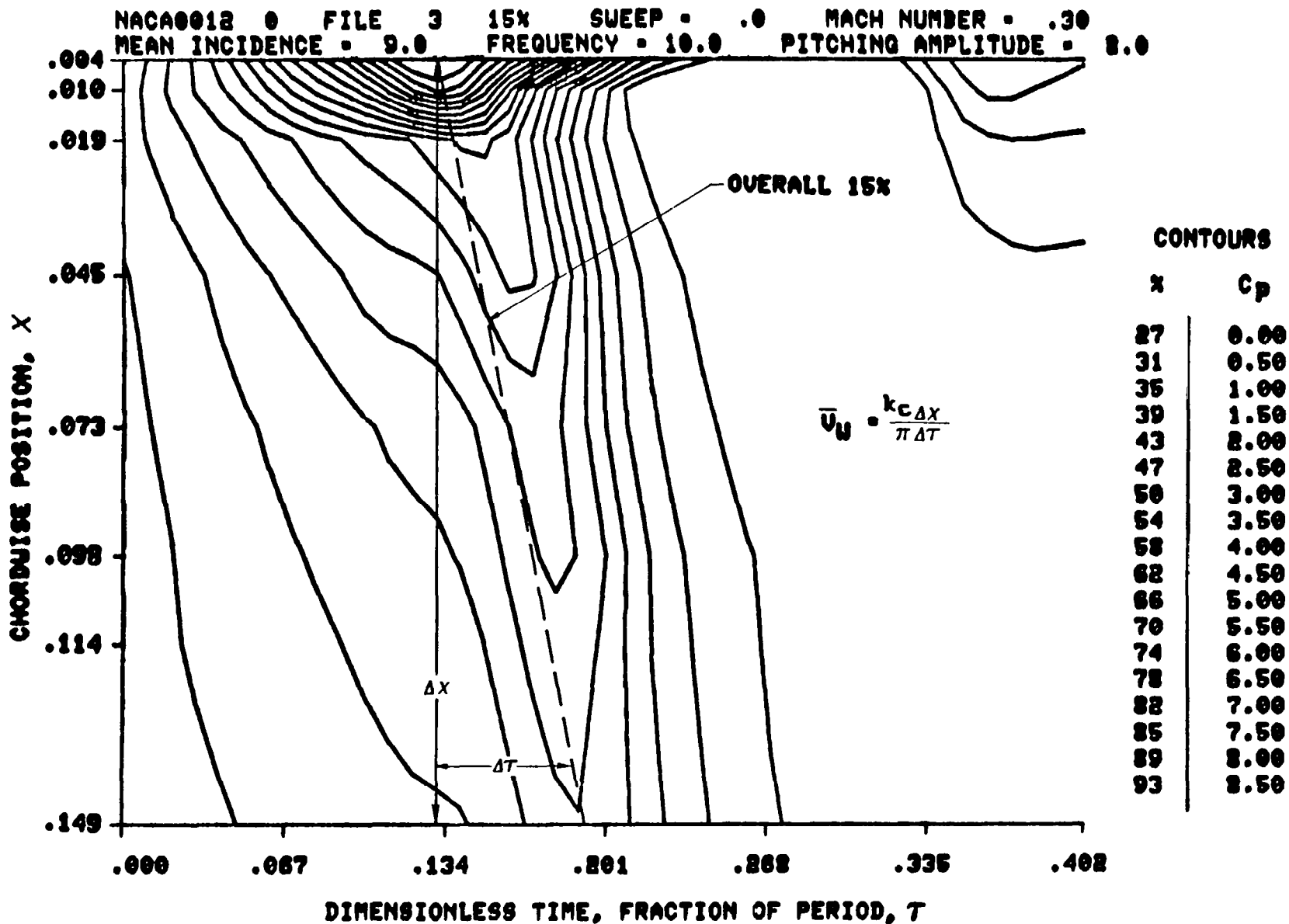


Fig. 12 Pressure Contour Map with Wave Speed Definition, Near Leading Edge

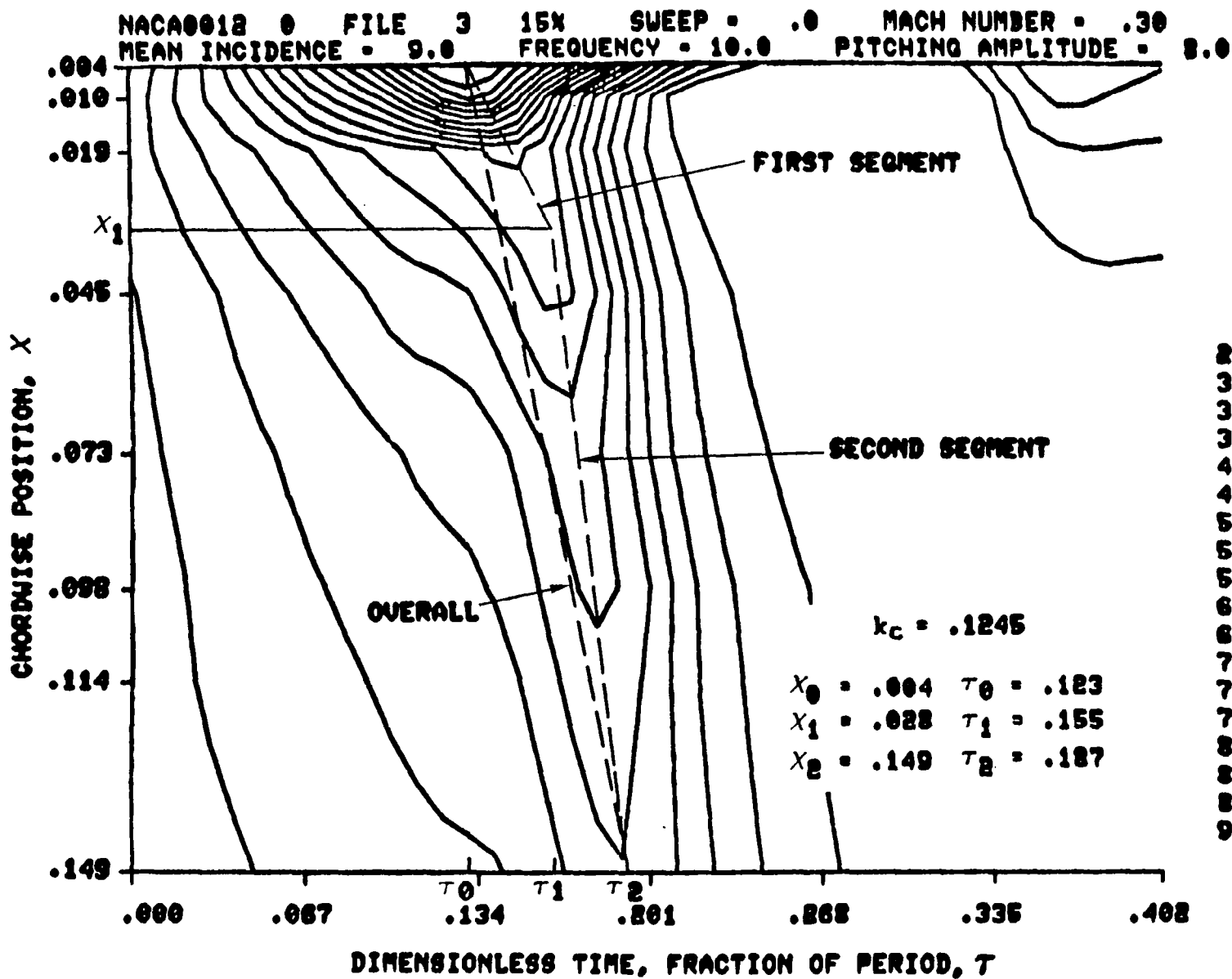


Fig. 13 Illustration of Segmented Wave Speed Near Leading Edge

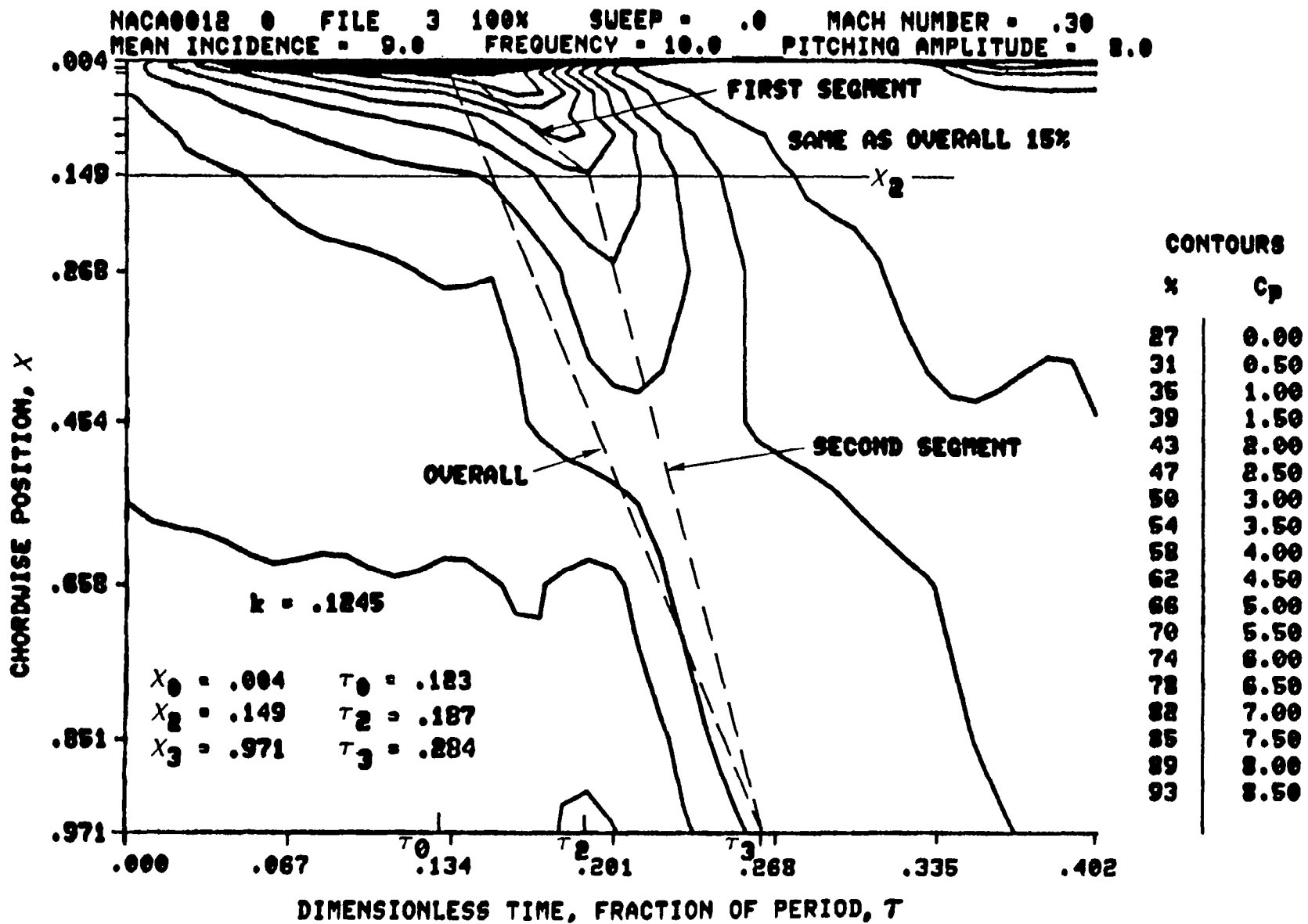


Fig. 14 Illustration of Segmented Wave Speed Over Entire Blade

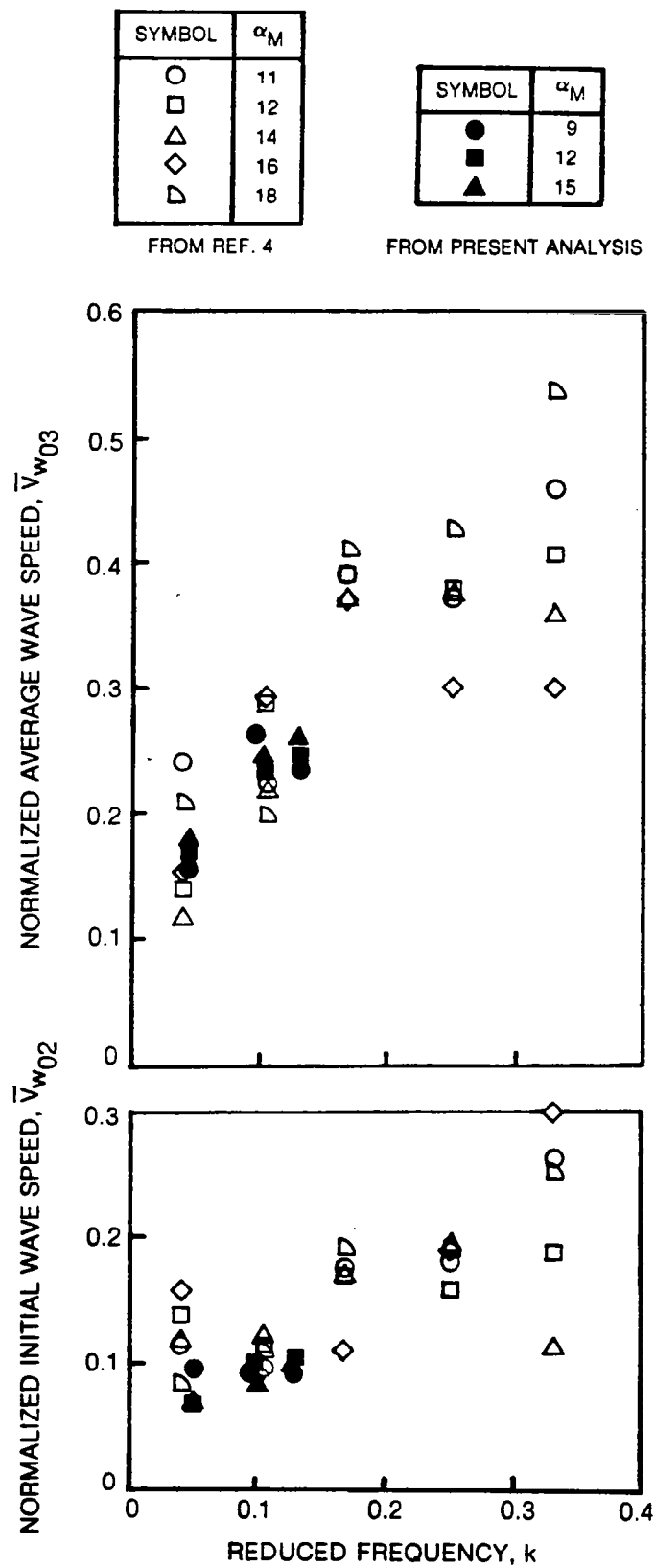


Fig. 15 Variation of Normalized Wave Speeds with Frequency.
 (In Ref. 4 \bar{V}_{w02} was Denoted \bar{V}_{w1} and \bar{V}_{w03} was Denoted \bar{V}_w)

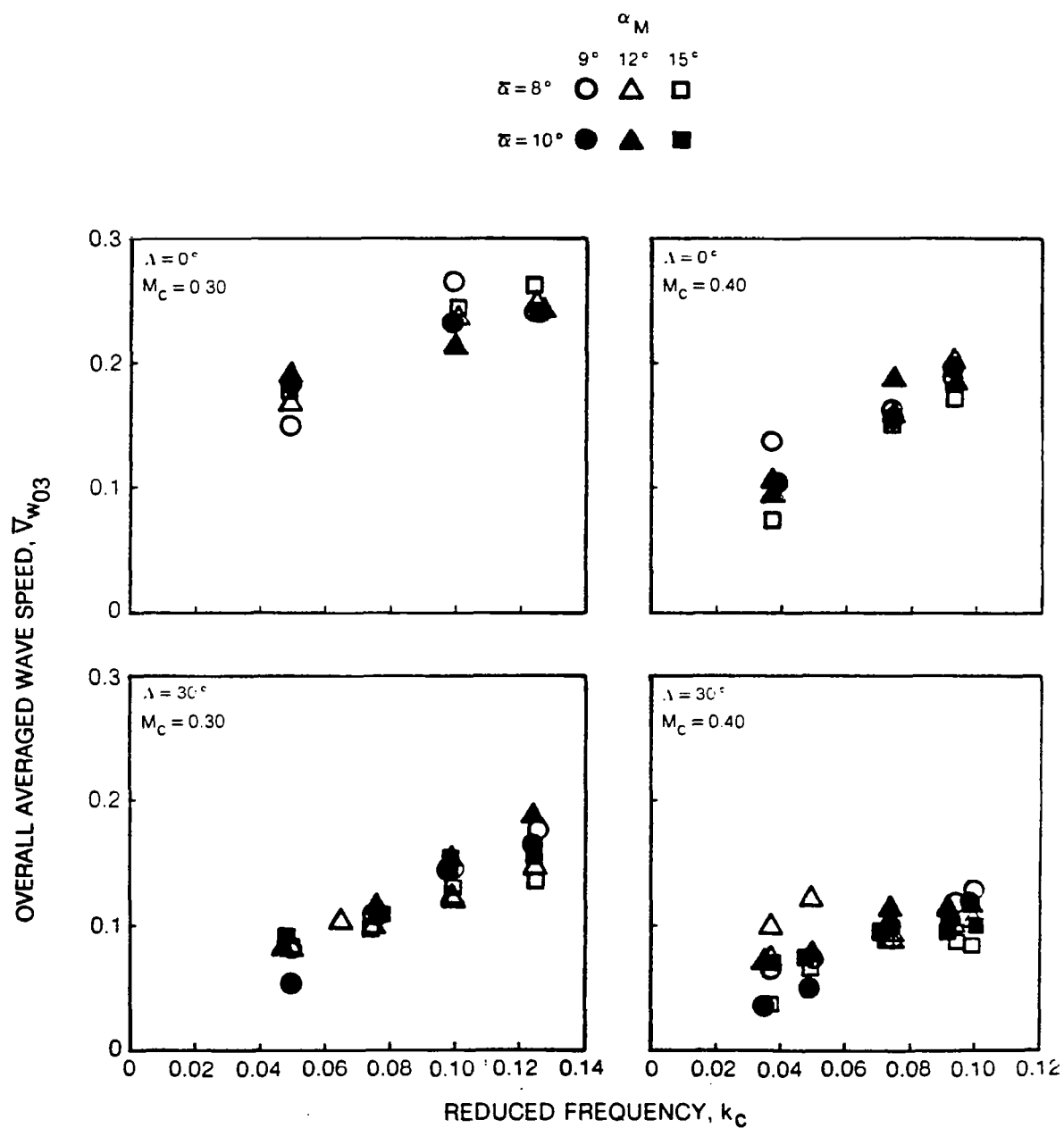


Fig. 16 Effect of Pitching Amplitude on Overall Wave Speed

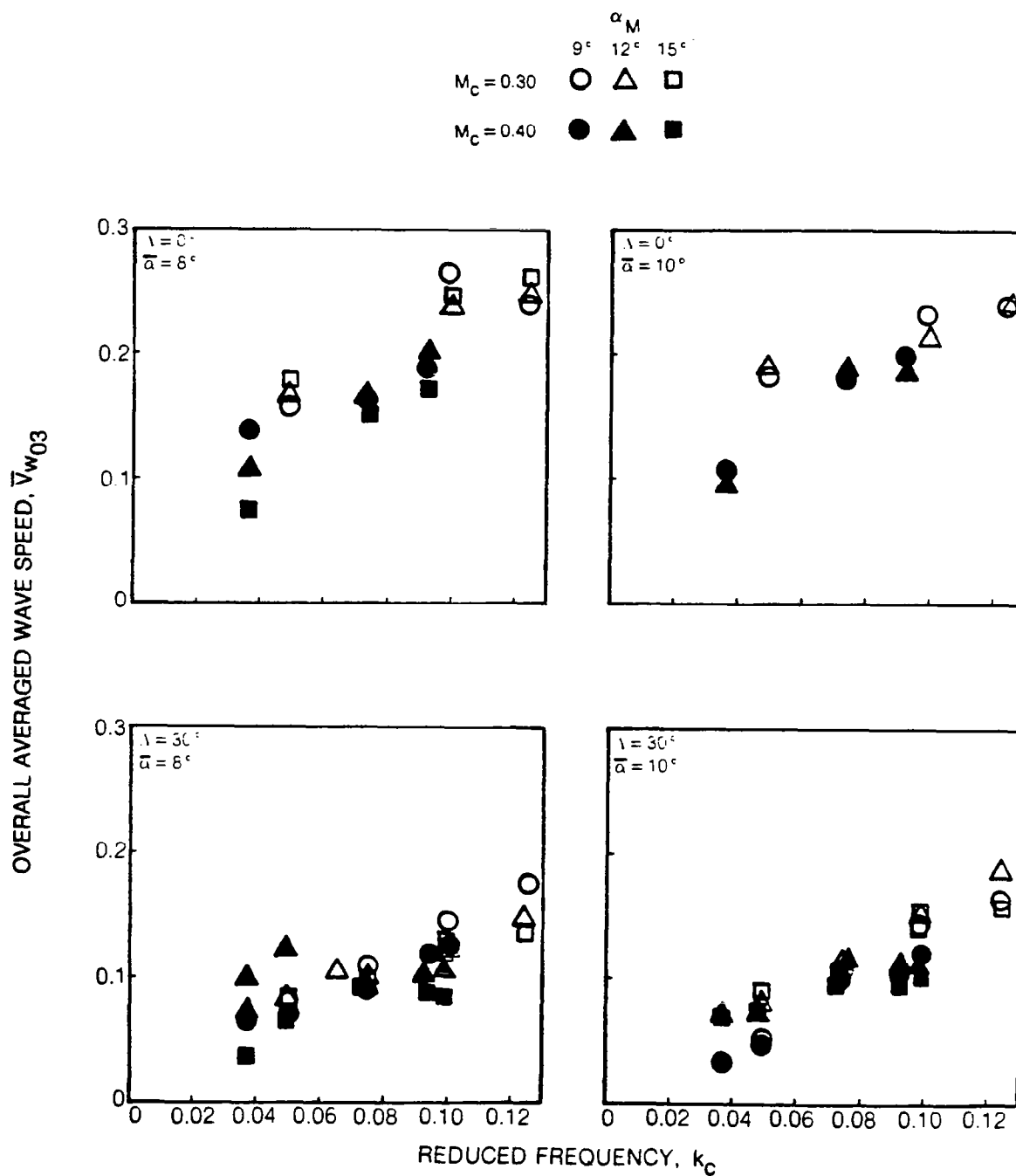


Fig. 17 Effect of Mach Number on Overall Wave Speed

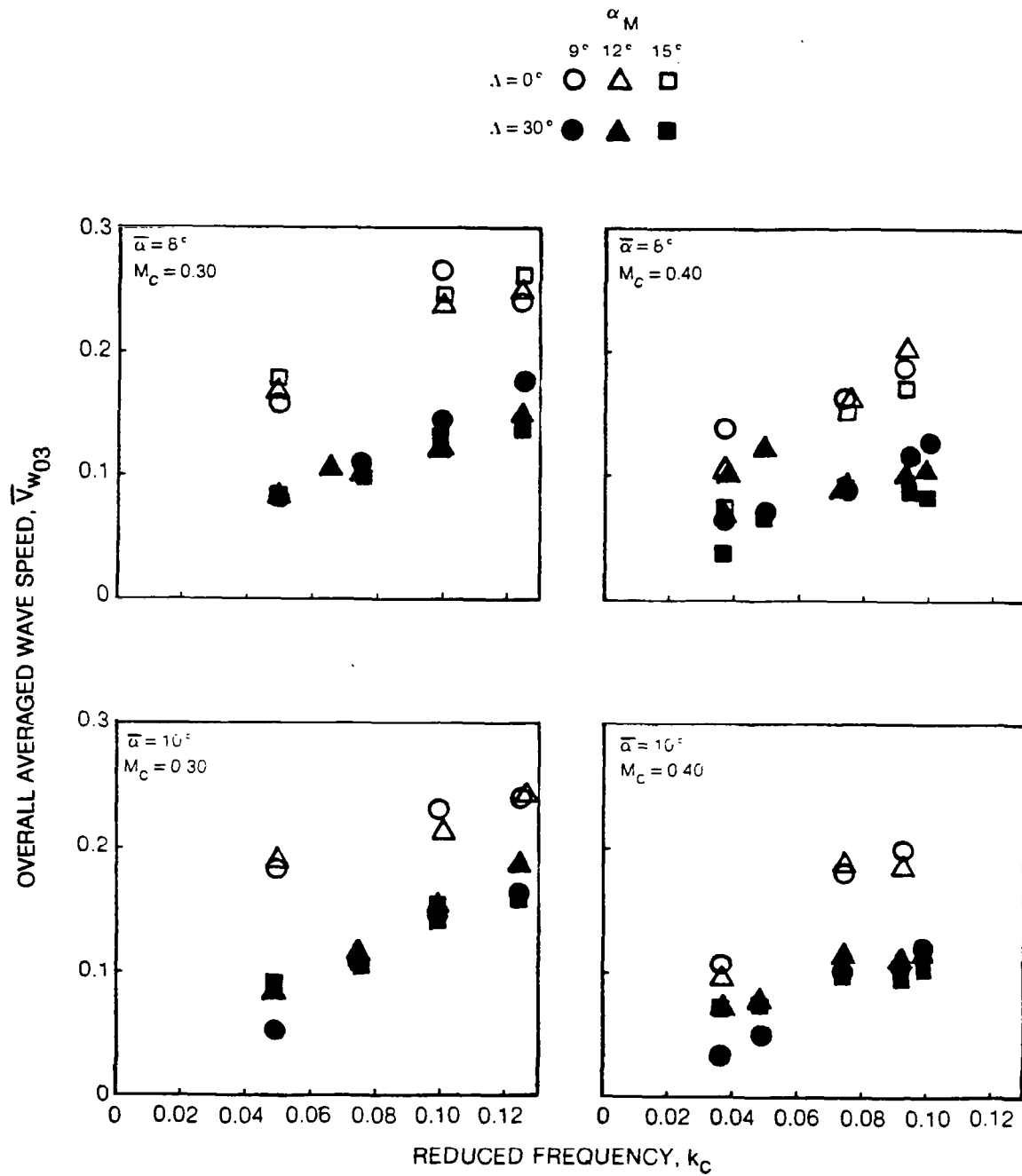


Fig. 18 Effect of Sweep Angle on Overall Wave Speed

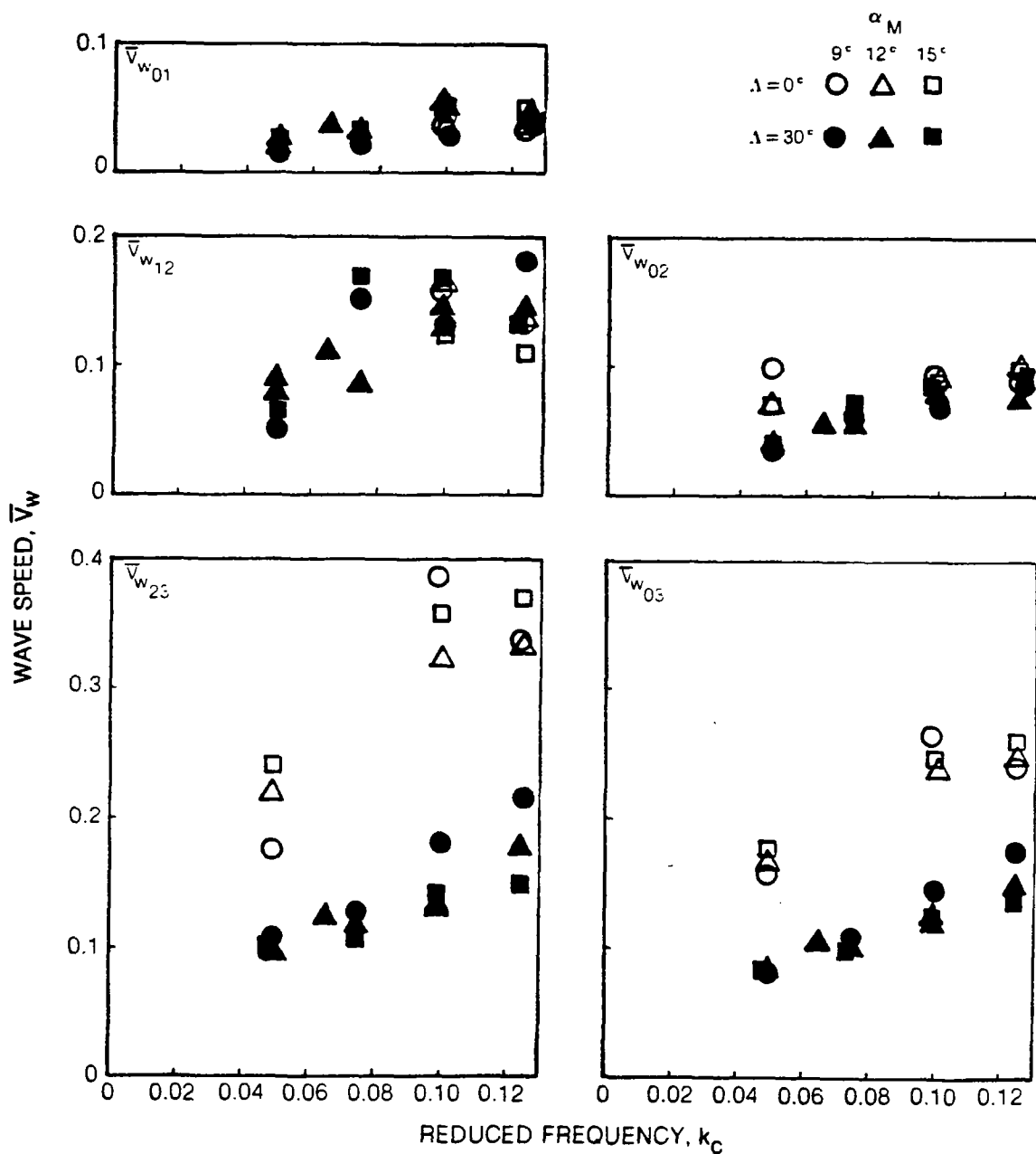


Fig. 19 Effect of Sweep Angle on Wave Speed at Several Chordwise Locations for $M_c = 0.30$ and $\bar{\alpha} = 8^\circ$

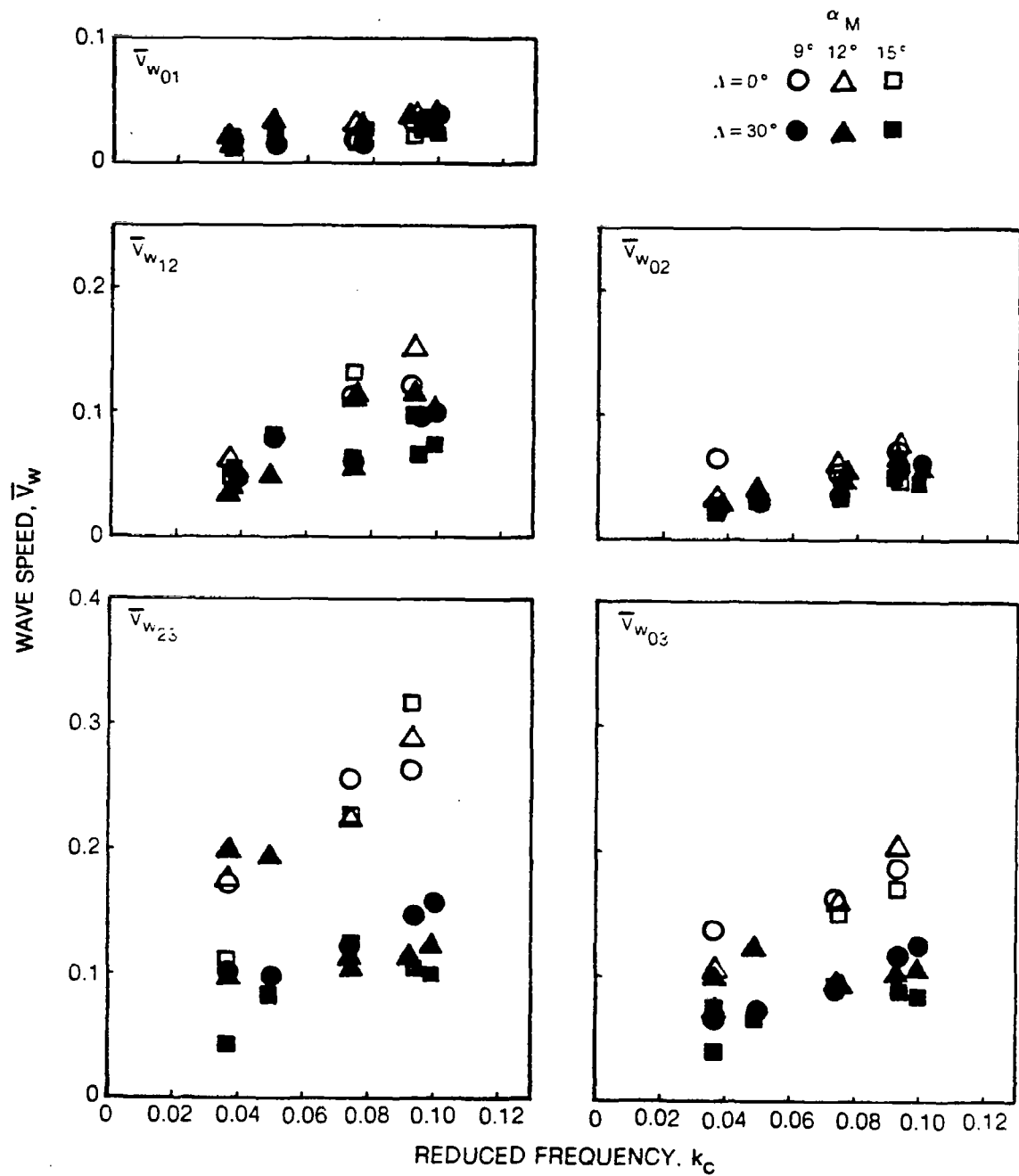


Fig. 20 Effect of Sweep Angle on Wave Speed at Several Chordwise Locations for $M_c = 0.40$ and $\bar{\alpha} = 8^\circ$

k_c	SYMBOL
0.038	○
0.050	△
0.075	□
0.094	▽
0.100	◇

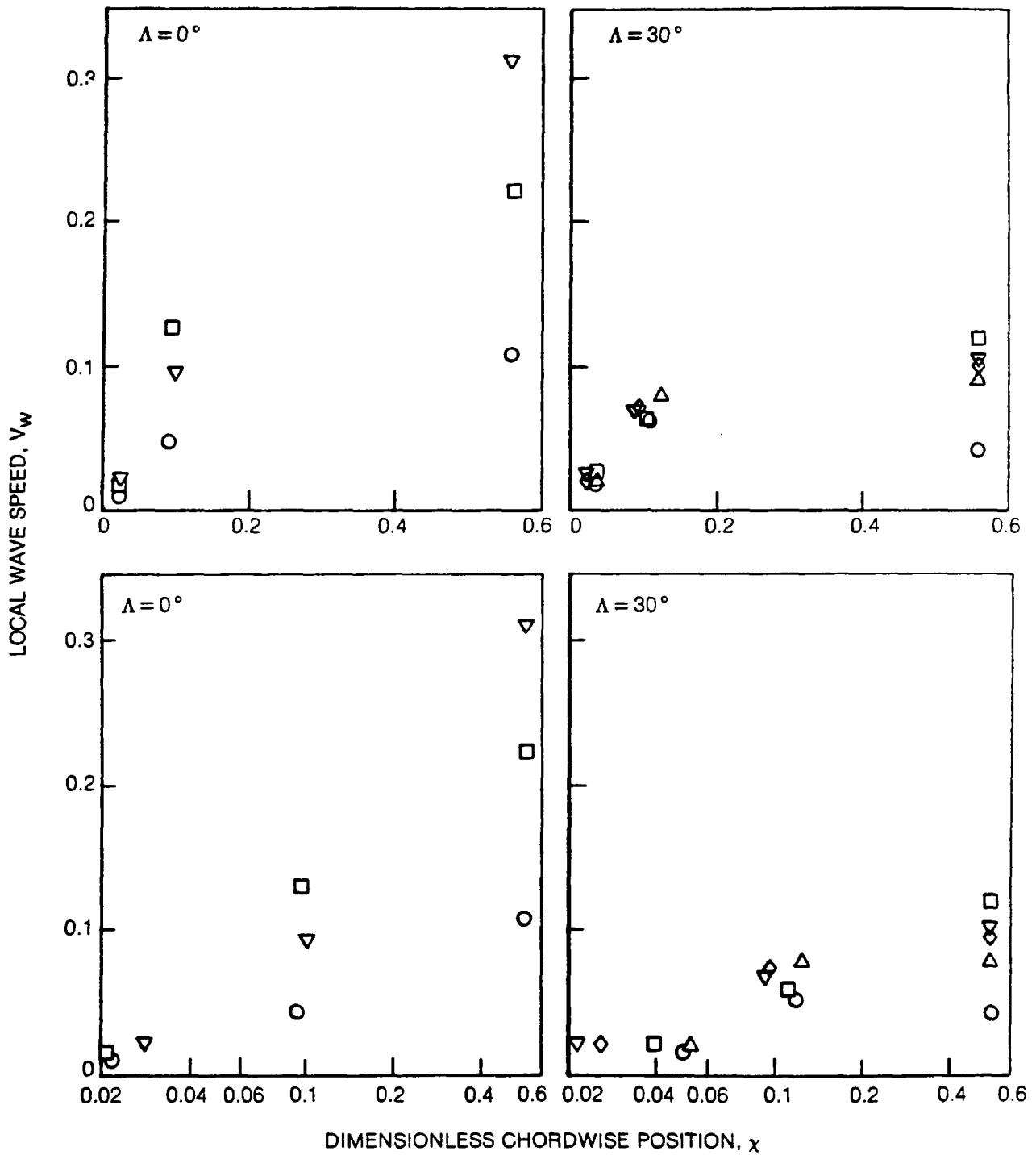


Fig. 21 Chordwise Variation of Local Wave Speed for $\alpha_M = 15$ deg, $M_c = 0.40$, and $\bar{\alpha} = 8$ deg

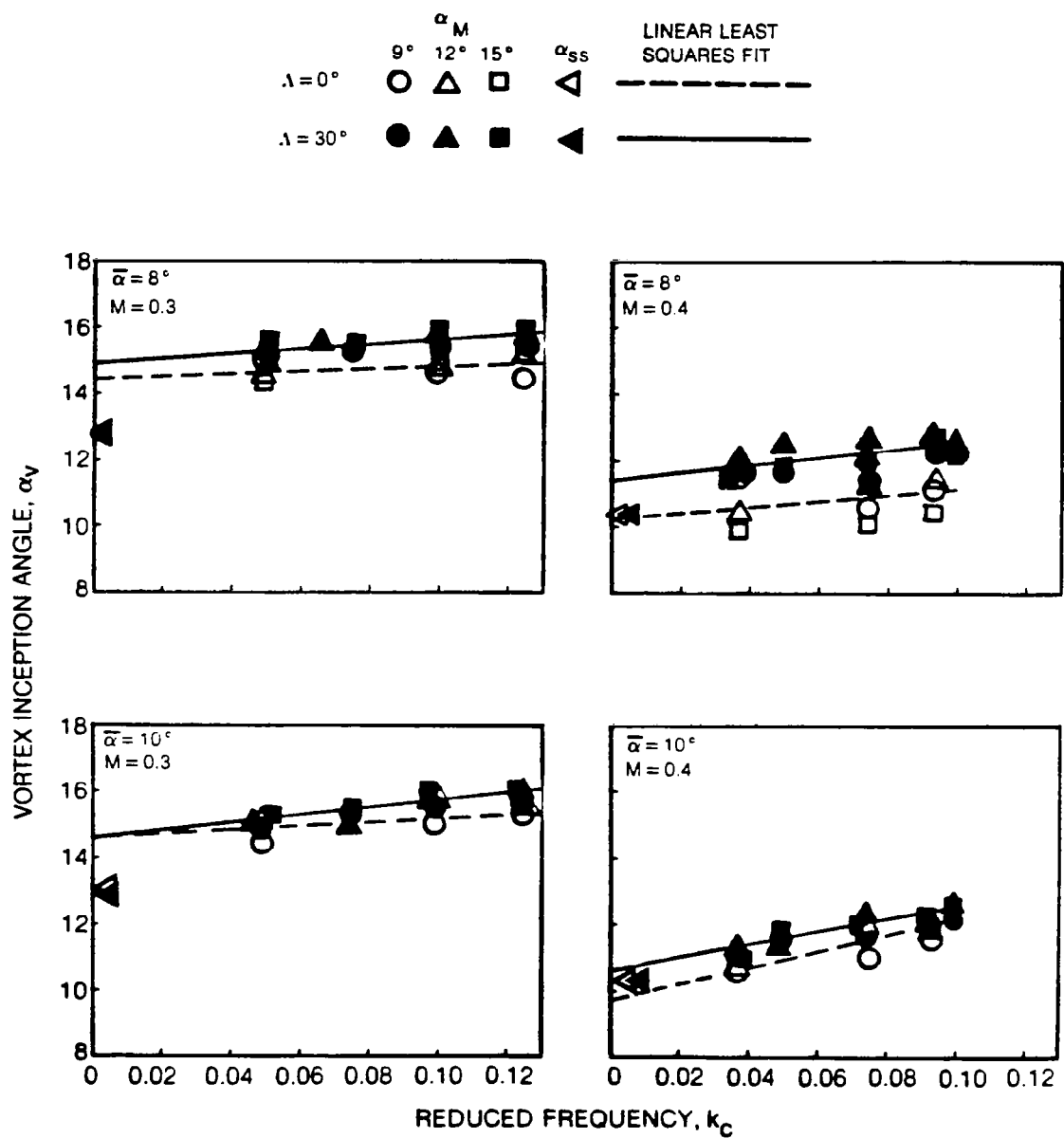


Fig. 22 Effect of Sweep Angle on Vortex Inception Angle Based on Initial Wave Propagation

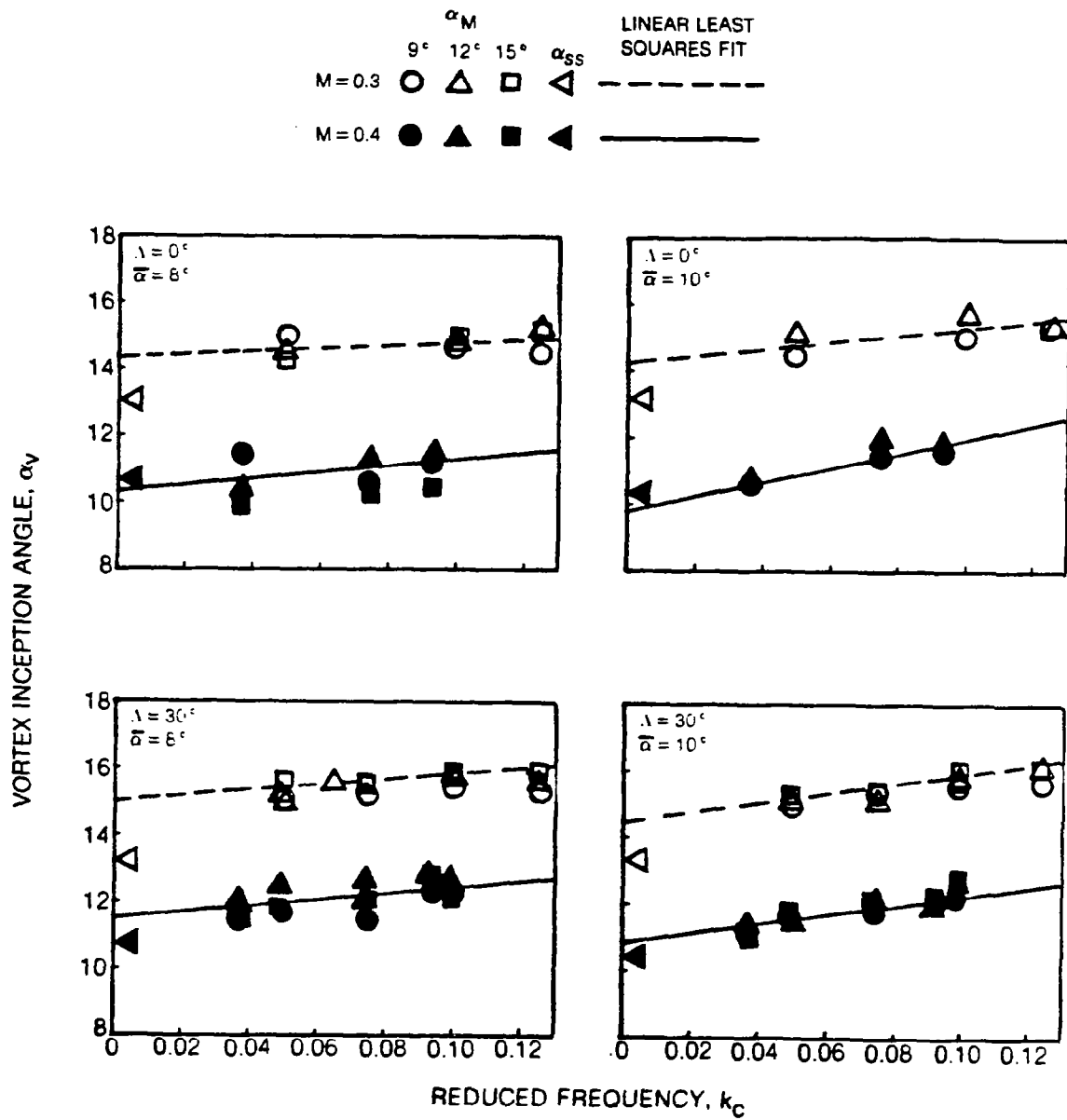


Fig. 23 Effect of Mach Number on Vortex Inception Angle Based on Initial Wave Propagation

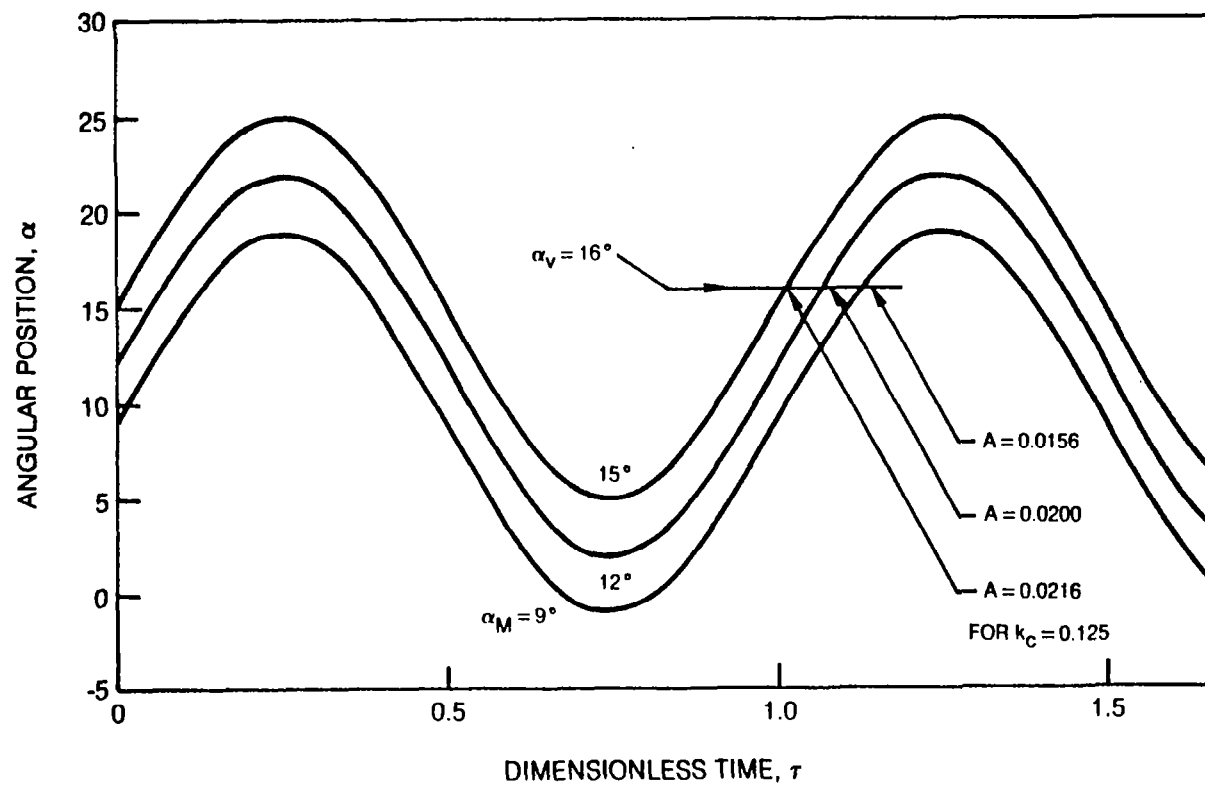


Fig. 24 Typical Motion Time Histories for Three Mean Angles of Attack

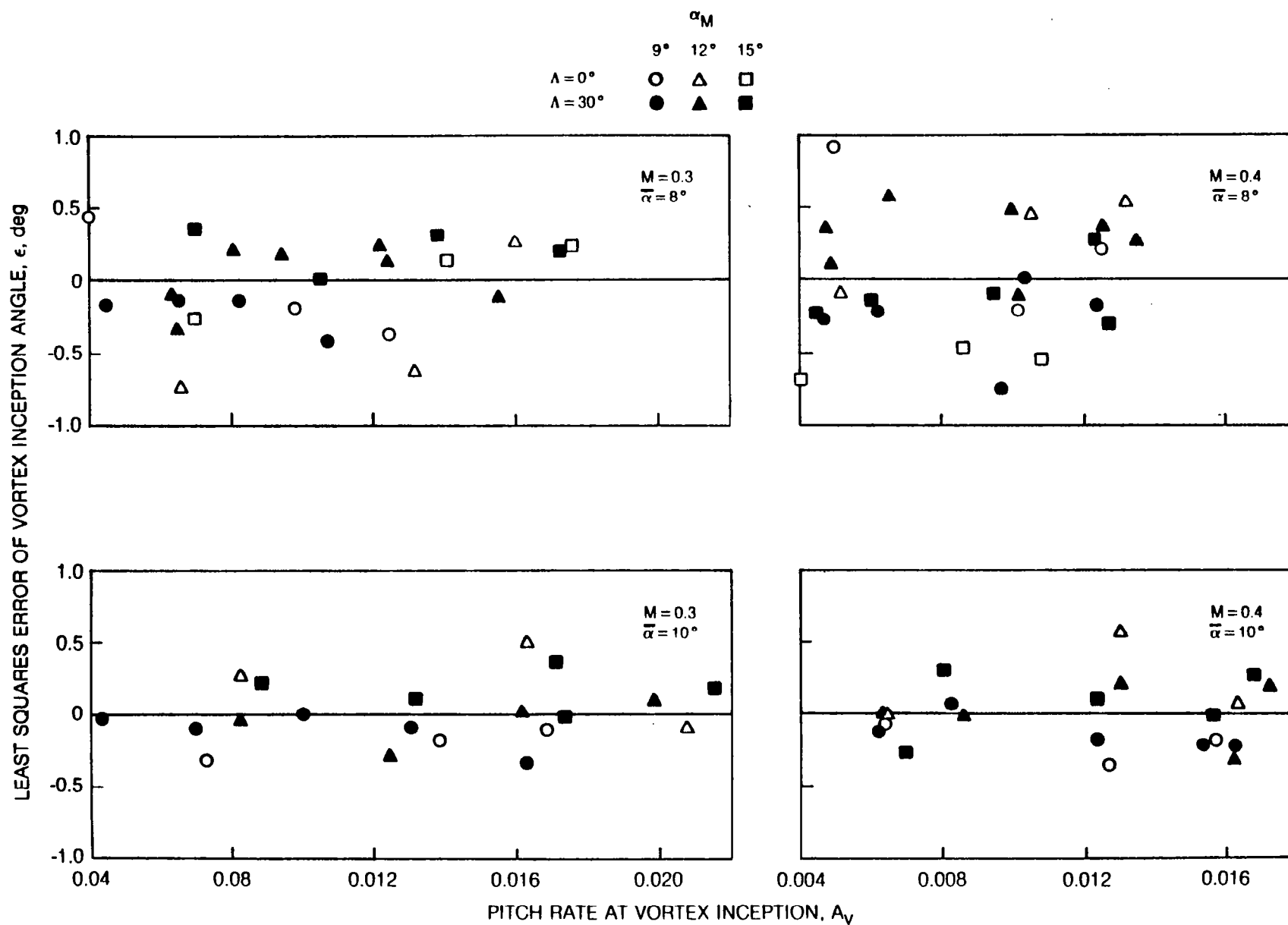


Fig. 25 Linear Least Squares Scatter Versus Pitch Rate

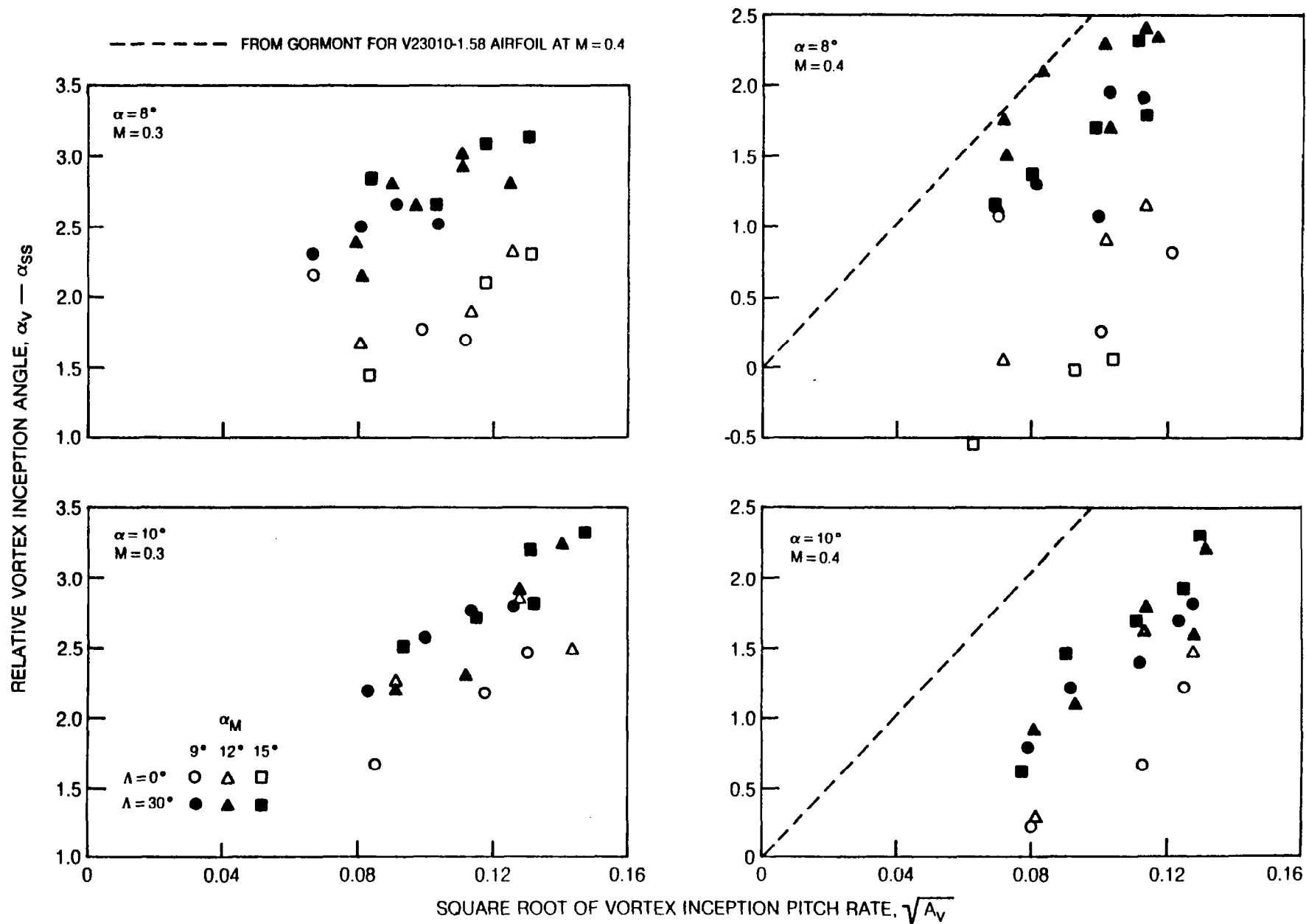


Fig. 26 Correlation of Relative Vortex Inception Angle with $\sqrt{A_v}$

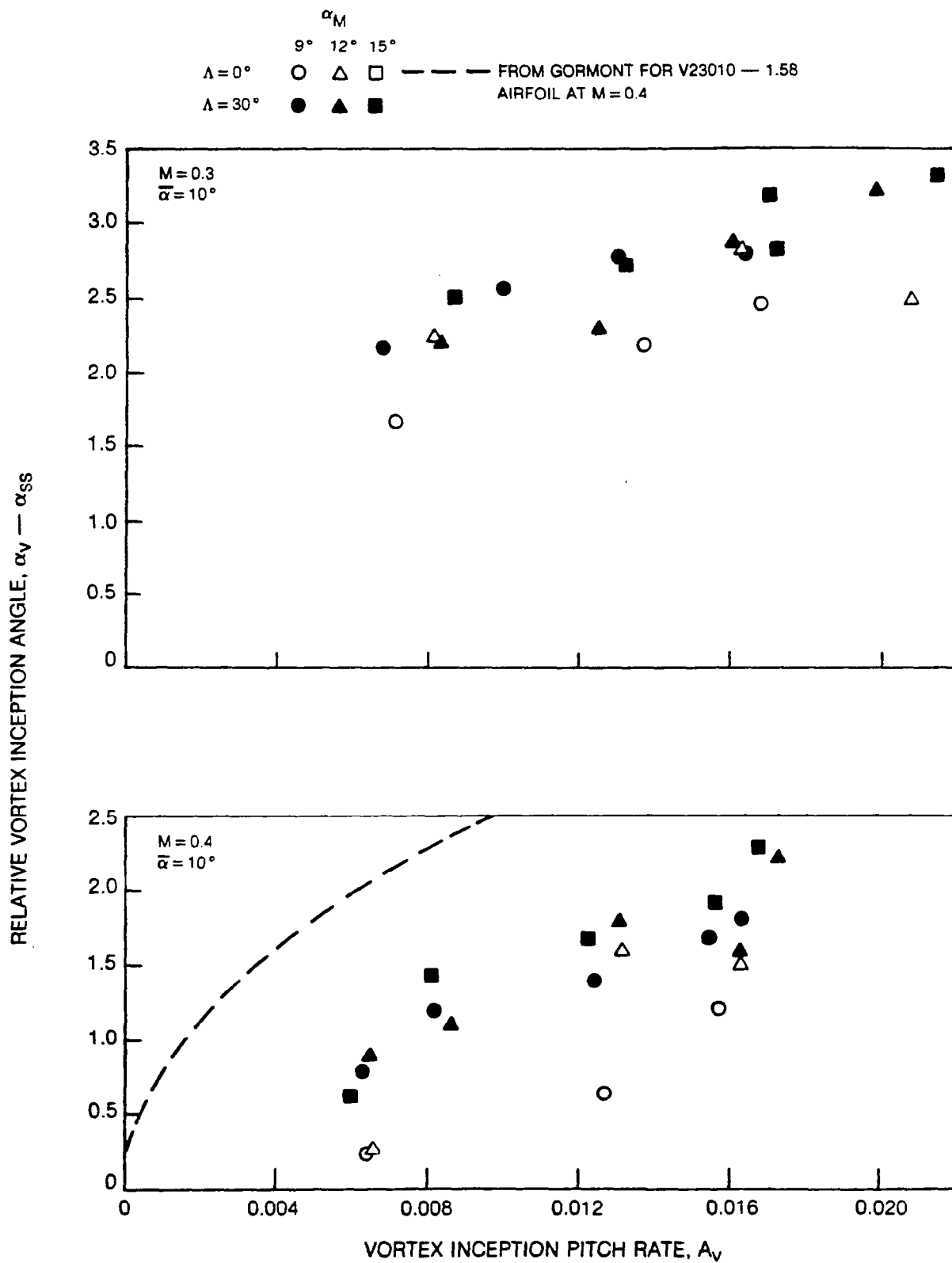


Fig. 27 Correlation of Relative Vortex Inception Angle with A_v

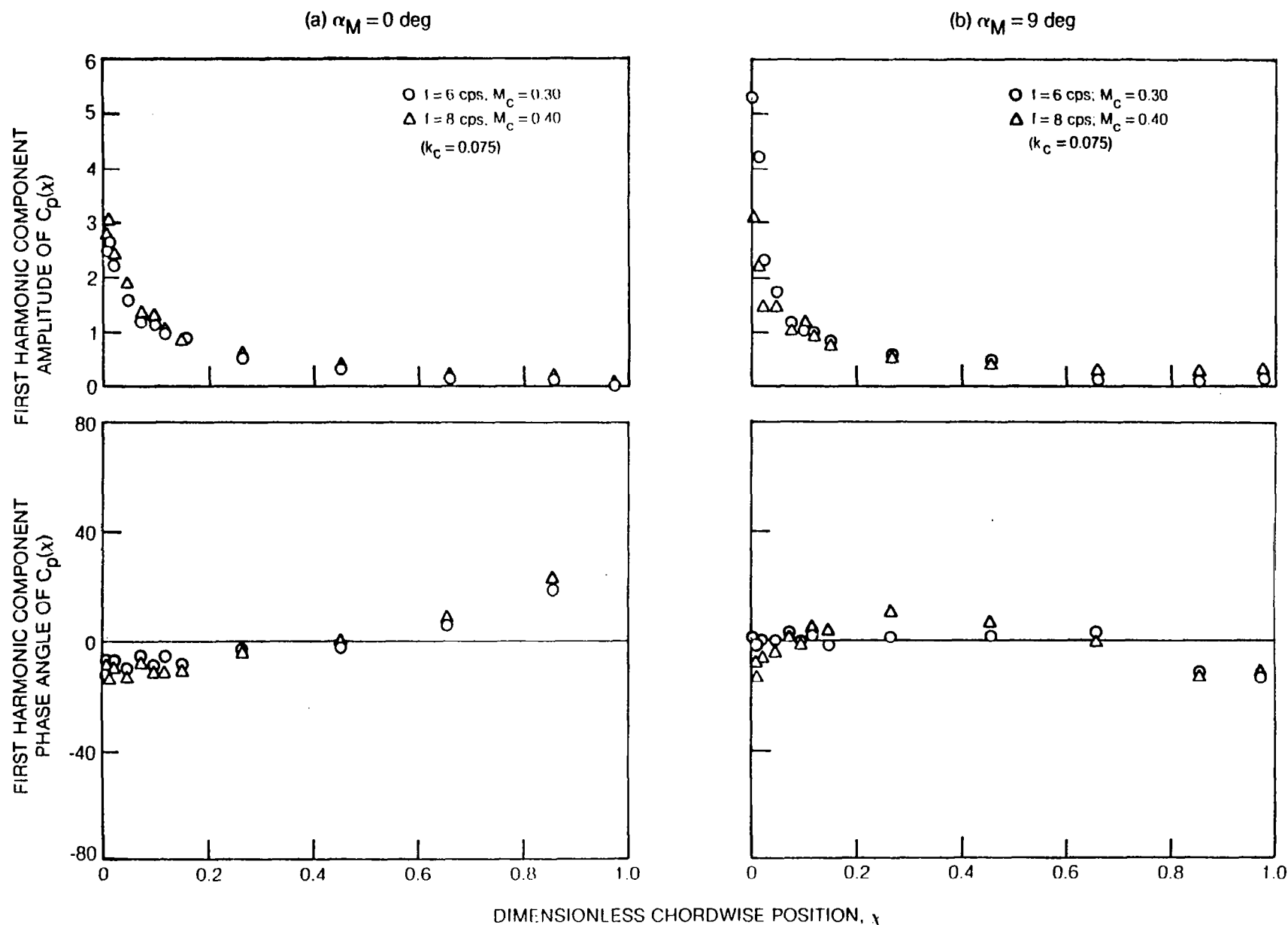


Fig. 28 Mach Number and Frequency Similarity Analysis of First Harmonic Component Response Distribution for 30 deg Swept Airfoil (Pitching Amplitude, $\bar{\alpha} = 8$ deg)

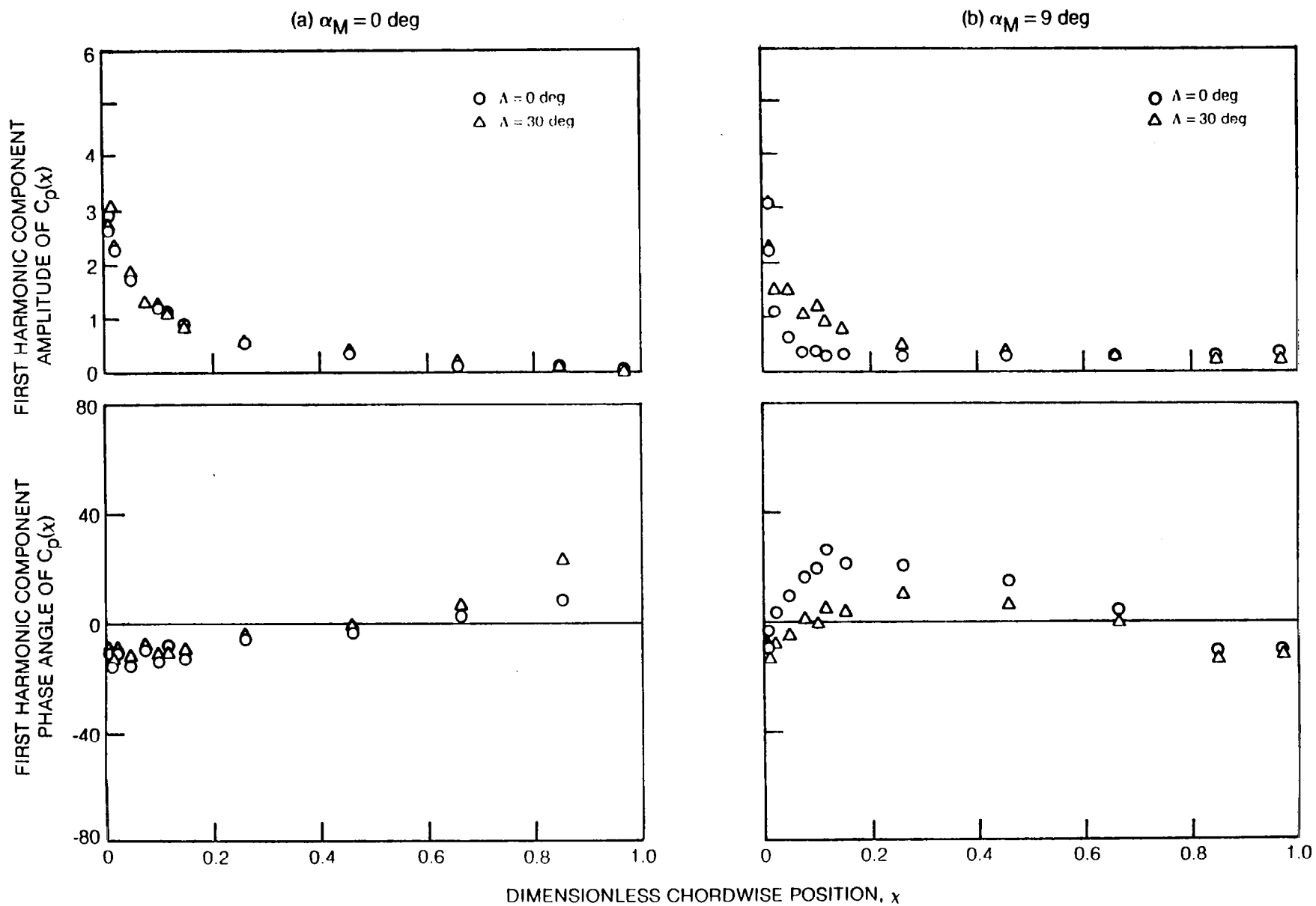


Fig. 29 Sweep Angle Similarity Analysis of First Harmonic Component Response Distribution
 $k_c = 0.075$ ($f = 8 \text{ Hz}$, $M_c = 0.40$) and $\bar{\alpha} = 8 \text{ deg}$

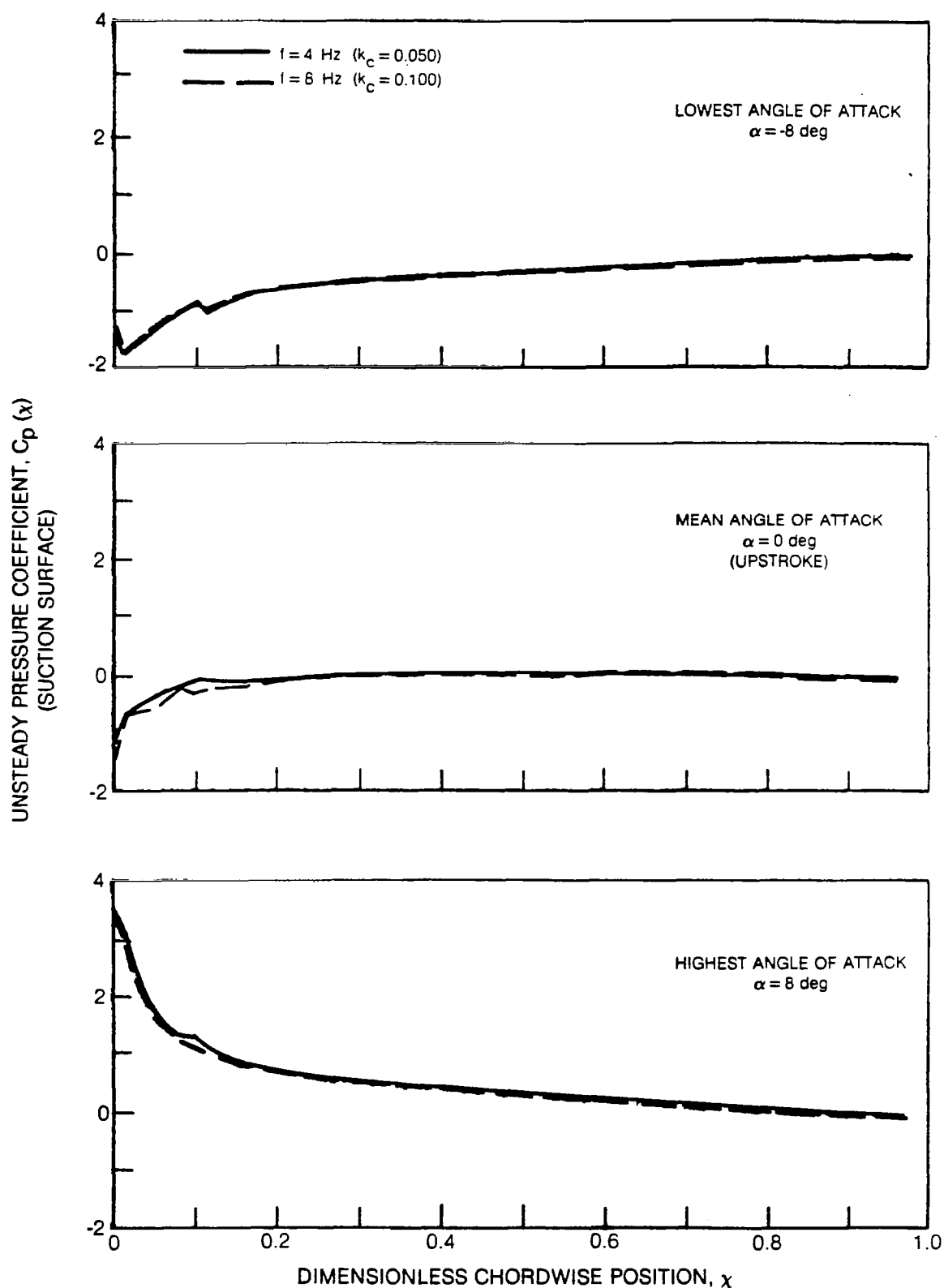


Fig. 30 Effect of Frequency on Complete Unsteady Chordwise Pressure Distribution at the Lowest, Mean, and Highest Angle of Attack Points of Motion Cycle ($\alpha_M = 0 \text{ deg}$, $M_C = 0.30$, $\bar{\alpha} = 8 \text{ deg}$, $\Lambda = 0 \text{ deg}$)

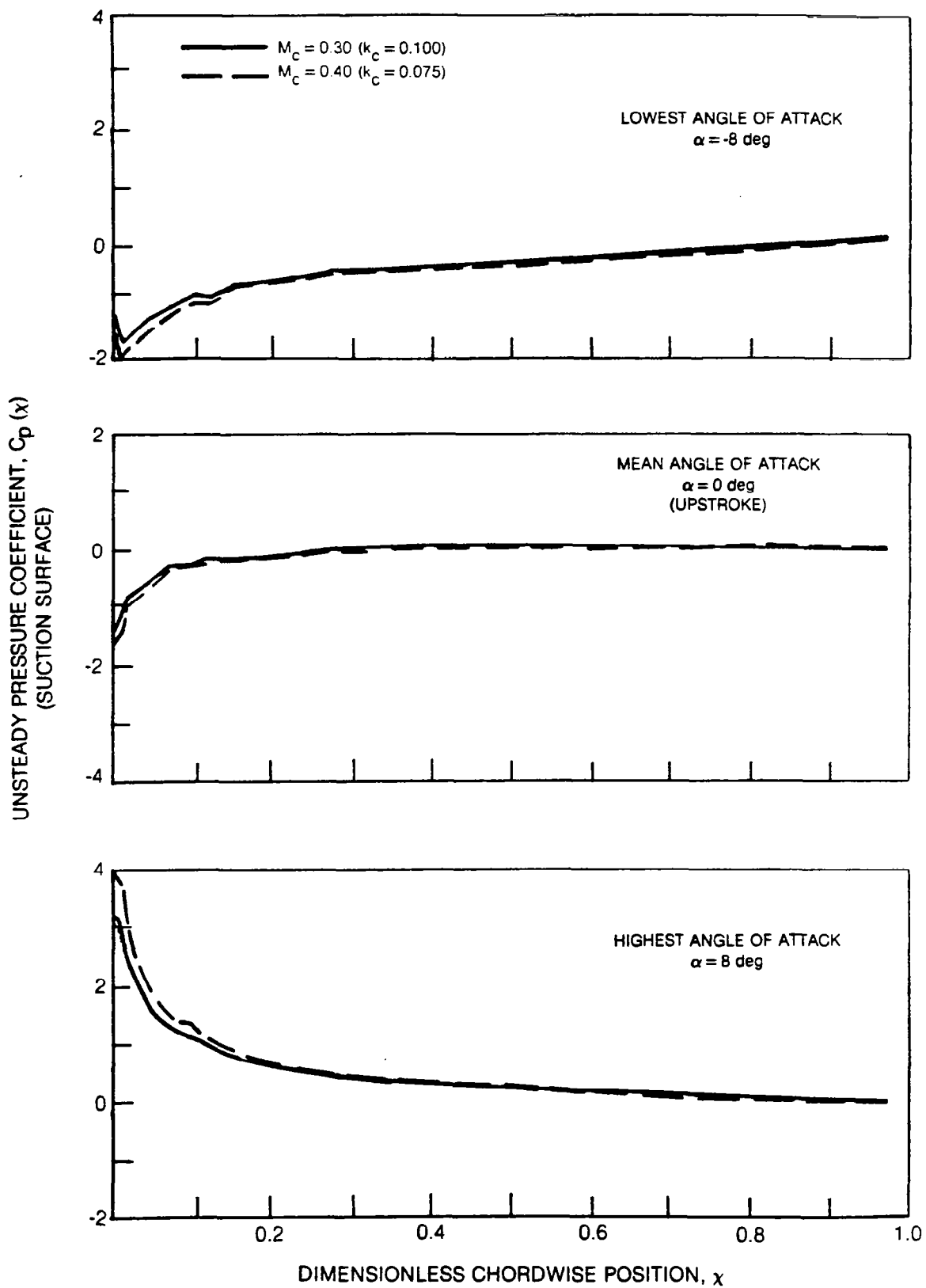


Fig. 31 Effect of Mach Number on Complete Unsteady Chordwise Pressure Distribution at the Lowest, Mean and Highest Angle of Attack Points of Motion Cycle ($\alpha_M = 0$ deg, $f = 8$ Hz, $\bar{\alpha} = 8$ deg, $\Lambda = 0$ deg)

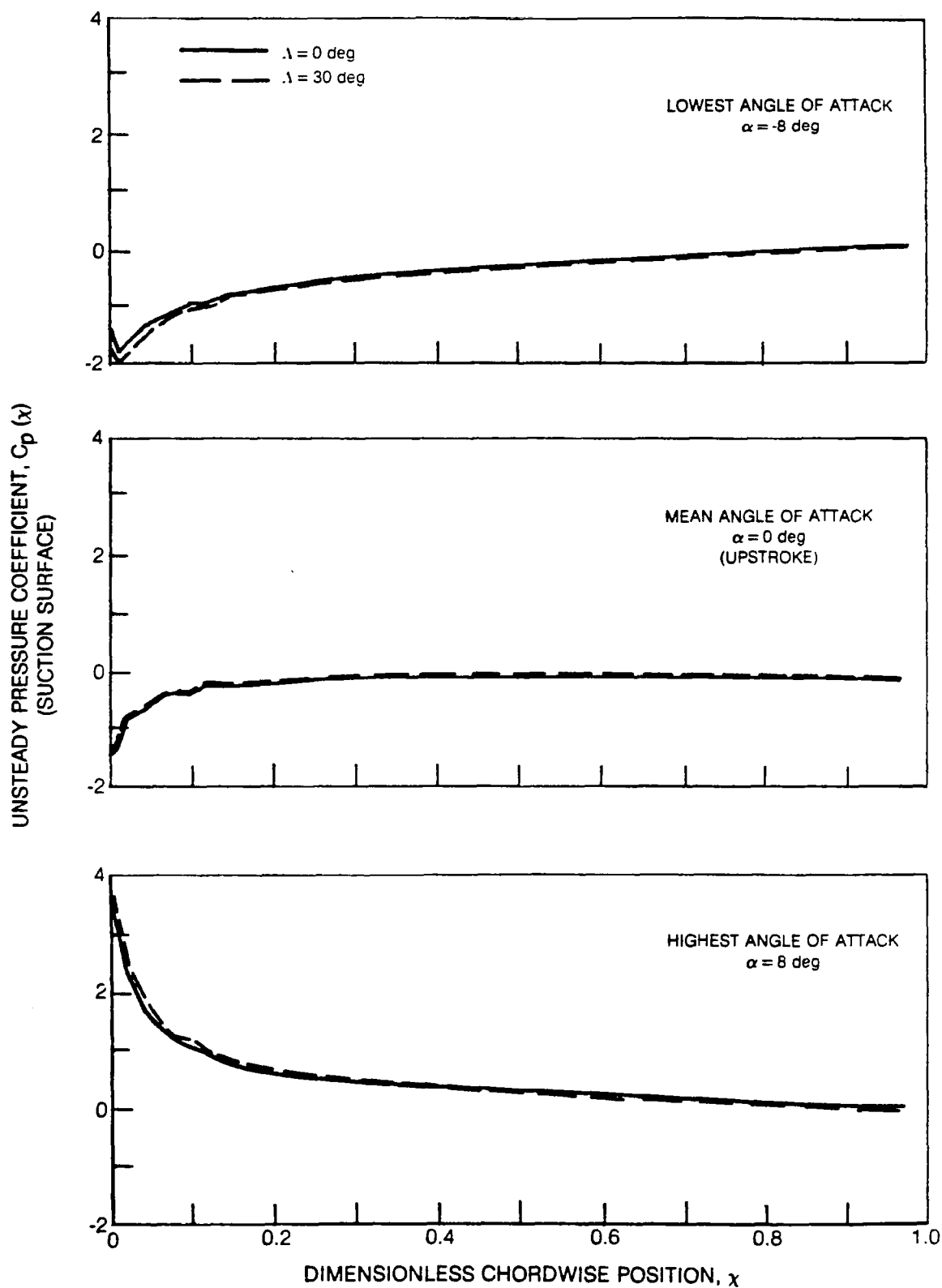


Fig. 32 Effect of Sweep on Complete Unsteady Chordwise Pressure Distribution at the Lowest, Mean, and Highest Angle of Attack Points of Motion Cycle
 $\alpha_M = 0 \text{ deg}$, $k_c = 0.100$ ($f = 8 \text{ Hz}$, $M_c = 0.30$), and $\bar{\alpha} = 8 \text{ deg}$

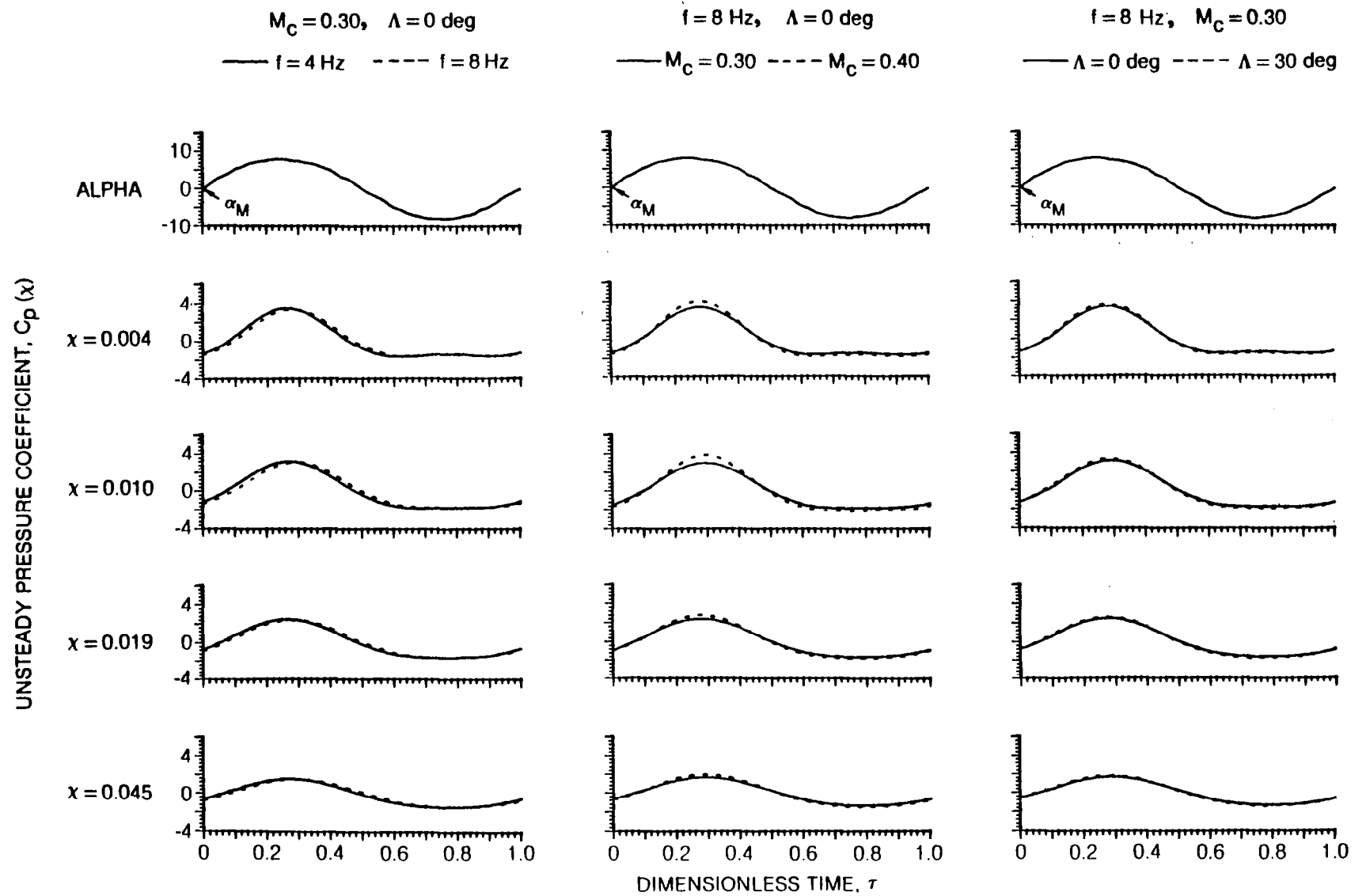


Fig. 33 Parameter Sensitivity of Upper Surface, Leading Edge Region Pressure Coefficient Time Histories at $\alpha_M = 0 \text{ deg}$ and $\bar{\alpha} = 8 \text{ deg}$

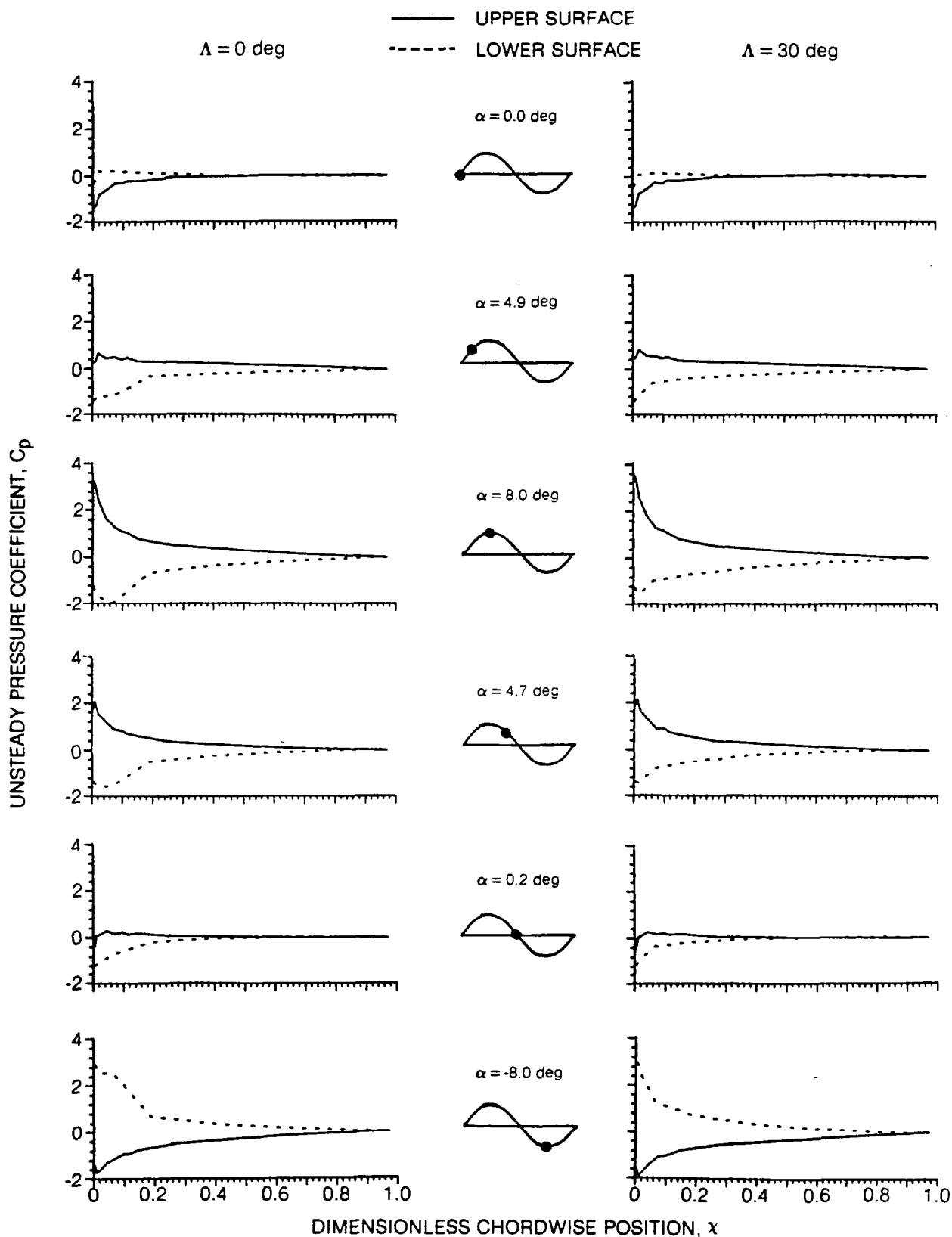


Fig. 34 Chordwise Pressure Results for the Unswept and Swept Configurations at $\alpha_M = 0 \text{ deg}$, $k_c = 0.100$ ($f = 8 \text{ Hz}$, $M_c = 0.30$), and $\bar{\alpha} = 8 \text{ deg}$

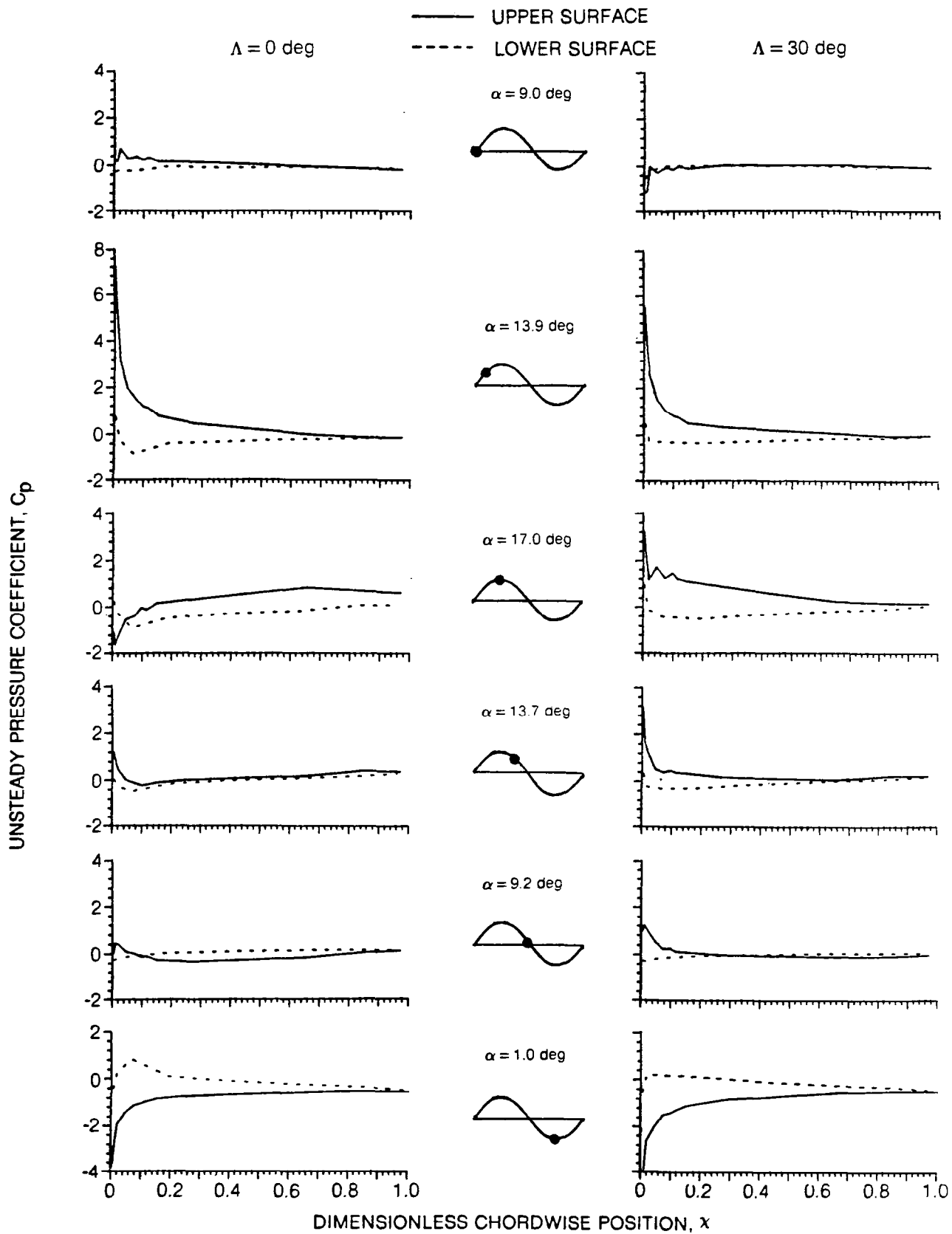


Fig. 35 Chordwise Pressure Results for the Unswept and Swept Configurations at $\alpha_M = 9 \text{ deg}$, $k_c = 0.100$ ($f = 8 \text{ Hz}$, $M_c = 0.30$), and $\bar{\alpha} = 8 \text{ deg}$

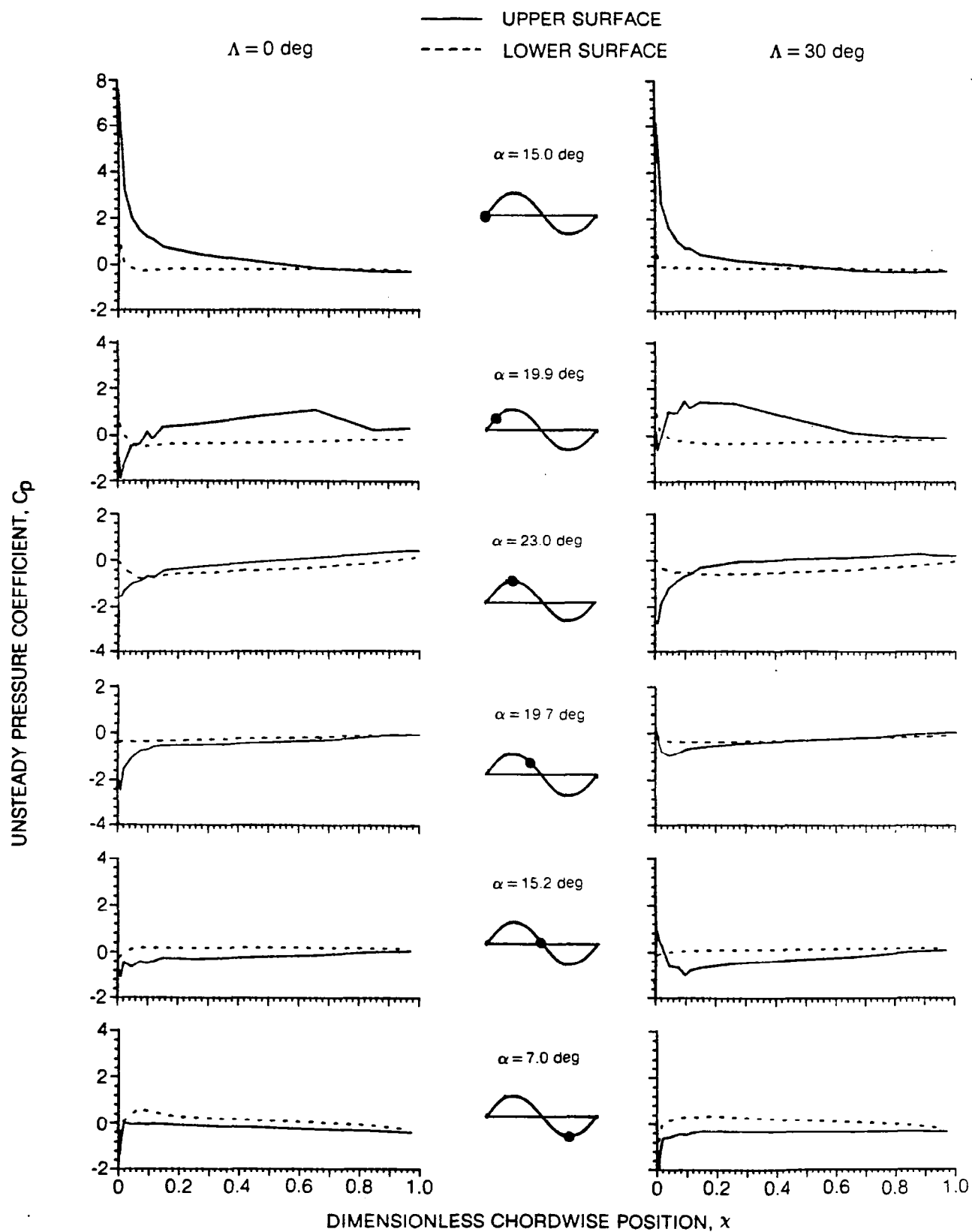


Fig. 36 Chordwise Pressure Results for the Unswept and Swept Configurations at $\alpha_M = 15 \text{ deg}$, $k_c = 0.100$ ($f = 8 \text{ Hz}$, $M_c = 0.30$), and $\bar{\alpha} = 8 \text{ deg}$

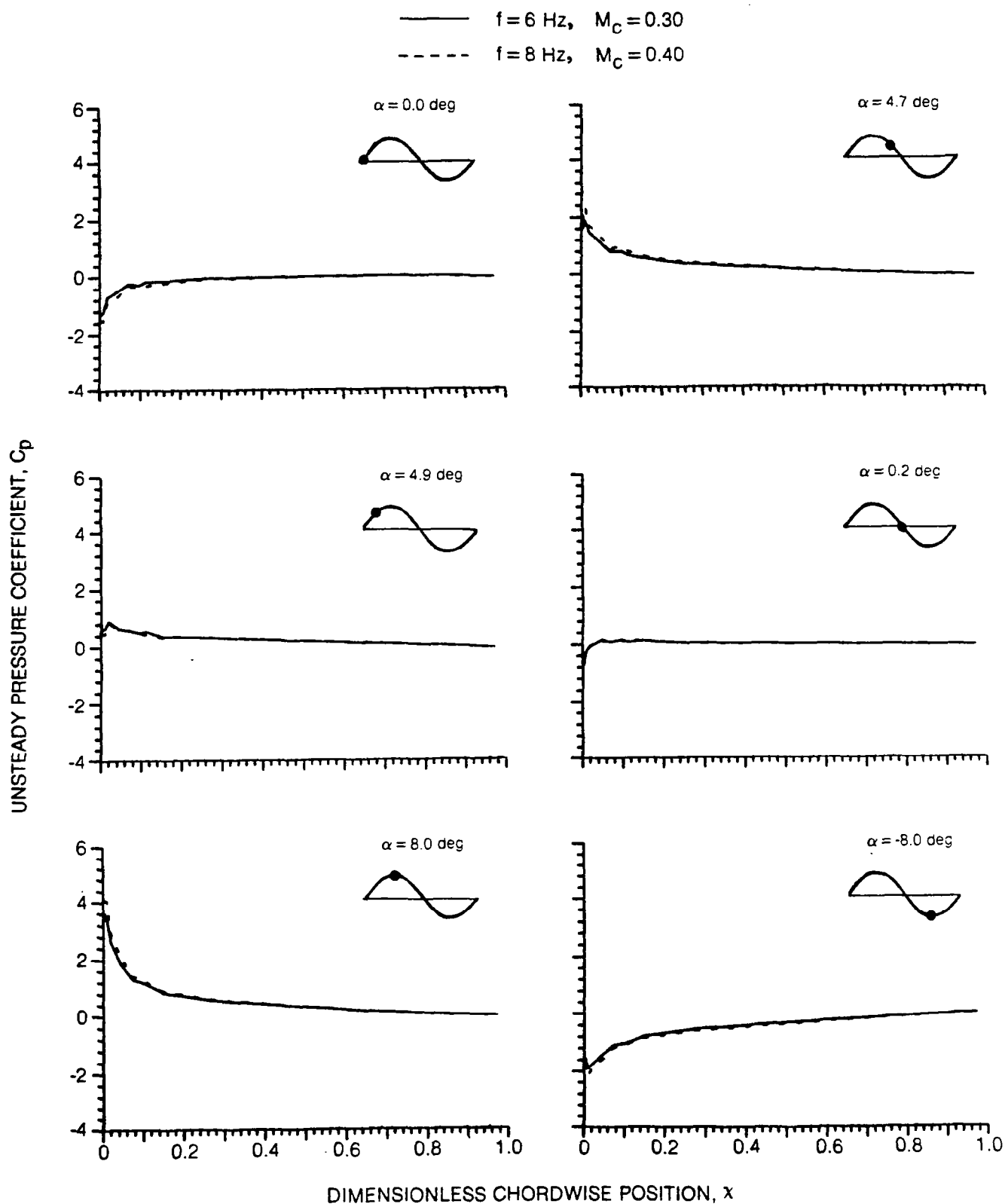


Fig. 37 Upper Surface Chordwise Pressure Behavior of Swept Airfoil at $\alpha_M = 0 \text{ deg}$, $k_C = 0.075$, and $\bar{\alpha} = 8 \text{ deg}$

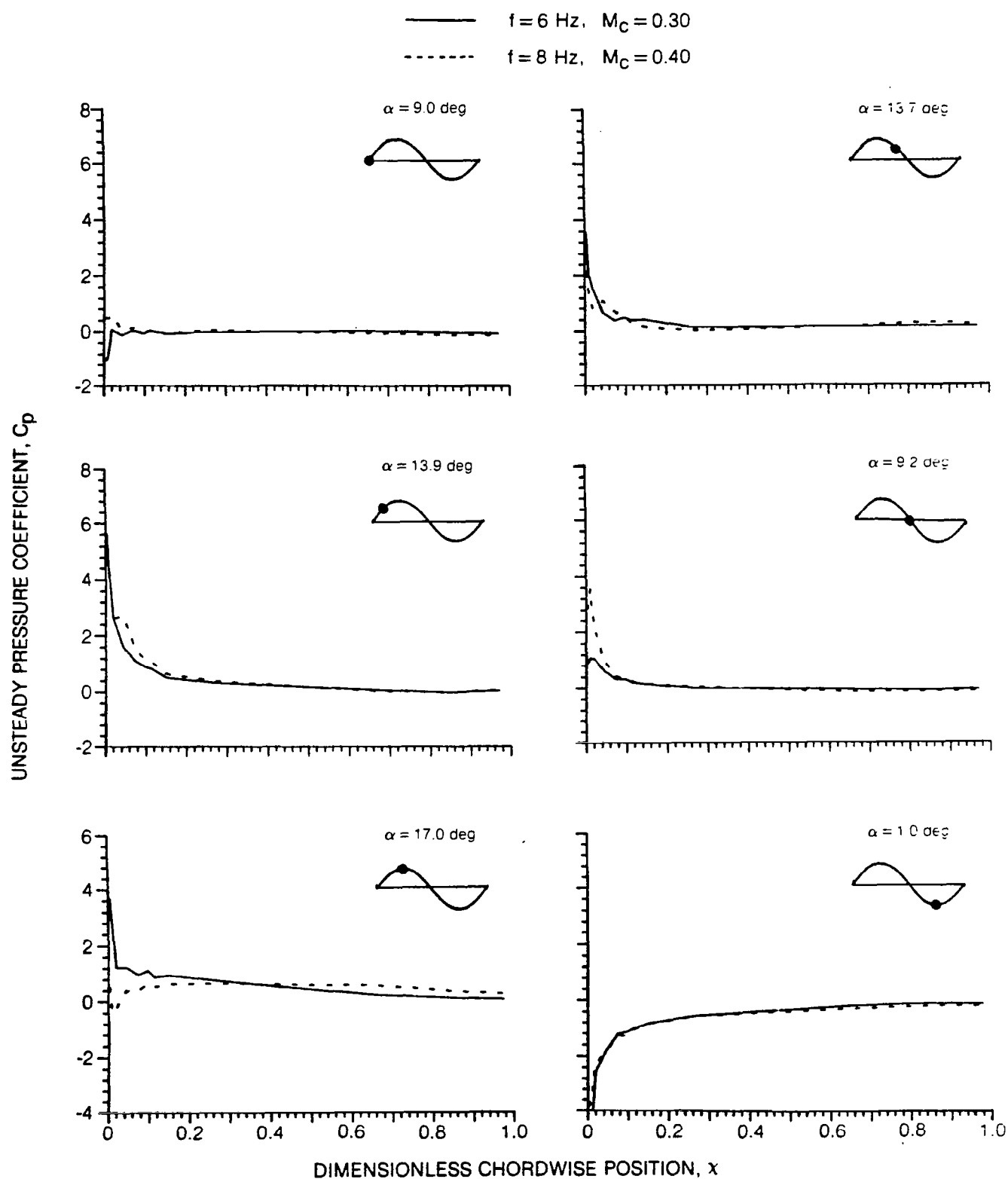


Fig. 38 Upper Surface Chordwise Pressure Behavior of Swept Airfoil at $\alpha_M = 9^\circ$, $k_C = 0.075$, and $\bar{\alpha} = 8^\circ$

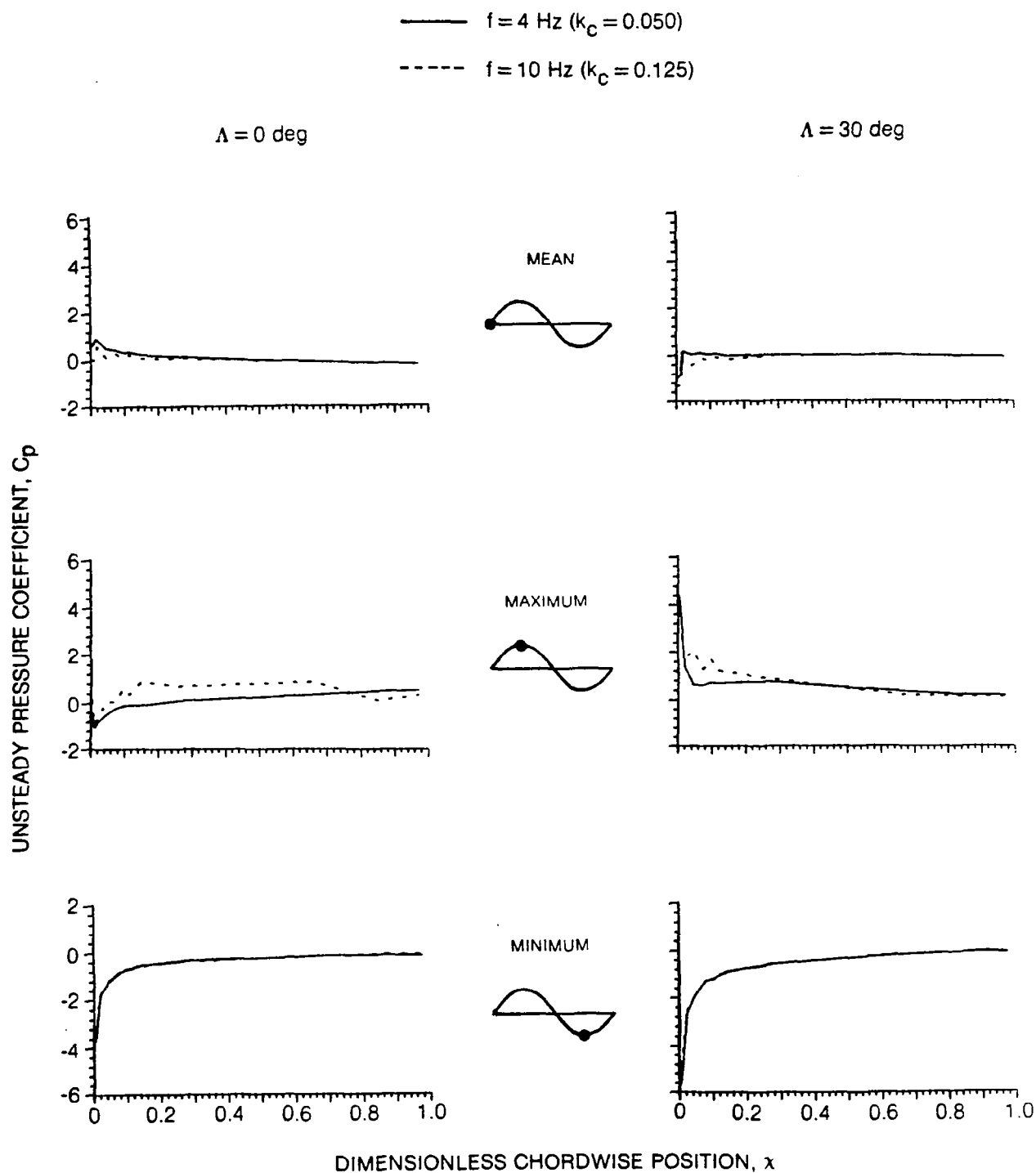


Fig. 39 Effect of Frequency on Upper Surface Response at Mean, Maximum, and Minimum Points of Motion Cycle ($\alpha_M = 9 \text{ deg}$, $M_c = 0.30$, $\bar{\alpha} = 8 \text{ deg}$)

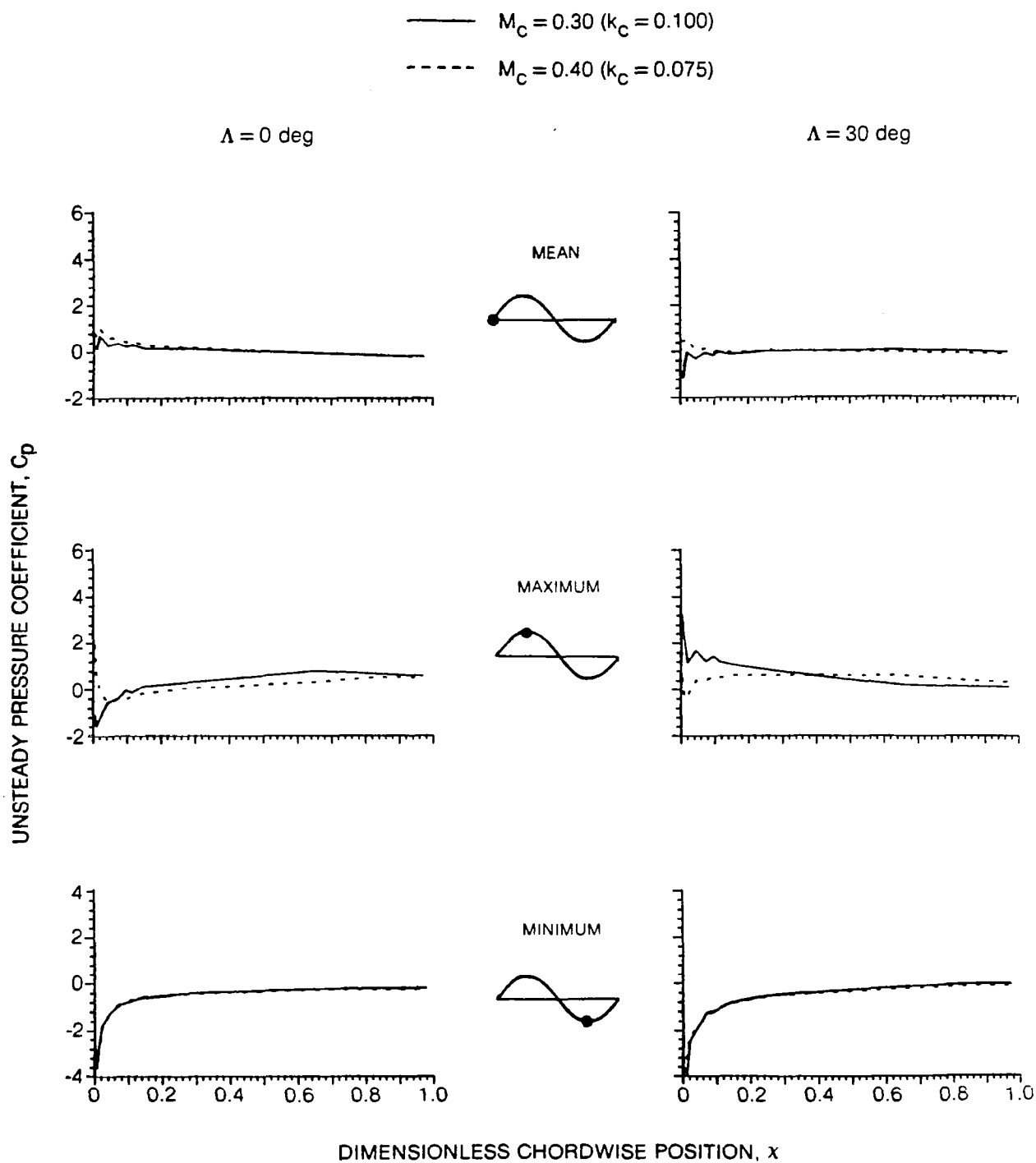


Fig. 40 Effect of Mach Number on Upper Surface Response at Mean, Maximum, and Minimum Points of Motion Cycle ($\alpha_M = 9 \text{ deg}$, $f = 8 \text{ Hz}$, $\bar{\alpha} = 8 \text{ deg}$)

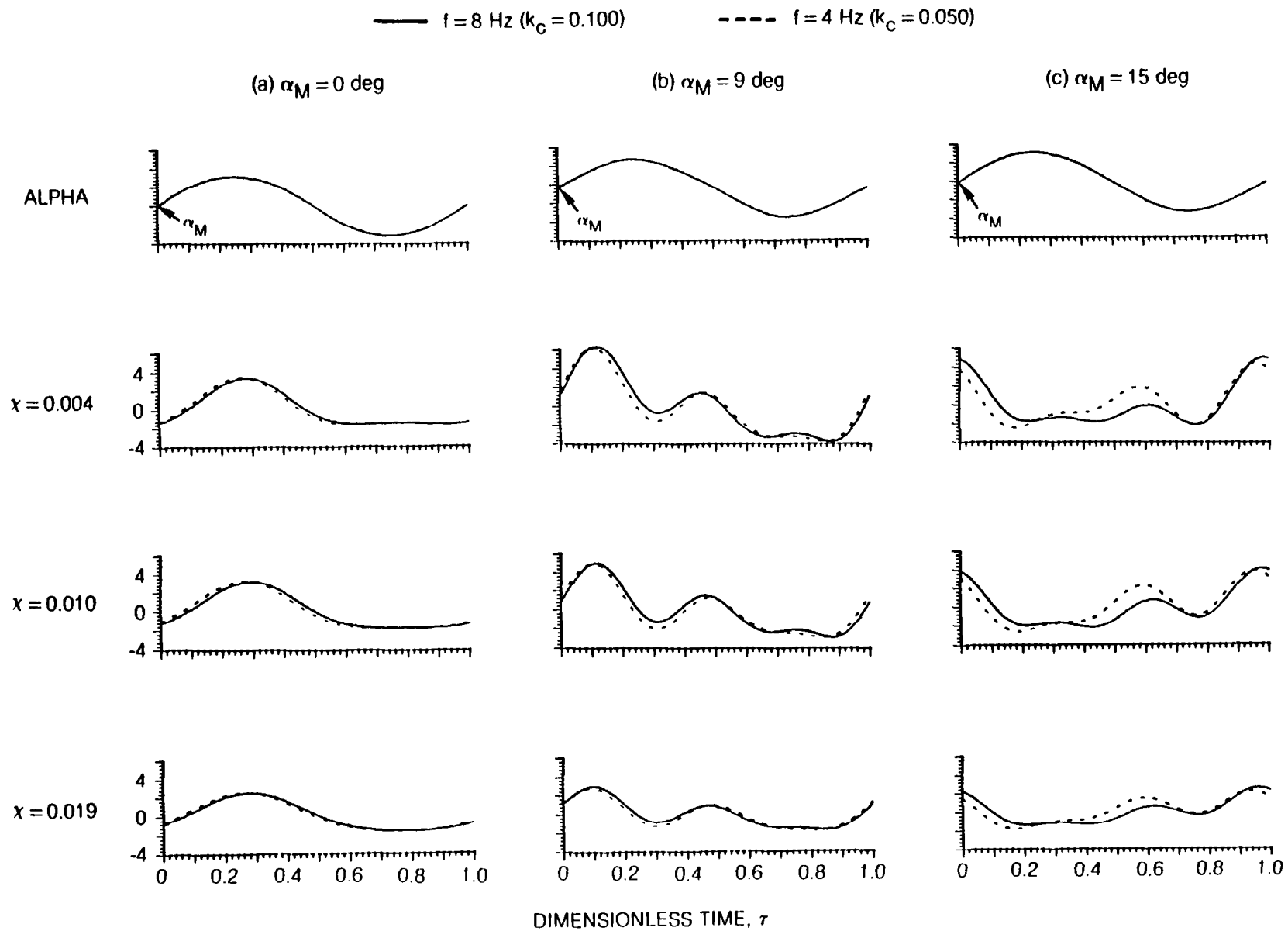


Fig. 41 Effect of Frequency on Upper Surface Leading Edge Region Time Histories ($M_c = 0.30$, $\bar{\alpha} = 8 \text{ deg}$, $\Lambda = 0 \text{ deg}$)

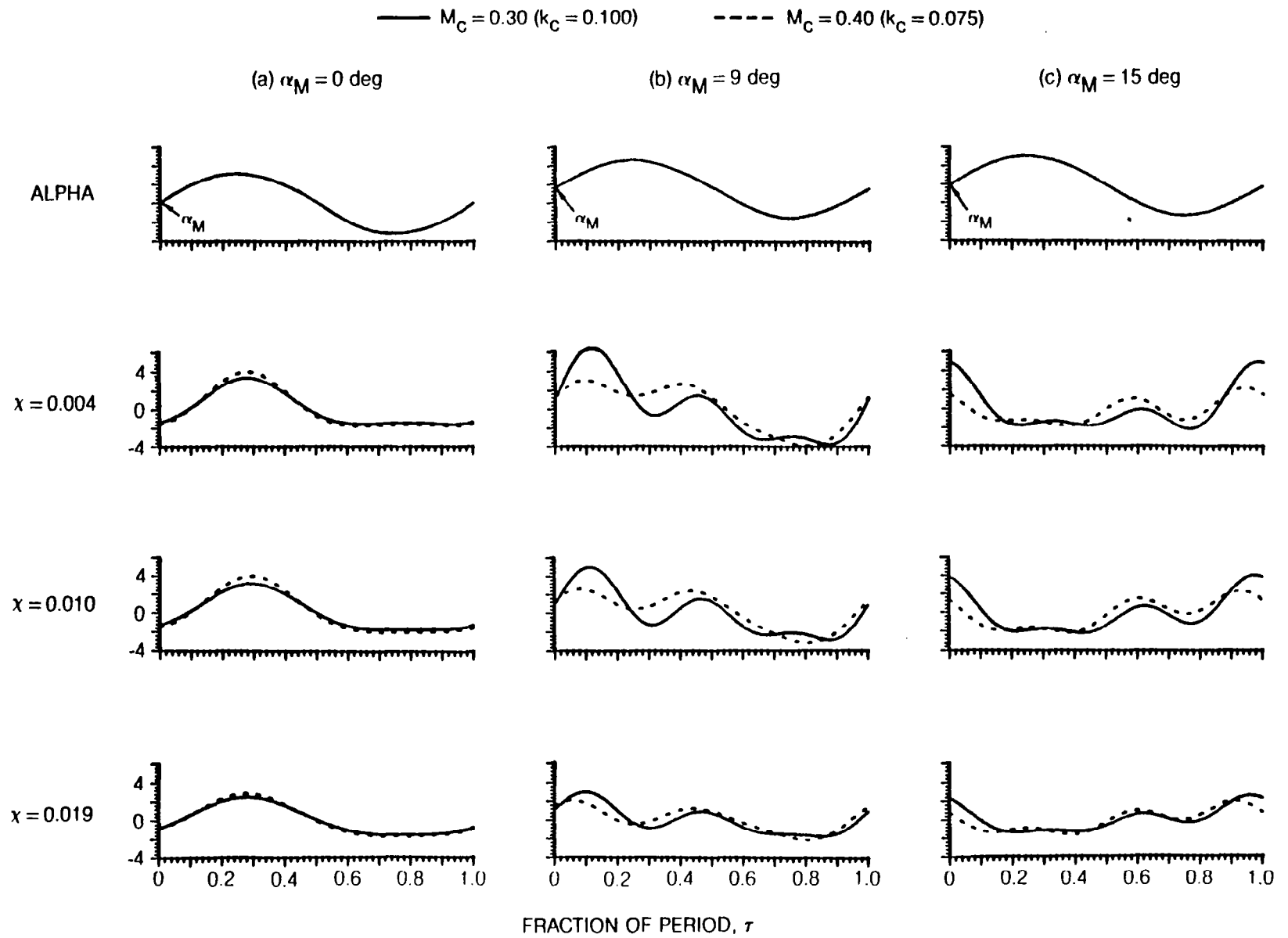


Fig. 42 Effect of Mach Number on Upper Surface Leading Edge Region Time Histories ($f = 8$ Hz, $\bar{\alpha} = 8$ deg, $\Lambda = 0$ deg)

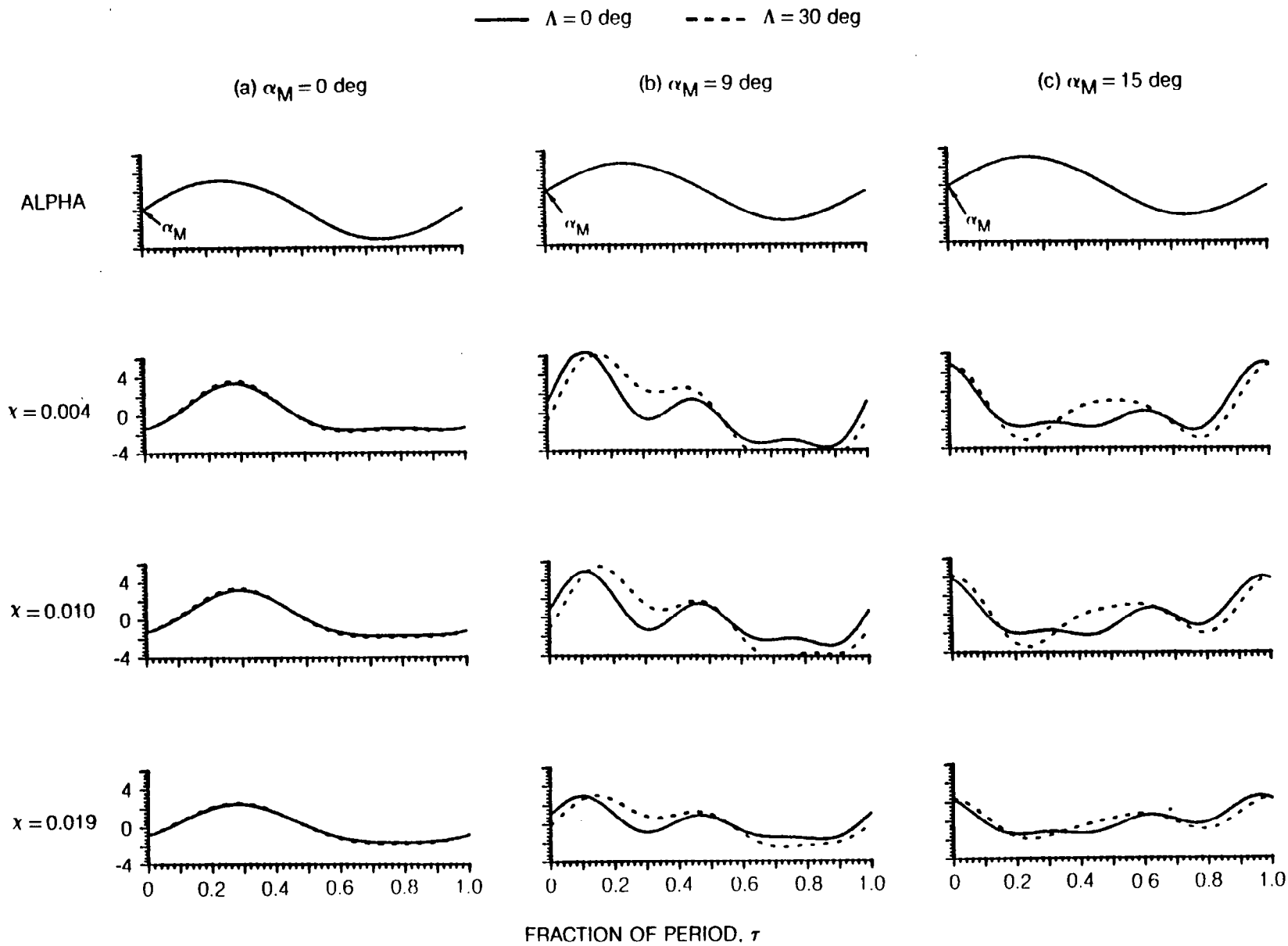


Fig. 43 Effect of Sweep on Upper Surface Leading Edge Region Time Histories
 $k_c = 0.100$ ($f = 8$ Hz, $M_c = 0.30$) and $\bar{\alpha} = 8$ deg

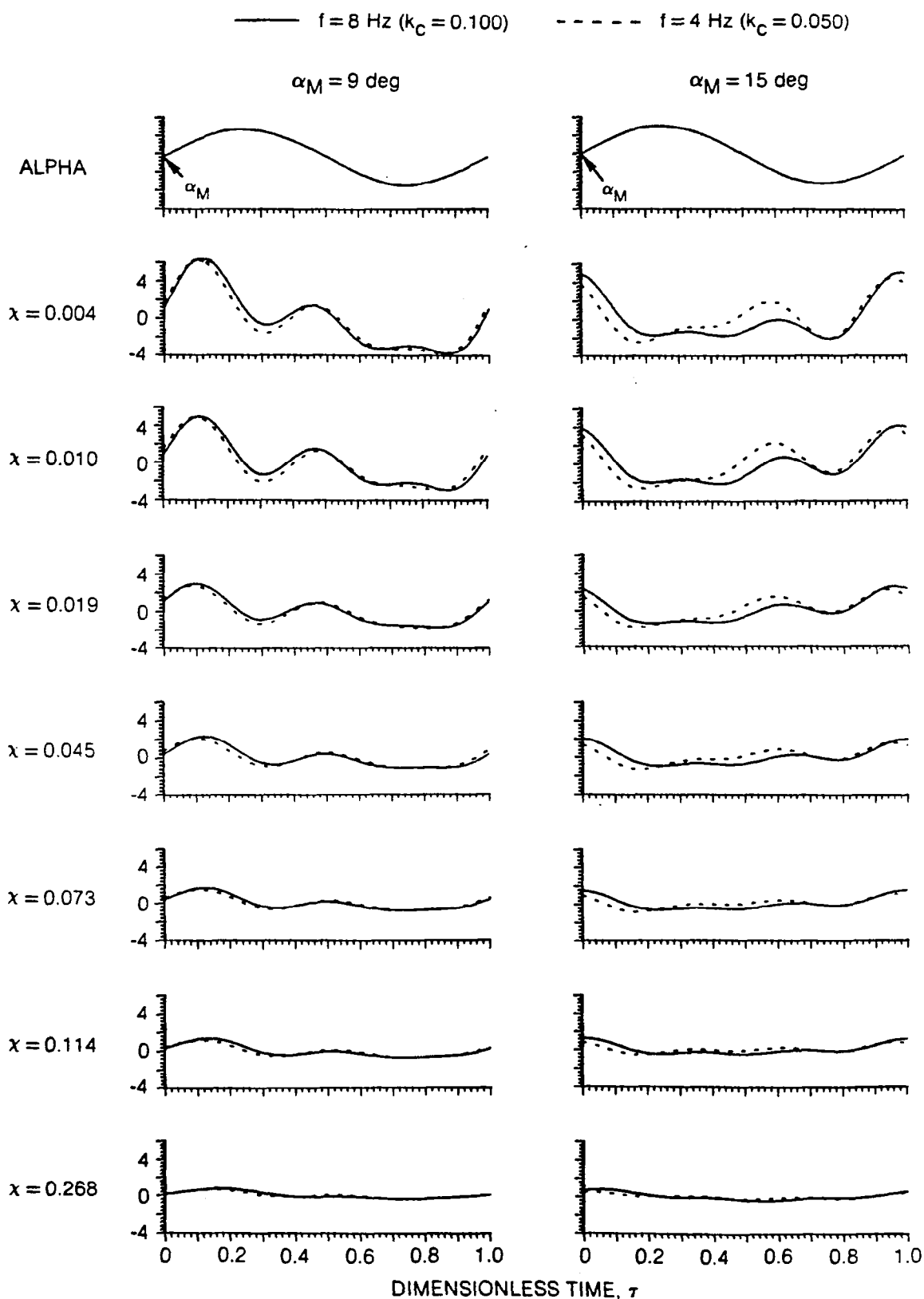


Fig. 44 Effect of Frequency on the Forwardmost Quarterchord Region Pressure Time Histories ($M_c = 0.30$, $\bar{\alpha} = 8 \text{ deg}$, $\Lambda = 0 \text{ deg}$)

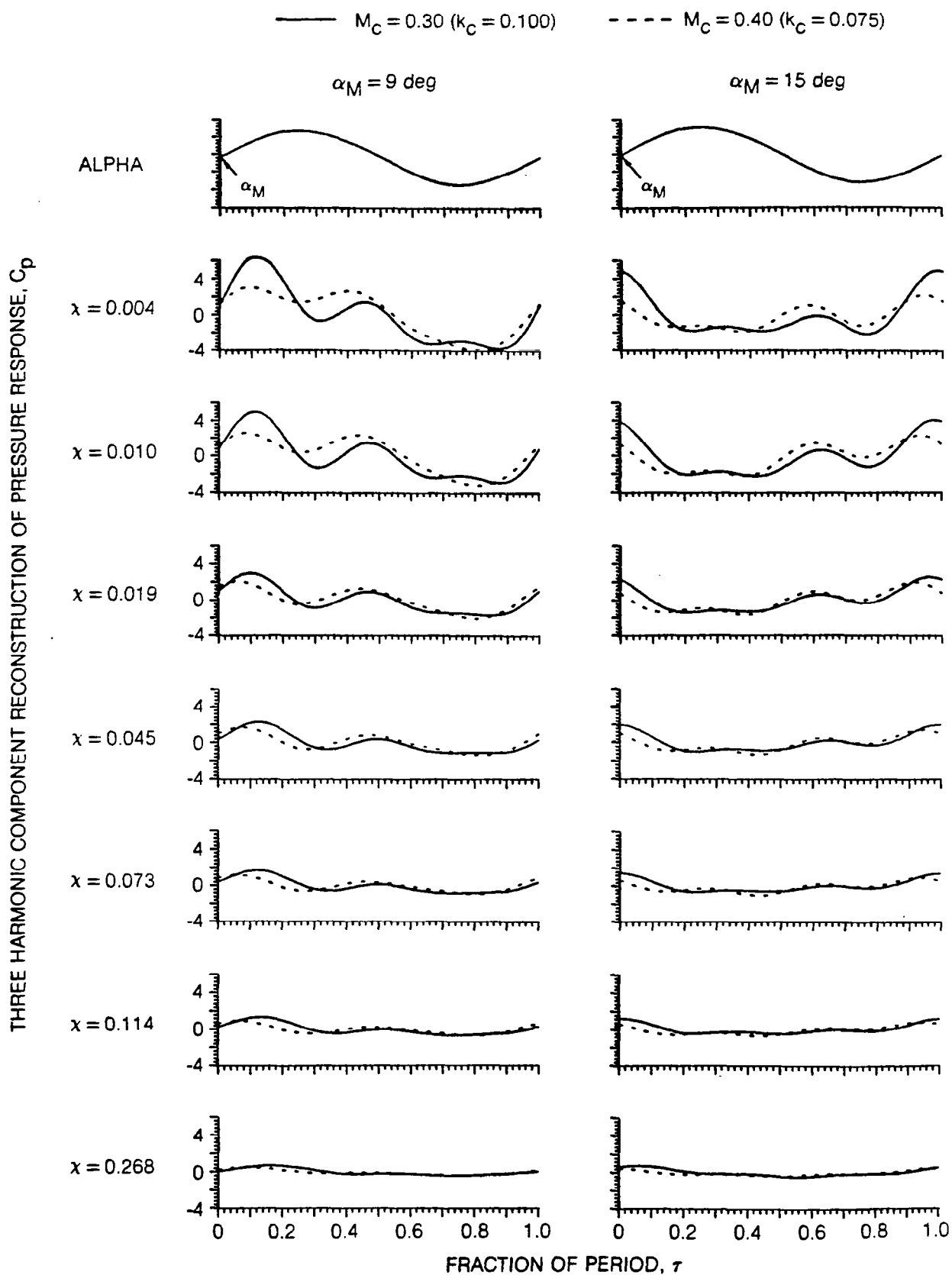


Fig. 45 Effect of Mach Number on the Forwardmost Quarterchord Region Pressure Time Histories ($f = 8 \text{ Hz}$, $\bar{\alpha} = 8 \text{ deg}$, $\Lambda = 0 \text{ deg}$)

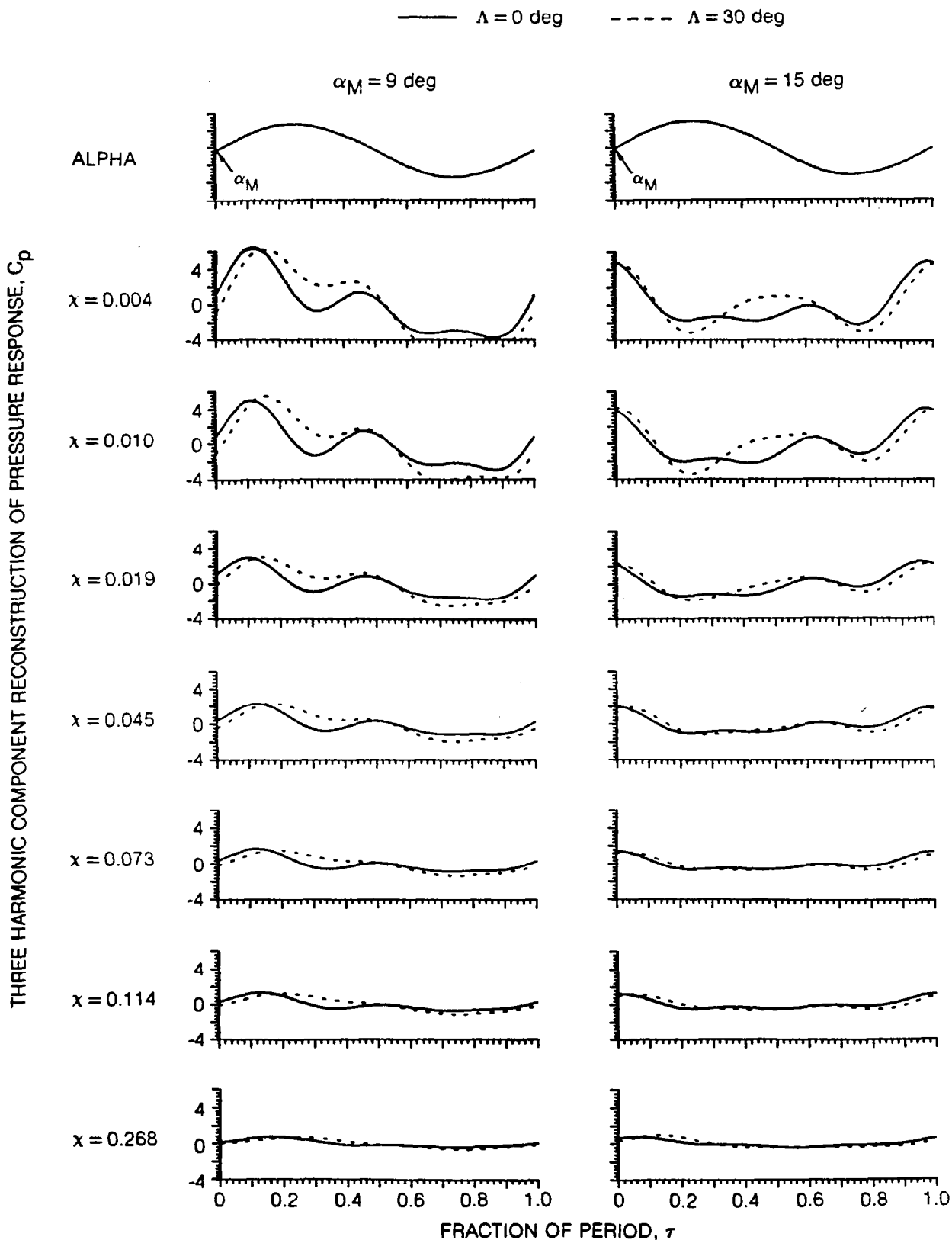


Fig. 46 Effect of Sweep on the Forwardmost Quarterchord Region Pressure Time Histories
 $k_c = 0.100$ ($f = 8$ Hz, $M_c = 0.30$) and $\bar{\alpha} = 8$ deg

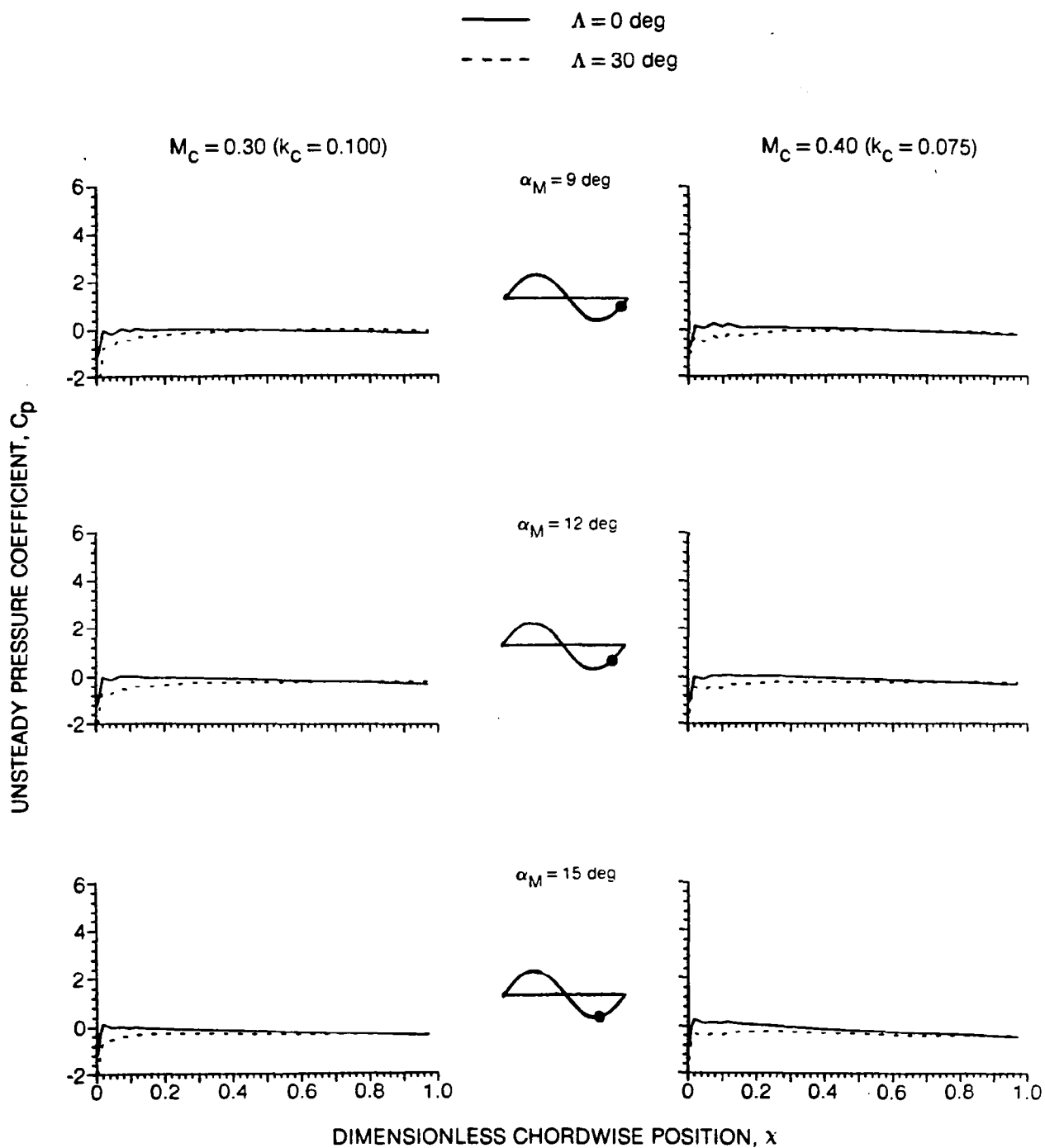


Fig. 47 Effect of α_M on Sweep Dependence of Upper Surface Response at $\alpha = 7.4 \text{ deg}$ Upstroke ($f = 8 \text{ Hz}$, $\bar{\alpha} = 8 \text{ deg}$)

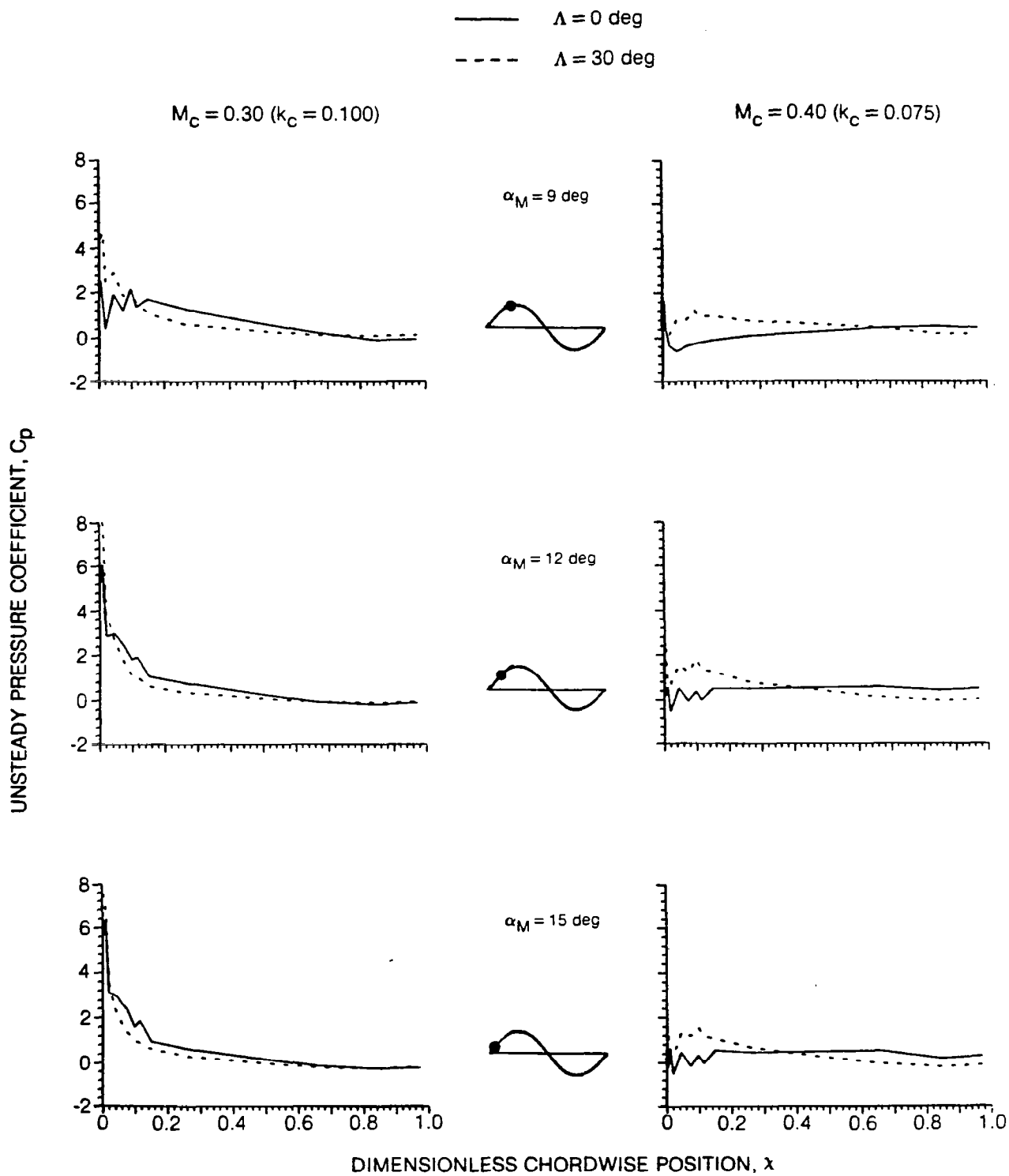


Fig. 48 Effect of α_M on Sweep of Dependence of Upper Surface Response at $\alpha = 16.6$ deg Upstroke ($f = 8$ Hz, $\bar{\alpha} = 8$ deg)

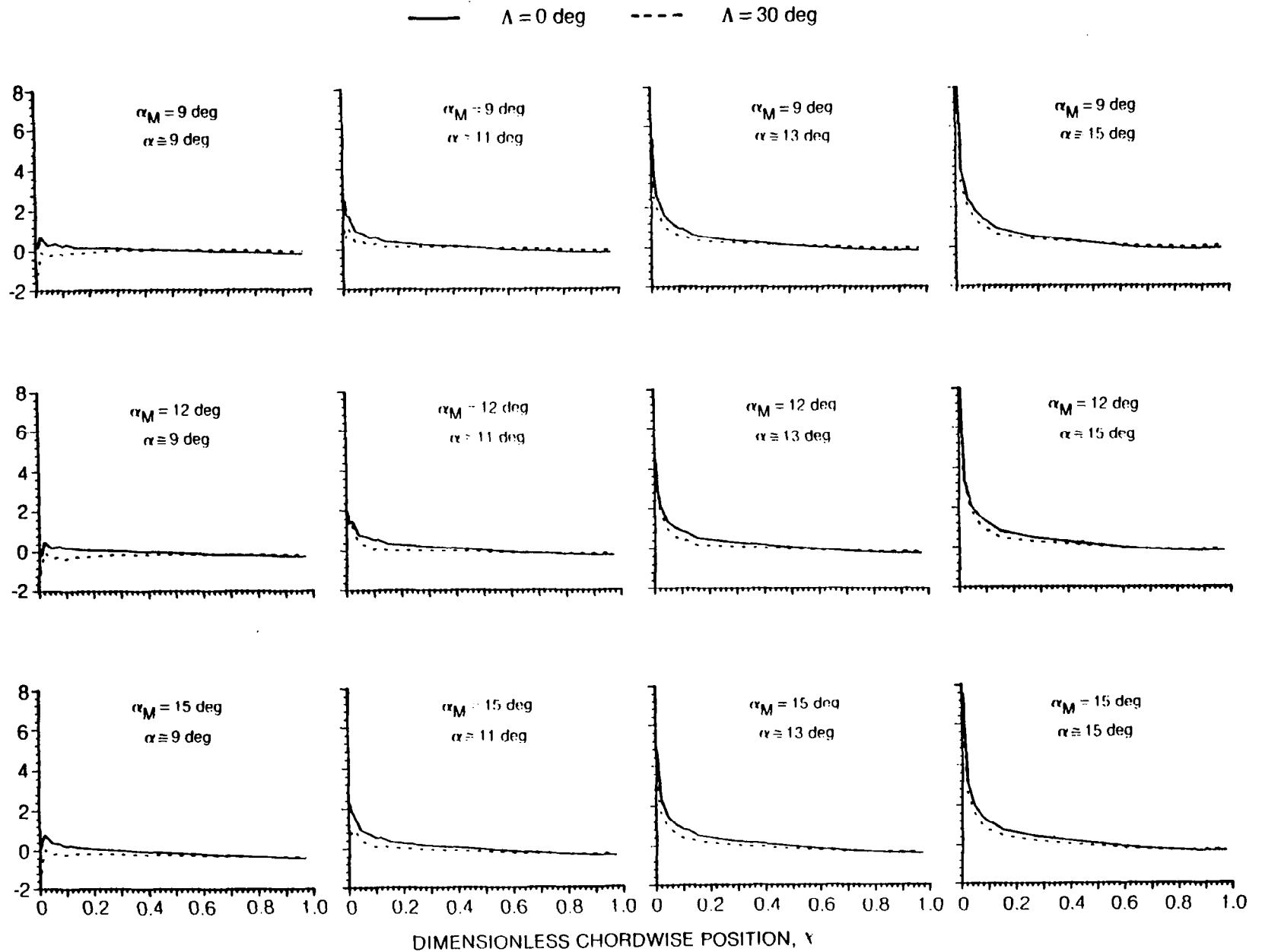
UNSTEADY PRESSURE COEFFICIENT, C_p 

Fig. 49 Effect of Sweep and Mean Incidence Angle on Upper Surface Response in Midrange Upstroke Portion of Motion cycle $k_c = 0.100$ ($f = 8$ Hz, $M_c = 0.30$) and $\bar{\alpha} = 8$ deg)

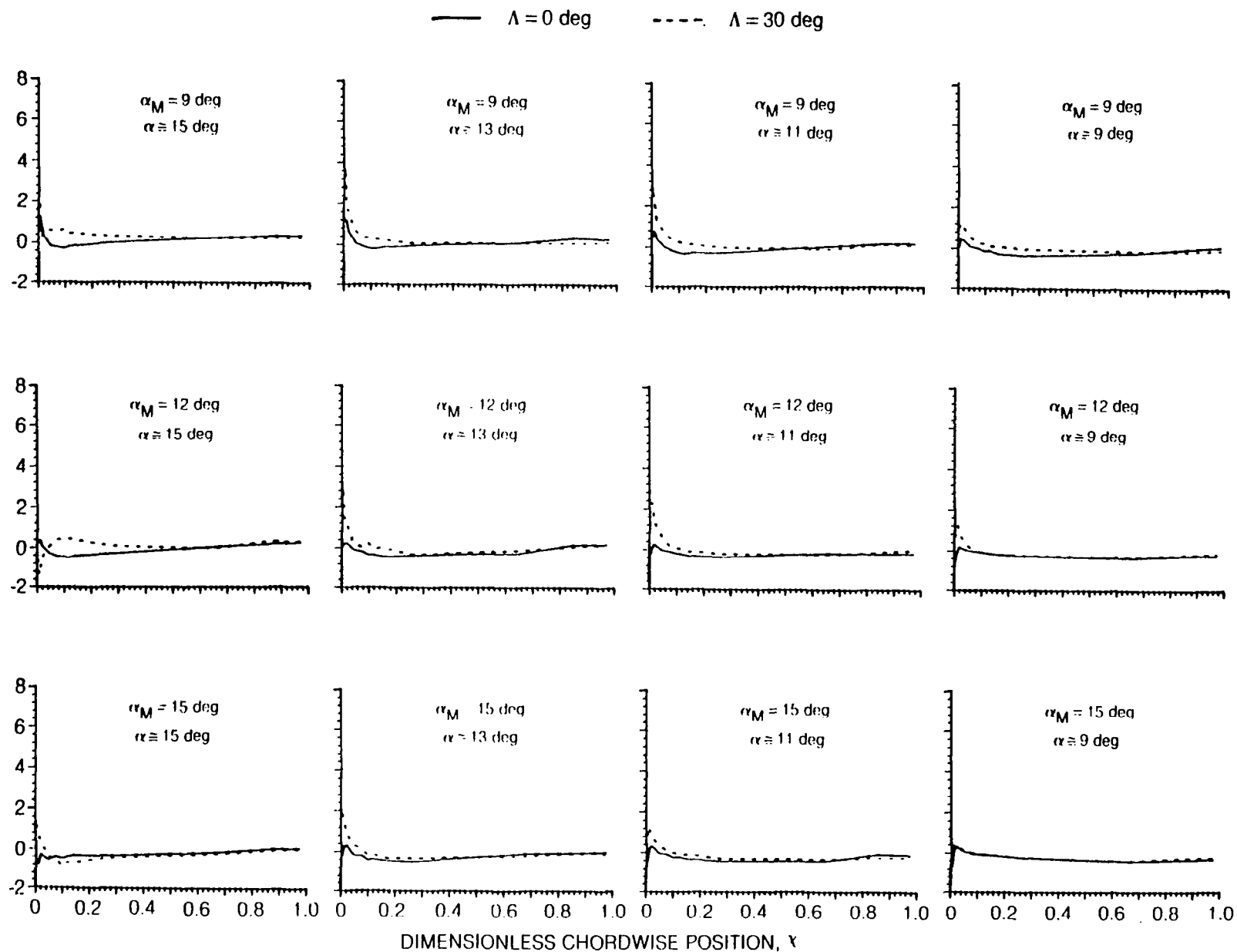


Fig. 50 Effect of Sweep and Mean Incidence Angle on Upper Surface Response in Midrange Downstroke Portion of Motion Cycle $k_c = 0.100$ ($f = 8$ Hz, $M_c = 0.30$) and $\bar{\alpha} = 8$ deg)

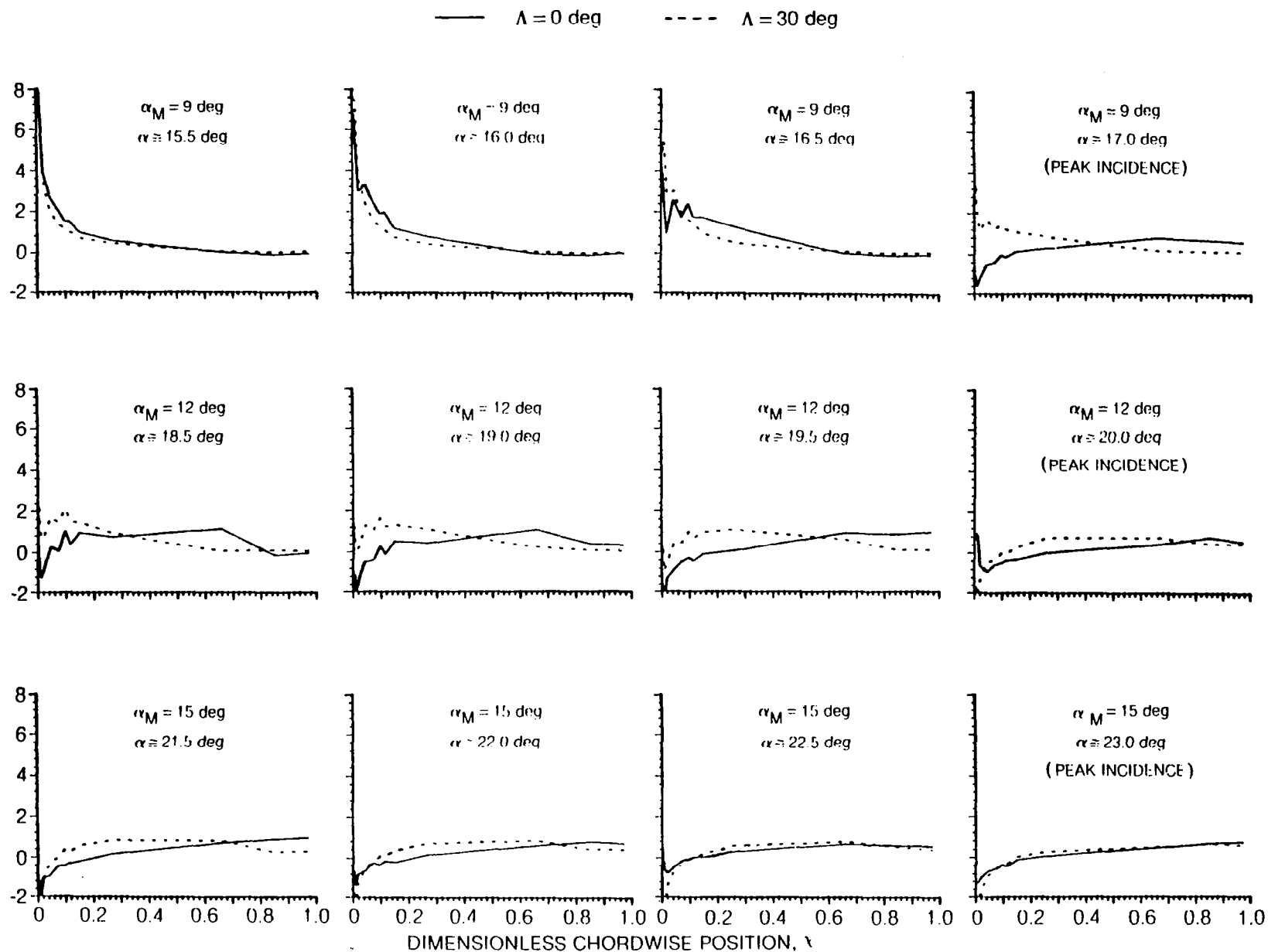


Fig. 51 Effect of Sweep on Upper Surface Response in High Incidence Upstroke Portion of Motion Cycle for Three Mean Incidence Angle Settings $k_c = 0.100$ ($f = 8$ Hz, $M_c = 0.30$) and $\bar{\alpha} = 8$ deg

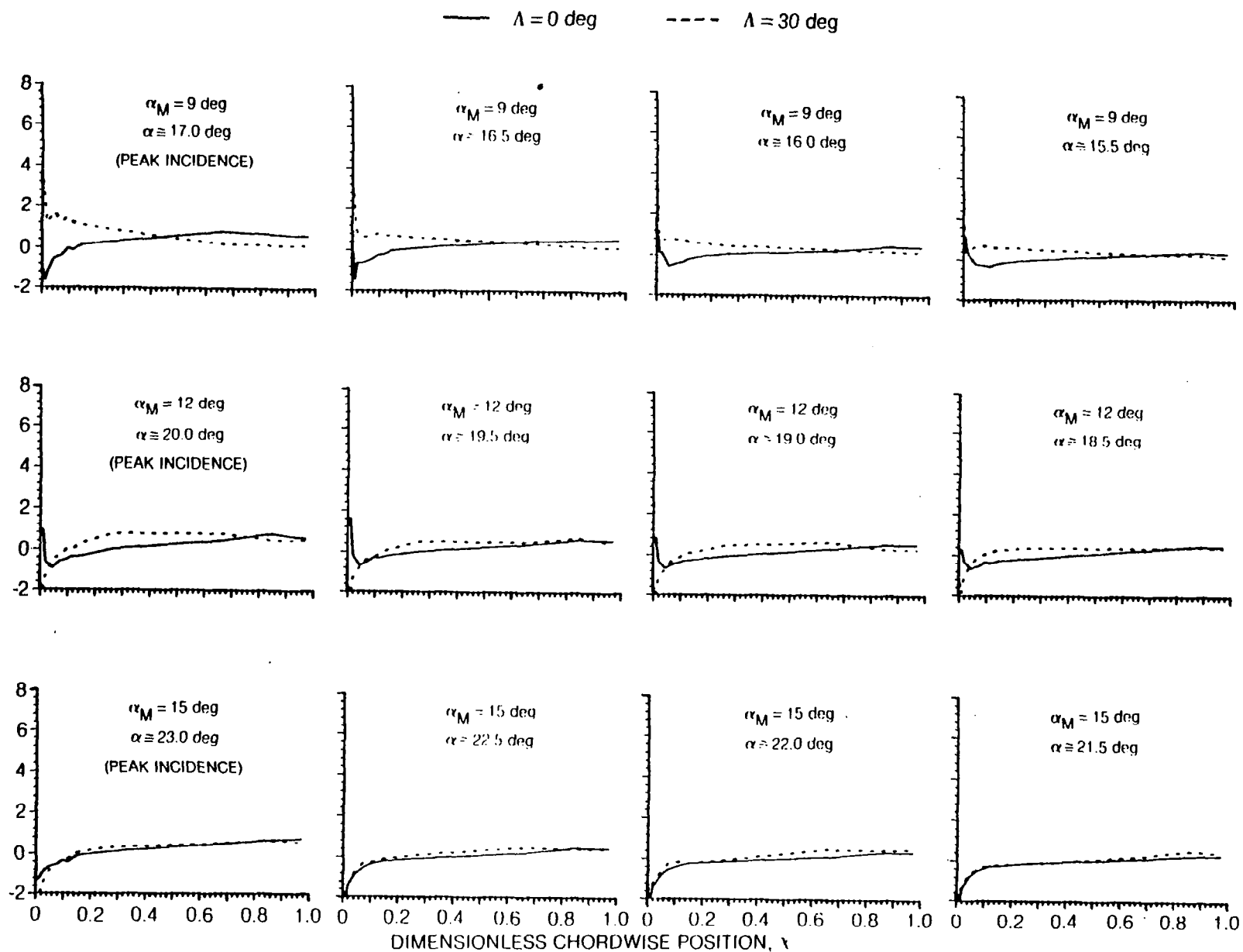
UNSTEADY PRESSURE COEFFICIENT, C_p 

Fig. 52 Effect of Sweep on Upper Surface Response in High Incidence Downstroke Portion of Motion Cycle for Three Mean Incidence Angle Settings $k_C = 0.100$ ($f = 8$ Hz, $M_C = 0.30$) and $\bar{\alpha} = 8$ deg

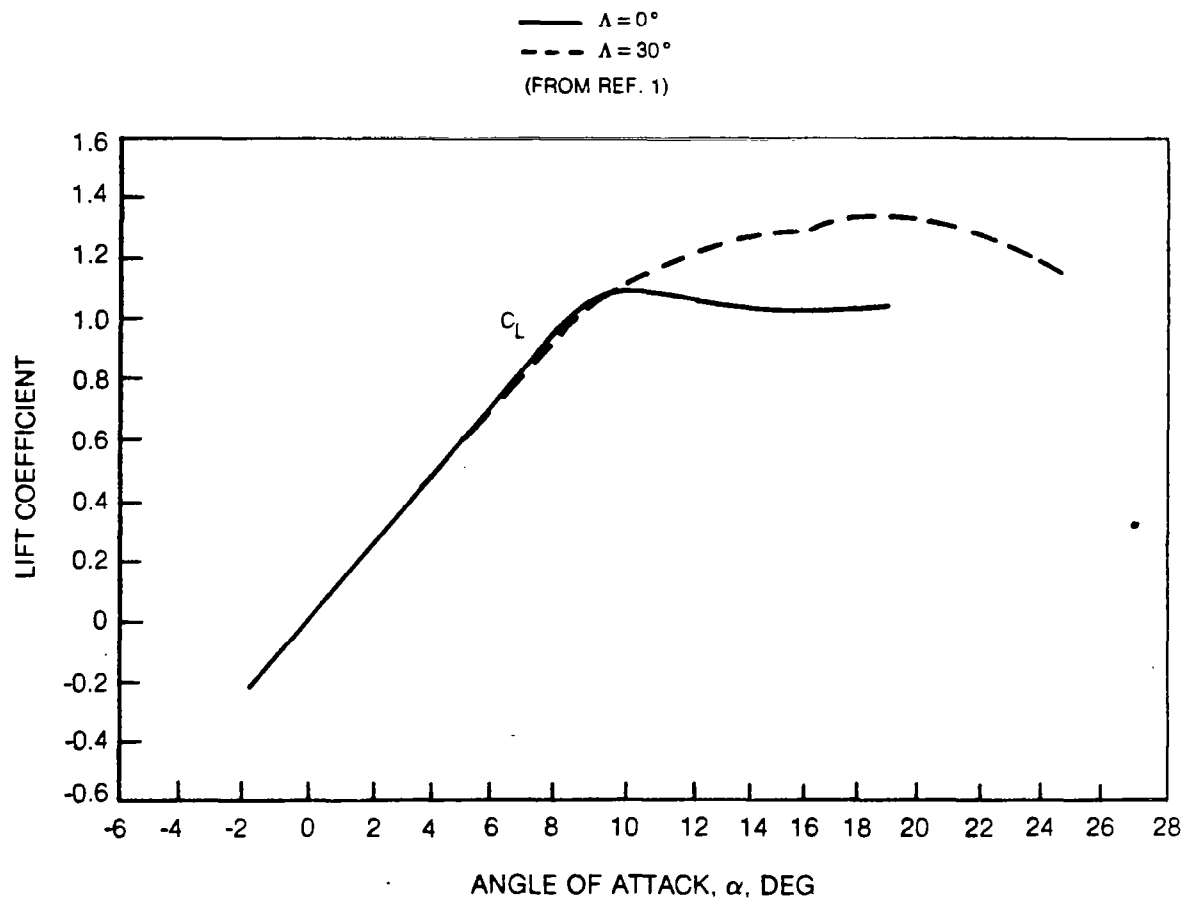


Fig. 53 Steady-State Lift Coefficient for NACA 0012 Airfoil at $M_c = 0.40$

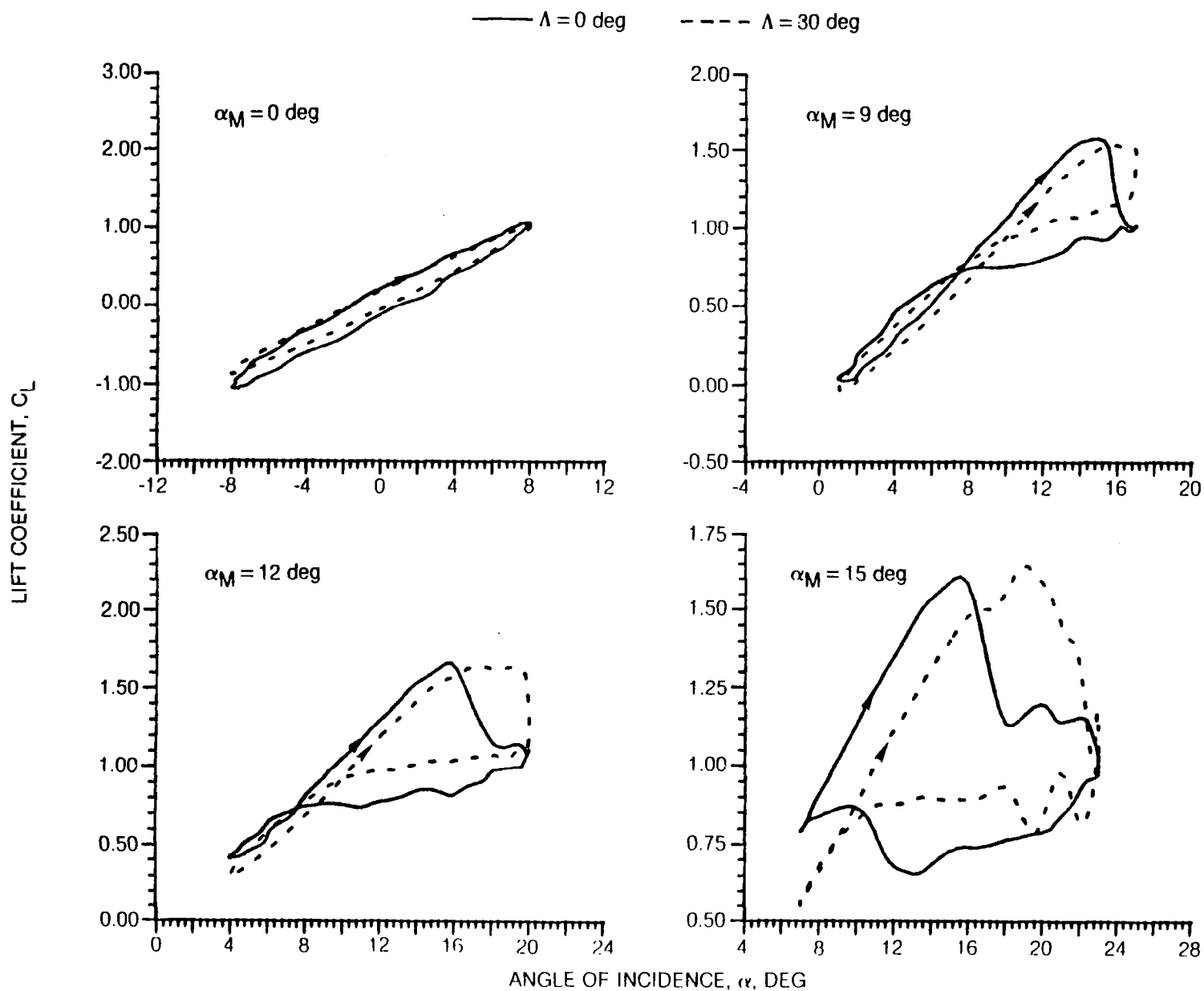


Fig. 54 Effect of Mean Incidence Angle and Sweep on the Lift Response at $k_c = 0.075$ ($f = 8$ Hz, $M_c = 0.40$), and $\bar{\alpha} = 8$ deg

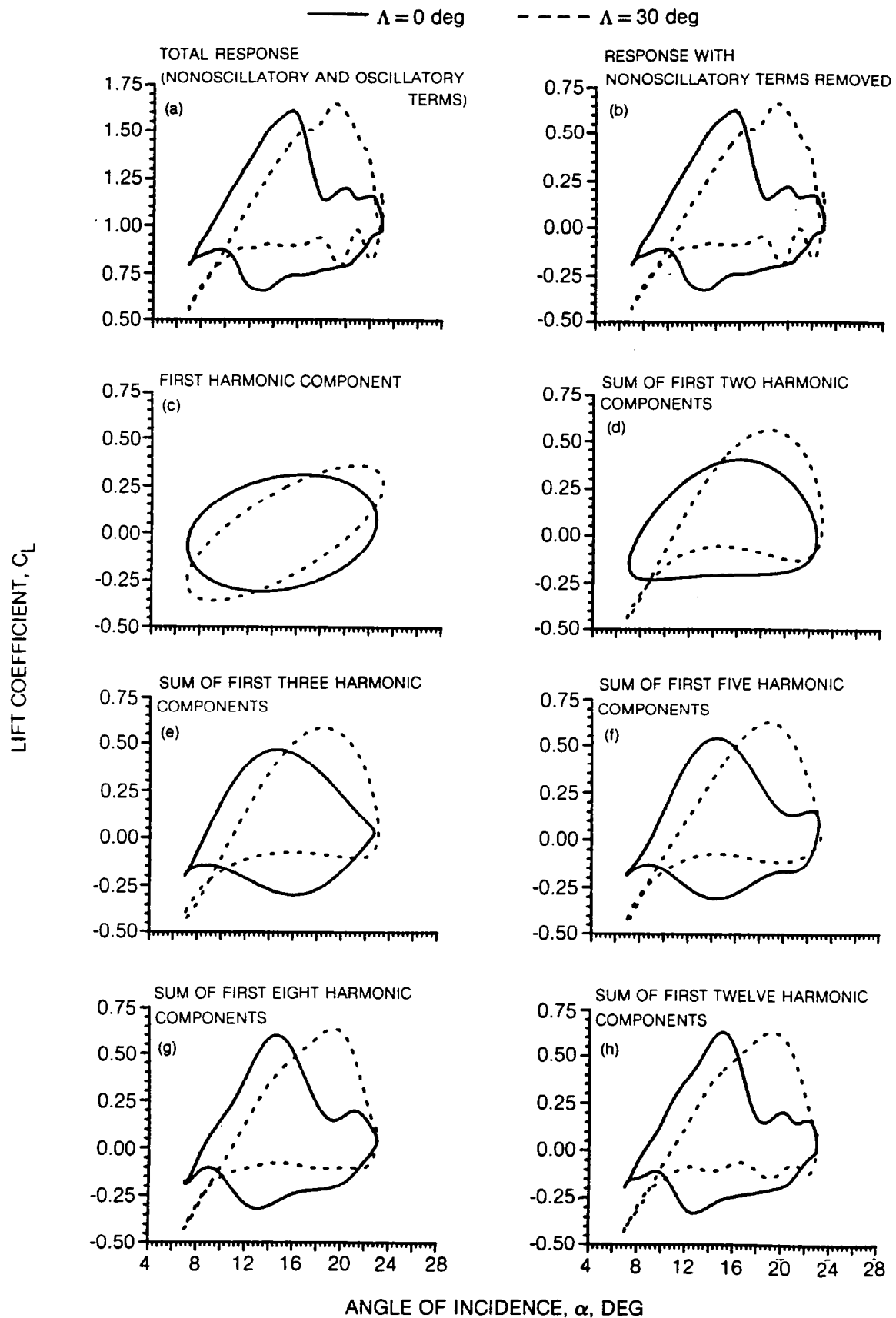


Fig. 55 Harmonic Analysis of the Sweep Effect on the Lift Response at $\alpha_M = 15$ deg, $k_c = 0.075$ ($f = 8$ Hz, $M_c = 0.40$), and $\bar{\alpha} = 8$ deg

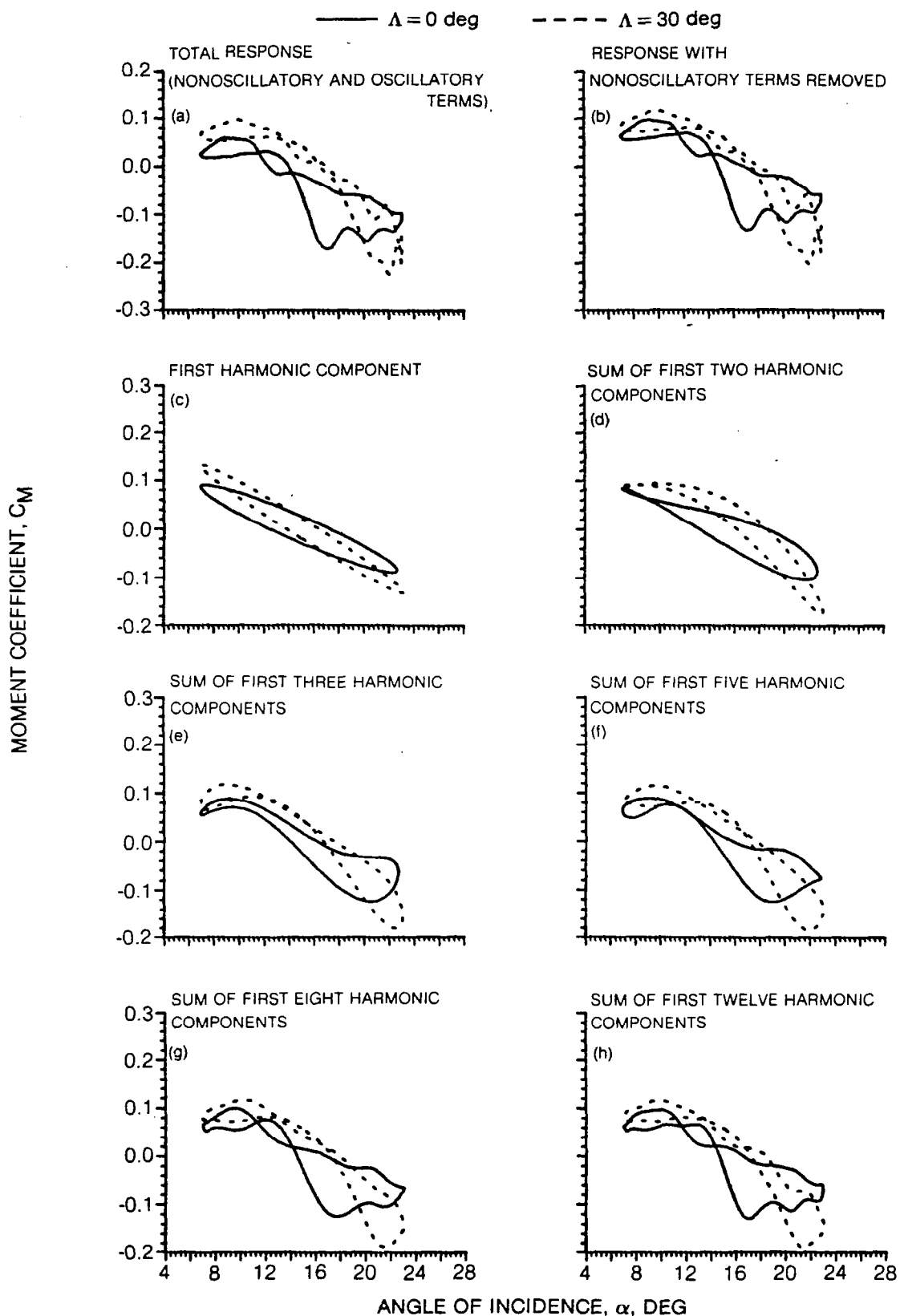


Fig. 56 Harmonic Analysis of the Sweep Effect on the Moment Response at $\alpha_M = 15$ deg, $k_C = 0.075$ ($f = 8$ Hz, $M_C = 0.40$), and $\bar{\alpha} = 8$ deg

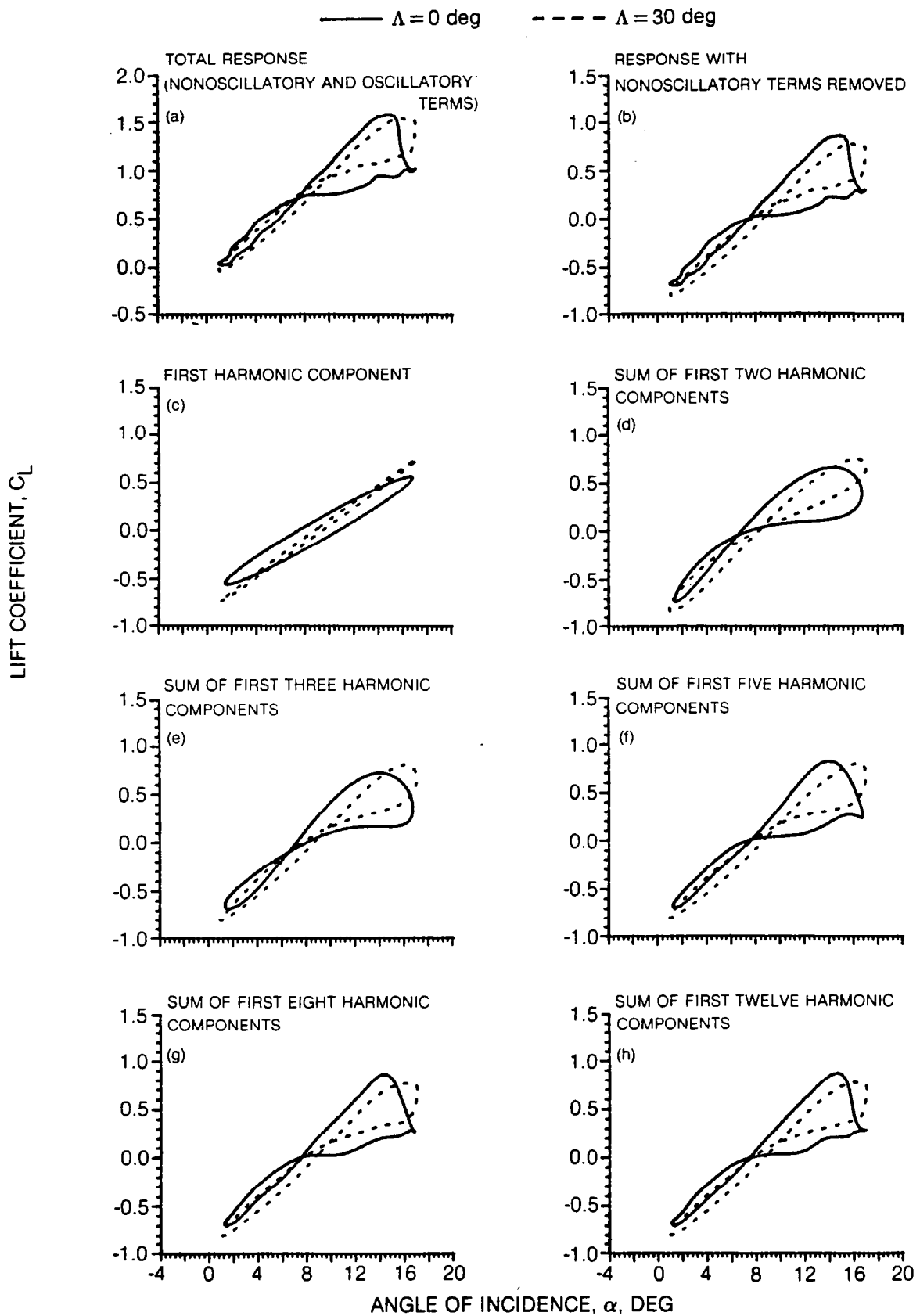


Fig. 57 Harmonic Analysis of the Sweep Effect on the Lift Response at $\alpha_M = 9$ deg, $k_c = 0.075$ ($f = 8$ Hz, $M_c = 0.40$), and $\bar{\alpha} = 8$ deg

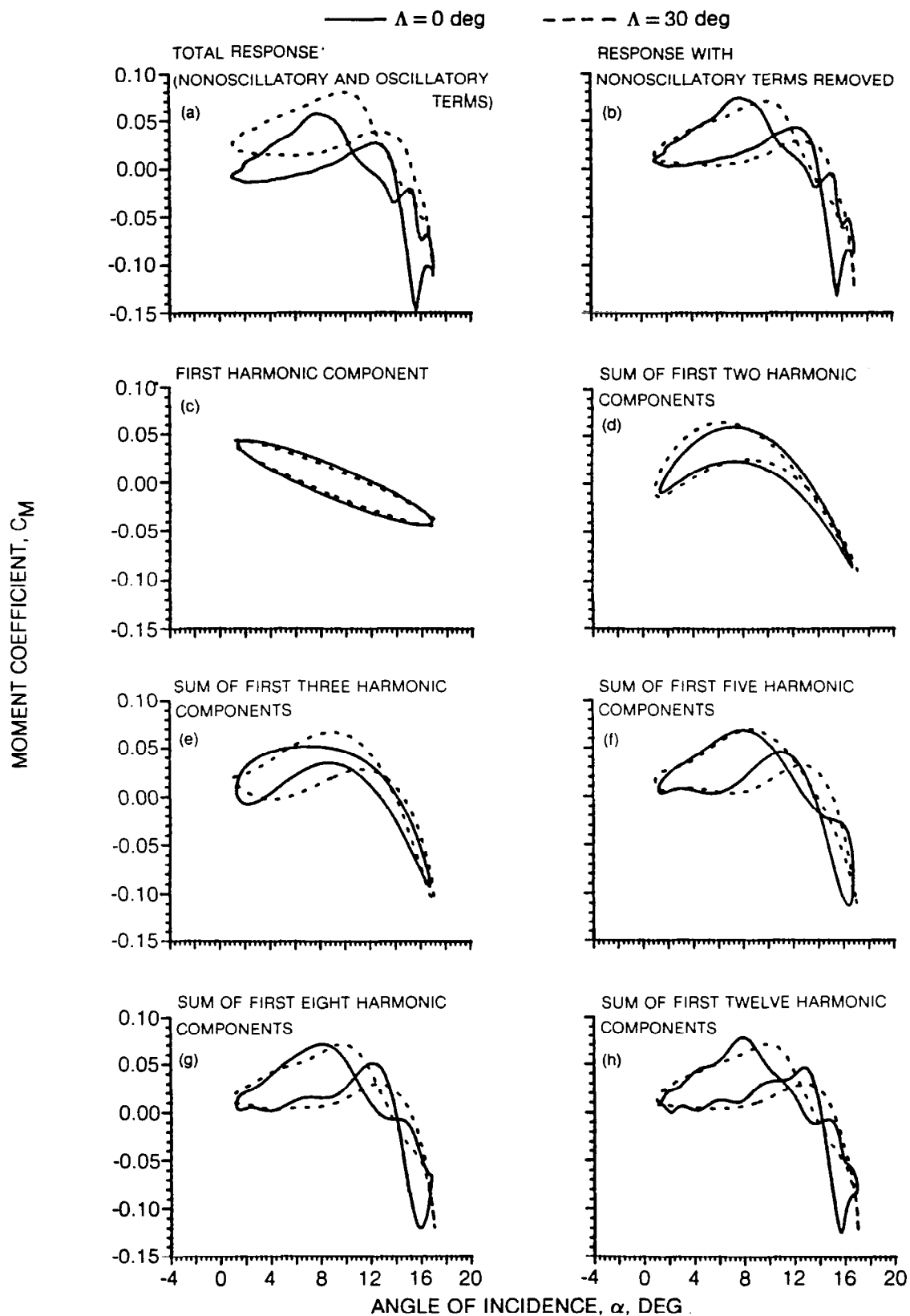


Fig. 58 Harmonic Analysis of the Sweep Effect on the Moment Response at $\alpha_M = 9$ deg, $k_C = 0.075$ ($f = 8$ Hz, $M_C = 0.40$), and $\bar{\alpha} = 8$ deg